Experimental Study of the Decay $K^+ \to \pi^+\gamma\gamma$

Tamaki Yoshioka[1]

Department of Physics, Graduate School of Science
The University of Tokyo
and
High Energy Accelerator Research Organization (KEK)

[1]electric address: tyosioka@post.kek.jp

Abstract

An experimental search[1] for the rare decay $K^+ \to \pi^+\gamma\gamma$ in the π^+ momentum region $P_{\pi^+} > 213$ MeV/c was performed using the E949 detector at the Brookhaven National Laboratory (BNL). During the E949-2002 run, data equivalent to 1.2×10^{12} kaon decays were collected while the $K^+ \to \pi^+\gamma\gamma$ trigger was active. No candidate event was observed in the search region, where the total background level was (0.197 ± 0.070) events. By assuming the π^+ spectrum predicted by the Chiral Perturbation Theory with higher order corrections, the upper limit for the branching ratio was set to be

$$Br(K^+ \to \pi^+\gamma\gamma, P_{\pi^+} > 213\mathrm{MeV/c}) < 9.08 \times 10^{-9}$$

at the 90% Confidence Level.

This report is based on a dissertation that was submitted to the graduate school of the University of Tokyo.

[1] This research was supported by the Japan-U.S. Cooperative Research Program in High Energy Physics and the Grant-in-Aid for Scientific Research on Priority Areas "Origin of Mass".

Contents

Chapter 1

Introduction

1.1 Overview

This thesis describes an experimental search for the rare decay $K^+ \to \pi^+\gamma\gamma$ in the π^+ momentum region $P_{\pi^+} > 213\text{MeV/c}$ using a data set that was collected in the year of 2002 by the E949 detector at the Brookhaven National Laboratory (BNL).

The $K^+ \to \pi^+\gamma\gamma$ decay is a process of Flavor-Changing Neutral Current, but is considered to be due to hadronic interactions of the kaon and the pion. The motivation to study this decay mode is a stringent test of the Chiral Perturbation Theory (ChPT) [1,2,3], which is an effective field theory of Quantum Chromodynamics (QCD) in the low-energy region. The Lagrangian is constructed with the fields of the kaon and the pion, which are regarded as Nambu-Goldstone bosons [4,5] due to spontaneous breaking of the chiral symmetry in the original QCD Lagrangian. An observation of this decay mode in the π^+ momentum region $P_{\pi^+} < 180$ MeV/c was reported in 1997 with the branching ratio $Br(K^+ \to \pi^+\gamma\gamma, 100\text{MeV/c} < P_{\pi^+} < 180\text{MeV/c}) = (6.0 \pm 1.5(stat.) \pm 0.7(syst.)) \times 10^{-7}$ [6]. As described in this chapter, higher order corrections to the ChPT are sensitive to the π^+ momentum spectrum in the region $P_{\pi^+} > 213\text{MeV/c}$, while there has not been yet any observation in this region. In order to prove the existence of higher order corrections, the new search described in this thesis was performed in the region $P_{\pi^+} > 213\text{MeV/c}$.

The outline of this thesis is as follows: the remaining part of this chapter is devoted to theoretical considerations and the experimental status of $K^+ \to \pi^+\gamma\gamma$. In Chapter 2, the E949 experiment and the detector used in this study are described. In Chapter 3, details of the offline analysis, including background categorization, are explained. In Chapter 4, the background level is estimated for each background source. In Chapter 5, the results of this analysis, including the acceptance calculations, are described. In Chapter 6, the conclusion of this analysis is given.

1.2 Theoretical Consideration

1.2.1 Chiral Perturbation Theory

The general form of the $K \to \pi\gamma\gamma$ amplitude is given by

$$\mathcal{M}(K(p) \to \pi(p')\gamma(q_1, \epsilon_1)\gamma(q_2, \epsilon_2)) = \epsilon_\mu(q_1)\epsilon_\nu(q_2)M^{\mu\nu}(p, q_1, q_2), \tag{1.1}$$

where ϵ_1 and ϵ_2 are the polarization vectors of the photons (γ_1 and γ_2). The decay amplitude ($M^{\mu\nu}$) consists of four invariant amplitudes (A, B, C and D) as

$$\begin{aligned}
M^{\mu\nu}(p, q_1, q_2) &= \frac{A(y,z)}{M_K^2}(q_2^\mu q_1^\nu - q_1 \cdot q_2 g^{\mu\nu}) \\
&+ \frac{B(y,z)}{M_K^4}(p \cdot q_1 q_2^\mu p^\nu + p \cdot q_2 p^\mu q_1^\nu - p \cdot q_1 p \cdot q_2 g^{\mu\nu} - q_1 \cdot q_2 p^\mu p^\nu) \\
&+ \frac{C(y,z)}{M_K^2}(\epsilon^{\mu\nu\rho\sigma} q_{1\rho} q_{2\sigma}) \\
&+ \frac{D(y,z)}{M_K^4}\{\epsilon^{\mu\nu\rho\sigma}(p \cdot q_2 q_{1\rho} + p \cdot q_1 q_{2\rho})p_\sigma + (p^\mu \epsilon^{\nu\alpha\beta\gamma} + p^\nu \epsilon^{\mu\alpha\beta\gamma})p_\alpha q_{1\beta} q_{2\gamma}\},
\end{aligned} \tag{1.2}$$

where

$$y \equiv \frac{p \cdot (q_1 - q_2)}{M_K^2}, \quad z \equiv \frac{(q_1 + q_2)^2}{M_K^2}. \tag{1.3}$$

Variables y and z are dimensionless, and their allowed regions are

$$0 \le |y| \le \frac{1}{2}\lambda^{1/2}(1, r_\pi^2, z), \quad 0 \le z \le (1 - r_\pi)^2, \tag{1.4}$$

with

$$\lambda(a, b, c) \equiv a^2 + b^2 + c^2 - 2(ab + bc + ca), \quad r_\pi \equiv \frac{M_\pi}{M_K}. \tag{1.5}$$

The invariant amplitudes (A, B, C and D) are calculated in the framework of Chiral Perturbation Theory (ChPT) [7]. ChPT is an effective field theory of Quantum Chromodynamics (QCD) in the low-energy region, where QCD can not be treated perturbatively, and gives a systematic way to describe hadronic interactions in this region. It assumes only chiral symmetry, which is a global symmetry of the QCD Lagrangian in the limit where the quark masses are set to be zero, and spontaneously breaking of the symmetry generates 8 pseudoscalar mesons (π, K, $\bar{K}$ and η), which are regarded as Nambu-Goldstone bosons. The effective Lagrangian ($\mathcal{L}_{\text{eff}}$) is expanded in powers of the momentum (p) of pseudoscalar mesons, such that $\mathcal{L}_{\text{eff}} = \sum_n \mathcal{L}_{2n}$, where $2n$ represents the order of the momentum ($O(p^{2n})$). Radiative processes, such as $K^+ \to \pi^+\gamma\gamma$, can also be treated in ChPT by replacing the derivative (∂_μ) in the Lagrangian by the covariant derivative ($\partial_\mu - ieA_\mu$) in the well-known manner in Quantum Electrodynamics (QED) so that the effective Lagrangian remains gauge-invariant. From Eqn. 1.2, the differential decay rate is expressed as

$$\frac{\partial\Gamma}{\partial y \partial z} = \frac{M_K}{2^9\pi^3}\left[z^2\left(|A + B|^2 + |C|^2\right) + \left(y^2 - \frac{1}{4}\lambda\left(1, r_\pi^2, z\right)\right)^2\left(|B|^2 + |D|^2\right)\right]. \tag{1.6}$$

1.2.2 $O(p^4)$ Contributions

There is no tree-level contribution at $O(p^2)$ for the decay $K^+ \to \pi^+\gamma\gamma$; the leading order starts at $O(p^4)$. Amplitudes B and D do not contribute at $O(p^4)$, and the remaining amplitudes (A and C) only depend on z, and not on y. The differential decay rate can therefore be obtained by integrating Eqn. 1.6 over y as

$$\frac{d\Gamma}{dz}(K^+ \to \pi^+\gamma\gamma) = \frac{M_{K^+}}{2^{10}\pi^3} z^2 \sqrt{\lambda(1, z, r_\pi^2)}(|A(z)|^2 + |C(z)|^2). \tag{1.7}$$

The amplitude A is calculated from the loop diagrams in ChPT shown in Fig. 1.1; the amplitude C can be calculated from the diagram with anomaly in ChPT ($\pi^0, \eta \to \gamma\gamma$) shown in Fig. 1.2. The results are expressed as follows:

$$A(z) = \frac{G_8 M_{K^+}^2 \alpha_{em}}{2\pi z}\left[(r_\pi^2 - 1 - z)F\left(\frac{z}{r_\pi^2}\right) + (1 - r_\pi^2 - z)F(z) + \hat{c}z\right], \tag{1.8}$$

$$C(z) = \frac{G_8 M_{K^+}^2 \alpha_{em}}{z}\left[\frac{z - r_\pi^2}{z - r_\pi^2 + ir_\pi \frac{\Gamma_{\pi^0}}{M_{K^+}}} - \frac{z - \frac{2+r_\pi^2}{3}}{z - r_\eta^2}\right], \tag{1.9}$$

where

$$F(x) \equiv \begin{cases} 1 - \dfrac{4}{x}\arcsin^2\left(\dfrac{\sqrt{x}}{2}\right), & x \leq 4, \\ 1 + \dfrac{1}{x}\left(\ln\left(\dfrac{1-\beta(x)}{1+\beta(x)}\right) + i\pi\right)^2, & x > 4, \end{cases} \tag{1.10}$$

$$\beta(x) \equiv \sqrt{1 - \frac{4}{x}}. \tag{1.11}$$

G_8 is the effective weak-coupling constant determined from $K \to \pi\pi$ decays at $O(p^2)$, and is

$$|G_8| \simeq 9.2 \times 10^{-6}\text{GeV}^{-2} \quad . \tag{1.12}$$

Γ_{π^0} is the decay rate for $\pi^0 \to \gamma\gamma$. Note that the amplitude A contains one undetermined parameter ($\hat{c}$), defined as

$$\hat{c} \equiv \frac{128\pi^2}{3}[3(L_9 + L_{10}) + N_{14} - N_{15} - 2N_{18}]. \tag{1.13}$$

L_9 and L_{10} are the local $O(p^4)$ strong couplings, and L_{14}, L_{15} and L_{18} are $O(p^4)$ weak couplings that can not be experimentally determined. $\hat{c}$ can therefore be computed only in a model-dependent way, and various models have predicted that $\hat{c} \sim O(1)$ [8, 9, 10, 11]. From the viewpoint of experimentalists, it can be said that the $K^+ \to \pi^+\gamma\gamma$ amplitude is governed and described by a single phenomenological parameter, $\hat{c}$.

The ChPT predicts a peculiar π^+ momentum spectra, as shown in the Fig. 1.3.[1] The spectra is very sensitive to $\hat{c}$. By integrating the differential decay rate (Eqn. 1.7) over z,

[1] In theoretical papers on $K^+ \to \pi^+\gamma\gamma$, the spectra of invariant mass of two photons ($M_{\gamma\gamma}$) are used to discuss the spectrum shape. $M_{\gamma\gamma}$ is expressed as $M_{\gamma\gamma}^2 = M_{K^+}^2 + M_{\pi^+}^2 - 2M_{K^+}\sqrt{(P_{\pi^+}^2 + M_{\pi^+}^2)}$. The π^+ momentum spectra are used throughout this thesis, because the accuracy of the π^+ momentum measurement is better than that of the photon energy in the E949 detector.

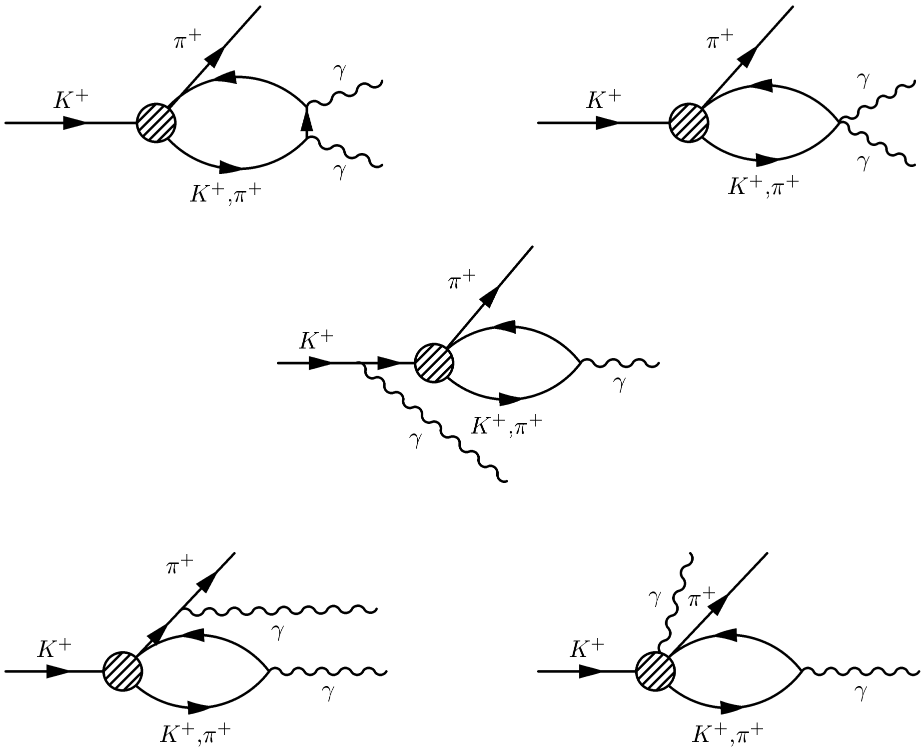

Figure 1.1: Loop diagrams contributing to the amplitude A at $O(p^4)$.

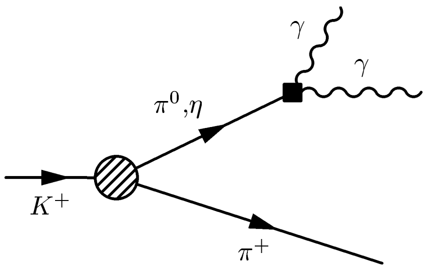

Figure 1.2: Diagram with anomaly in ChPT contributing to the amplitude C at $O(p^4)$.

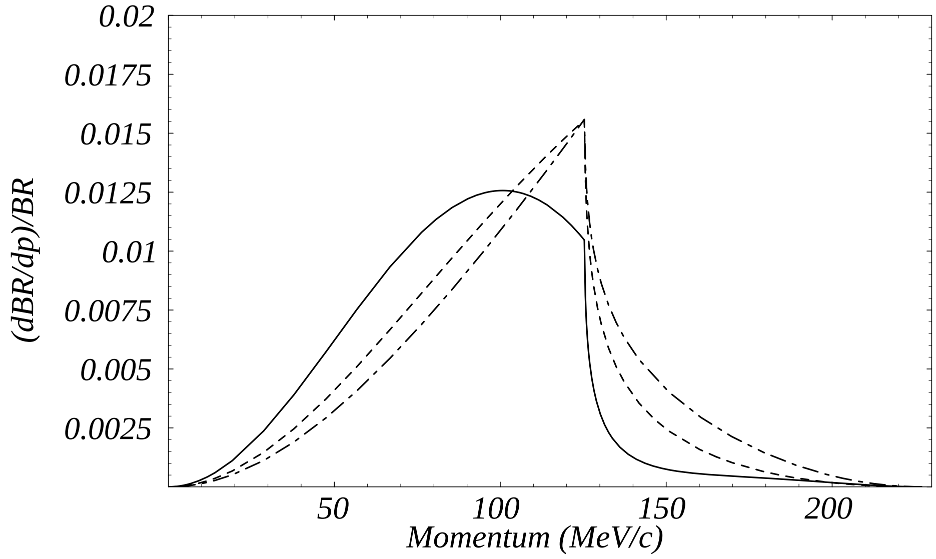

Figure 1.3: Differential branching ratio, predicted by the ChPT with $O(p^4)$, as a function of the π^+ momentum for $\hat{c} = -2$ (solid), $\hat{c} = 0$ (dashed) and $\hat{c} = 2$ (dot-dashed).

the total decay rate is obtained as follows:

$$\Gamma_A(K^+ \to \pi^+\gamma\gamma) = (2.80 + 0.87\hat{c} + 0.17\hat{c}^2) \times 10^{-20}\text{MeV}, \tag{1.14}$$

$$\Gamma_C(K^+ \to \pi^+\gamma\gamma) = 0.26 \times 10^{-20}\text{MeV}. \tag{1.15}$$

1.2.3 $O(p^6)$ Contributions

The branching ratio for the neutral mode, $K_L \to \pi^0\gamma\gamma$, measured in the early '90 [12, 13], was a factor of two higher than that predicted by ChPT, which was confirmed by new measurements by the KTeV and NA48 experiments [14, 15]. This indicated a necessity for next-to-leading order [$O(p^6)$] contributions and vector meson exchange contributions; the former (called "unitarity corrections") was obtained by an empirical fit to the decay amplitude of $K_L \to \pi^+\pi^-\pi^0$ [16, 17]. In the case of $K^+ \to \pi^+\gamma\gamma$, similar corrections are obtained from $K^+ \to \pi^+\pi^+\pi^-$ and the vector meson contributions are thought to be negligible compared to the unitarity corrections [18]. An invariant amplitude of the decay $K^+(p) \to \pi^+(p_1)\pi^+(p_2)\pi^-(p_3)$ is expressed in terms of the following kinematic variables:

$$X \equiv \frac{s_2 - s_1}{M^2_{\pi^+}}, \quad Y \equiv \frac{s_3 - s_0}{M^2_{\pi^+}}, \tag{1.16}$$

where $s_i \equiv (p - p_i)^2$ for $i = 1, 2, 3$ and $s_0 \equiv (s_1 + s_2 + s_3)/3$. The leading amplitude $O(p^2)$ is given as follows in ChPT:

$$A^{(2)} = G_8 M^2_{K^+} \left(\frac{2}{3} - r^2_\pi Y\right). \tag{1.17}$$

The amplitude $A^{(2)}$ with the value G_8 in Eqn. 1.12 underestimates the experimental result by 20-30%. Introducing $O(p^4)$ higher-order corrections to $K^+ \to \pi^+\pi^+\pi^-$ give good agreement with the experiment, and

$$
\begin{aligned}
A^{(4)} = \quad & 2\alpha_1 - \alpha_3 + (\beta_1 - \frac{1}{2}\beta_3 + \sqrt{3}\gamma_3)Y \\
& -2(\zeta_1 + \zeta_3)(Y^2 + \frac{X^2}{3}) - (\xi_1 + \xi_3 - \xi_3')(Y^2 - \frac{X^2}{3}). \qquad (1.18)
\end{aligned}
$$

The $O(p^6)$ contributions to $K^+ \to \pi^+\gamma\gamma$, induced by the $O(p^4)$ contributions to $K^+ \to \pi^+\pi^+\pi^-$, can be obtained by replacing the kinematic variables with appropriate covariant derivatives. The $O(p^6)$ contributions re-introduce the amplitudes A and B, but the amplitude C still remains unchanged. The corrected amplitudes are given as follows:

$$
\begin{aligned}
A(z,y) \quad = \quad & \frac{\alpha_{em}}{2\pi} \cdot \\
& \Bigg\{ \left[2(2\alpha_1 - \alpha_3) + \left(1 + \frac{1}{3r_\pi^2} - \frac{z}{r_\pi^2}\right) \left(\beta_1 - \frac{1}{2}\beta_3 + \sqrt{3}\gamma_3\right) \right] \frac{1}{z} F\left(\frac{z}{r_\pi^2}\right) \\
& - \frac{8}{3r_\pi^4}(2\zeta_1 - \xi_1) \left[r_\pi^2 \left(\ln\left(\frac{m_\pi^2}{\mu^2}\right) - 1 \right) \right. \\
& \qquad \left. + \frac{1}{18}(1 + 6(r_\pi^2 - z) + 9(r_\pi^2 - z)^2) \frac{1}{z} F\left(\frac{z}{r_\pi^2}\right) \right] \\
& - \frac{8}{3r_\pi^4}(4\zeta_1 + \xi_1) \left[-\frac{1}{12}(1 + 6r_\pi^2) \ln\left(\frac{m_\pi^2}{\mu^2}\right) + \frac{r_\pi^2}{2} \right. \\
& \qquad - \frac{1}{36}\left(9r_\pi^2 - 5 - 3(1 + 3r_\pi^2)(r_\pi^2 - z)\right) \frac{1}{z} F\left(\frac{z}{r_\pi^2}\right) \\
& \qquad + \frac{y^2}{z}\left(\frac{1}{12} + 3R\left(\frac{z}{r_\pi^2}\right) + \frac{1}{2}\left(1 + \frac{2r_\pi^2}{z}\right) F\left(\frac{z}{r_\pi^2}\right)\right) \\
& \qquad - \frac{(1 - r_\pi^2 + z)^2}{4z}\left(\frac{1}{12} + R\left(\frac{z}{r_\pi^2}\right) + \frac{1}{2}\left(1 + \frac{2r_\pi^2}{z}\right) F\left(\frac{z}{r_\pi^2}\right)\right) \\
& \qquad + (1 - r_\pi^2 + z)\left(\frac{1}{24} + \frac{z}{72r_\pi^2}\right. \\
& \qquad\qquad \left. + \frac{1}{12}\left(1 + \frac{2r_\pi^2}{z}\right)\left(\frac{z}{r_\pi^2} R\left(\frac{z}{r_\pi^2}\right) + 3F\left(\frac{z}{r_\pi^2}\right)\right)\right) \\
& \qquad - z\left(\frac{1}{36} - \frac{r_\pi^2}{24z} + \frac{z}{72r_\pi^2} + \frac{1}{12}\left(\frac{z}{r_\pi^2} + 1 - \frac{2r_\pi^2}{z}\right) R\left(\frac{z}{r_\pi^2}\right)\right. \\
& \qquad - z\left(\frac{1}{36} - \frac{r_\pi^2}{24z} + \frac{z}{72r_\pi^2} + \frac{1}{12}\left(\frac{z}{r_\pi^2} + 1 - \frac{2r_\pi^2}{z}\right) R\left(\frac{z}{r_\pi^2}\right)\right. \\
& \qquad\quad \left.\left. + \frac{r_\pi^2}{2z}\left(1 - \frac{r_\pi^2}{z}\right) F\left(\frac{z}{r_\pi^2}\right)\right)\right] \\
& + G_8 M_{K^+}^2 \left[(z + r_\pi^2 - 1)\frac{1}{z}F(z) - \hat{c} + 2r_\pi^2\eta_1 + 2\eta_2 \right] \Bigg\}, \qquad (1.19)
\end{aligned}
$$

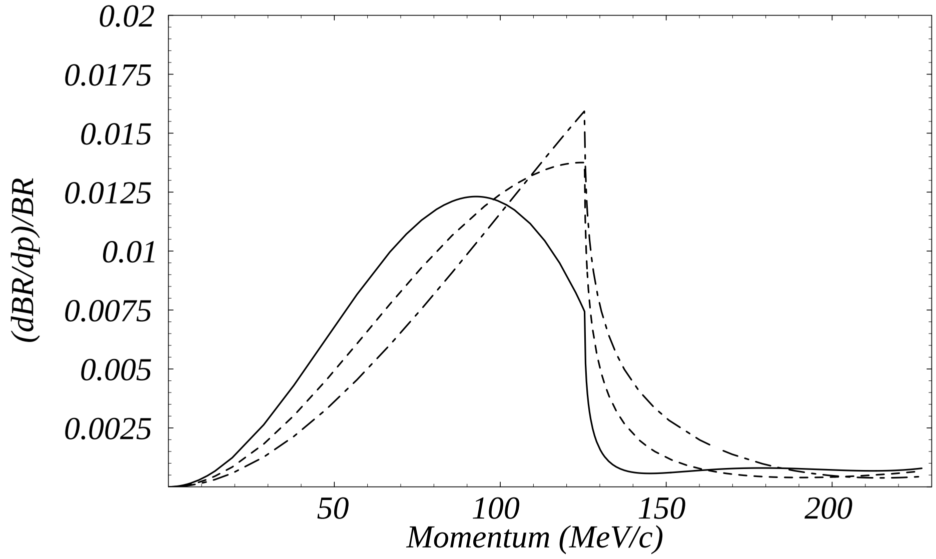

Figure 1.4: Differential branching ratio, predicted by the ChPT with $O(p^6)$ corrections, as a function of the π^+ momentum for $\hat{c} = -2$ (solid), $\hat{c} = 0$ (dashed) and $\hat{c} = 2$ (dot-dashed).

$$\begin{aligned} B(z,y) &= \frac{\alpha_{em}}{\pi}\left\{\frac{1}{3r_\pi^4}(4\zeta_1+\xi_1)\left[-\frac{1}{6}\left(1+2\ln\left(\frac{M_{\pi^+}^2}{\mu^2}\right)\right)+\frac{z}{18r_\pi^2}-\frac{2r_\pi^2}{z}F\left(\frac{z}{r_\pi^2}\right)\right.\right. \\ &\left.\left.+\frac{1}{3}\left(\frac{z}{r_\pi^2}-10\right)R\left(\frac{z}{r_\pi^2}\right)\right]+G_8M_{K^+}^2\eta_3\right\}, \end{aligned} \tag{1.20}$$

where the function $F(x)$ has been defined in Eqn. 1.11 and

$$R(x) \equiv \begin{cases} -\frac{1}{6}+\frac{2}{x}-\frac{2}{x}\sqrt{\frac{4}{x}-1}\arcsin(\frac{\sqrt{x}}{2}), & x \le 4 \\ -\frac{1}{6}+\frac{2}{x}-\frac{\beta(x)}{x}\left(\ln\left(\frac{1-\beta(x)}{1+\beta(x)}\right)+i\pi\right), & x > 4. \end{cases} \tag{1.21}$$

Note that the amplitude A still contains the undetermined parameter, $\hat{c}$. The π^+ momentum spectra with the $O(p^6)$ corrections for various $\hat{c}$'s are shown in Fig. 1.4. The $O(p^6)$ corrections change both the π^+ momentum spectra and the total branching ratio; a comparison of the π^+ momentum spectrum with $O(p^4)$ and the spectrum including $O(p^6)$ for the same value of $\hat{c}$ is shown Fig. 1.5 for the case of $\hat{c} = 0$. In Fig. 1.6, the momentum region $P_{\pi^+} > 180$MeV/c in Fig. 1.5 is enlarged. Note that the $O(p^6)$ corrections predict a nonzero amplitude at the kinematic end point $P_{\pi^+} = 227$MeV/c. The $O(p^6)$ corrections increase the branching ratio by 30-40% compared to the $O(p^4)$ at a given $\hat{c}$. The total branching ratio as a function of $\hat{c}$ is shown in Fig. 1.7, and the partial branching ratio in the momentum region $P_{\pi^+} > 213$MeV/c as a function of $\hat{c}$ is shown in Fig. 1.8. $O(p^6)$ corrections, if they exist, make the $K^+ \to \pi^+\gamma\gamma$ decay at the kinematic end point to be finite, which is a motivation of this experimental search.

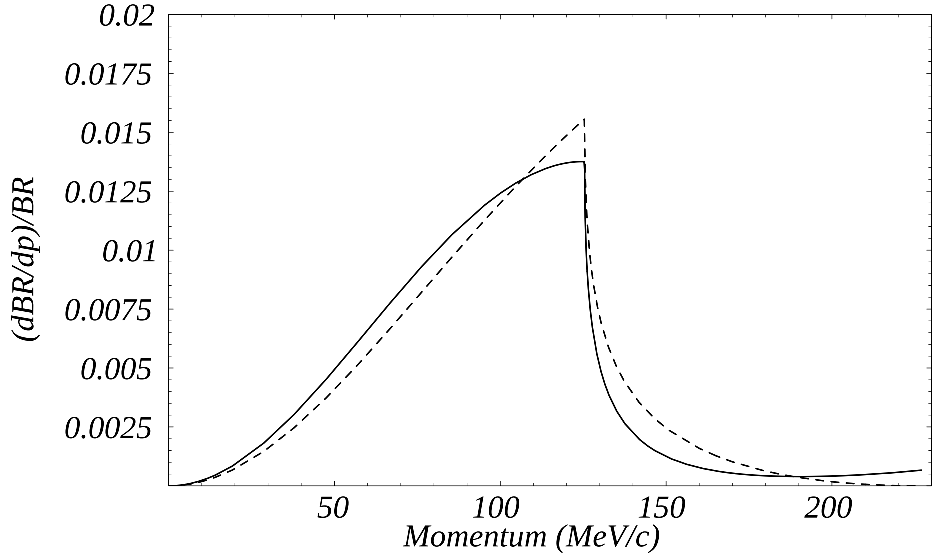

Figure 1.5: Comparison of the π^+ momentum spectrum with $O(p^4)$ (dashed) and the spectrum including $O(p^6)$ (solid) for $\hat{c} = 0$.

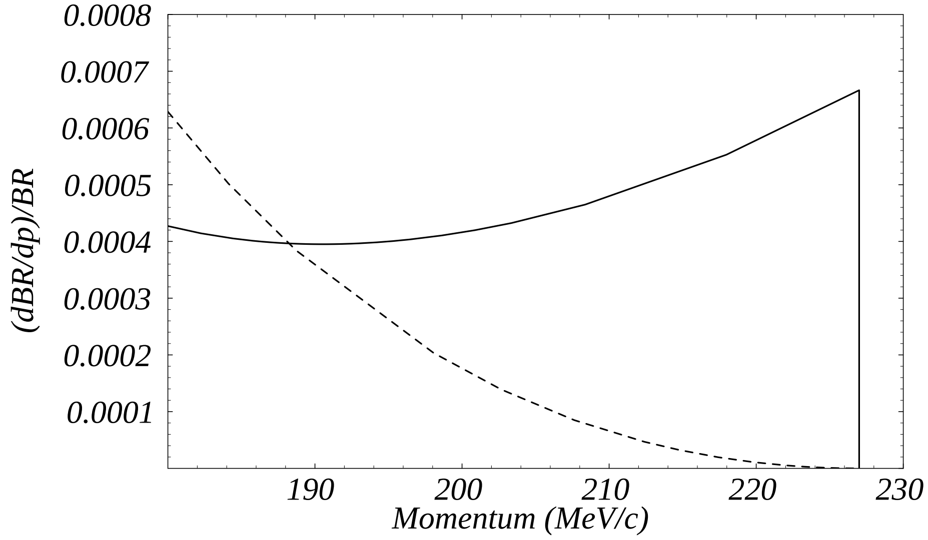

Figure 1.6: Comparison of the π^+ momentum spectrum with $O(p^4)$ (dashed) and the spectrum including $O(p^6)$ (solid) for $\hat{c} = 0$ in the momentum region $P_{\pi^+} > 180\mathrm{MeV/c}$.

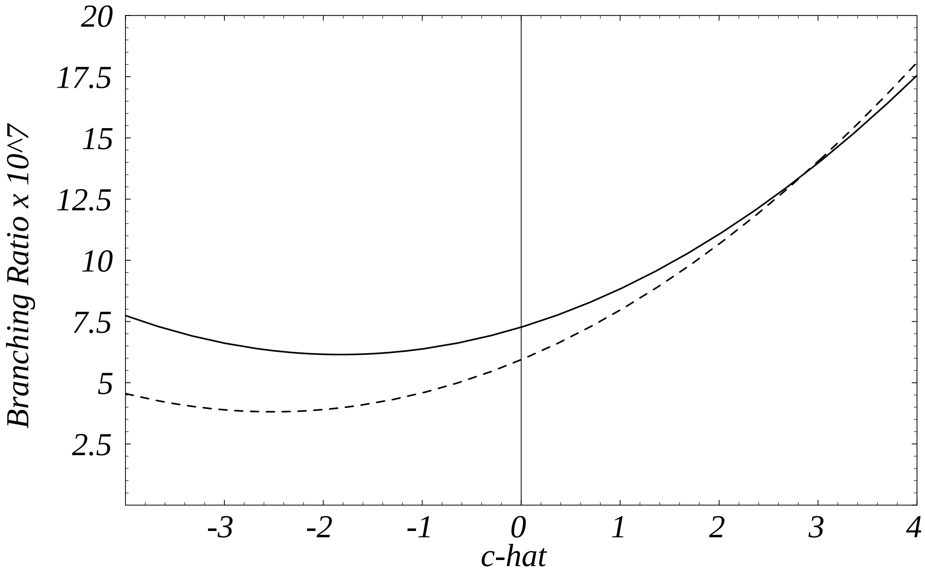

Figure 1.7: Total branching ratio as a function of $\hat{c}$ for the case of $O(p^4)$ (dashed) and the case including $O(p^6)$ corrections (solid).

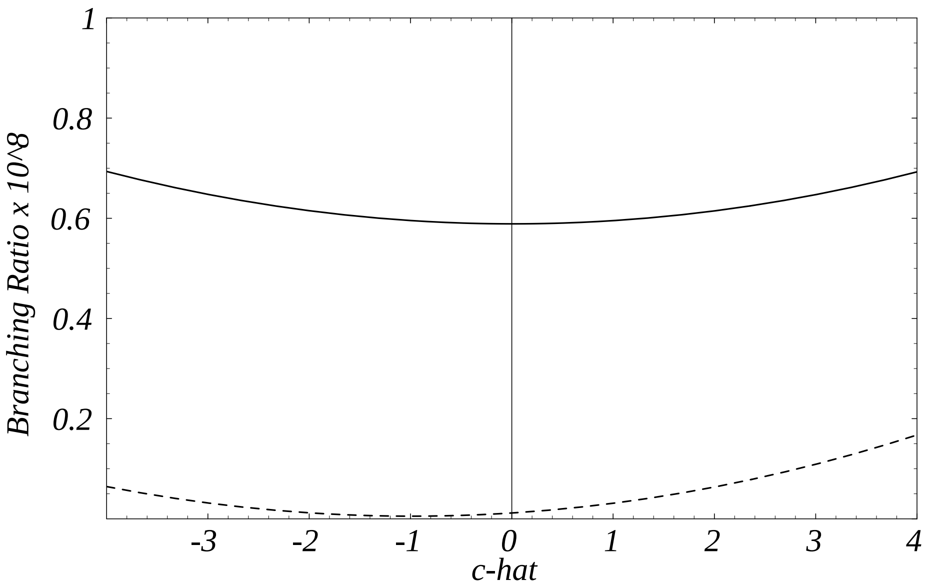

Figure 1.8: Partial branching ratio in the momentum region $P_{\pi^+} > 213\text{MeV/c}$ as a function of $\hat{c}$ for the case of $O(p^4)$ (dashed) and the case including $O(p^6)$ corrections (solid).

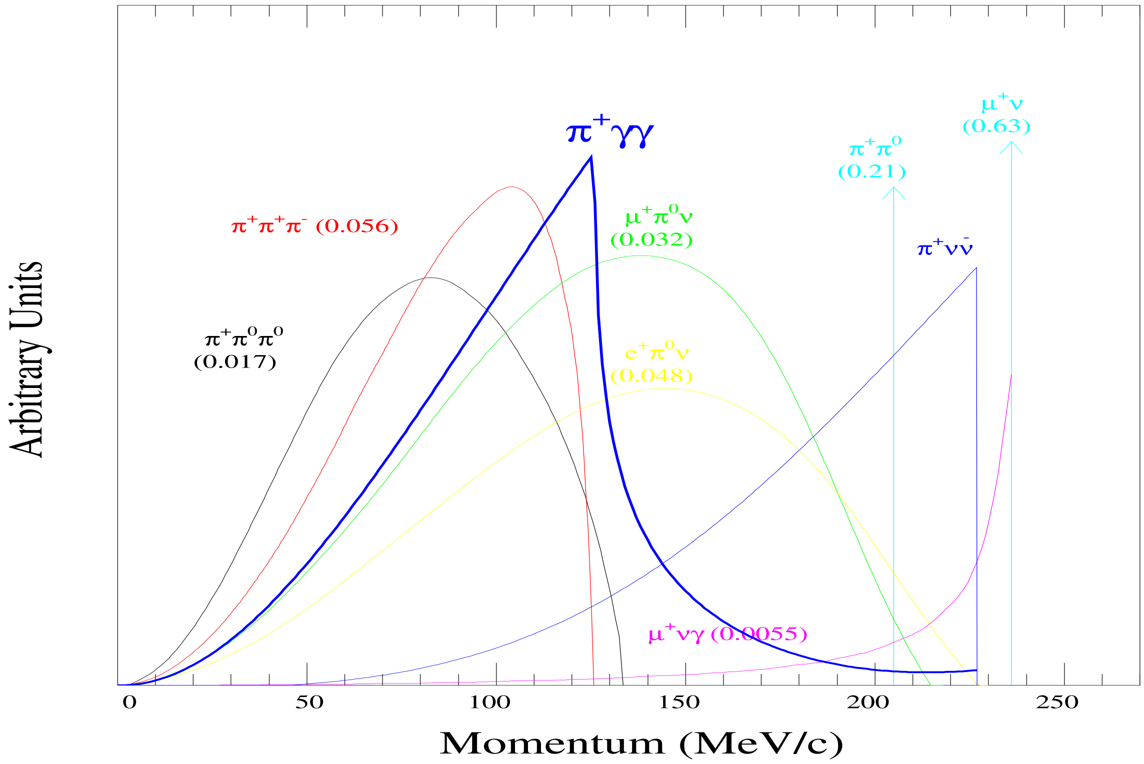

Figure 1.9: Momentum distributions of charged decay products from K^+ decay at rest. The numbers in parenthesis are the branching ratio for each decay mode.

1.3 Experimental Status

Fig. 1.9 shows the momentum distributions of charged decay products from K^+ decay at rest. The $K^+ \to \pi^+\gamma\gamma$ momentum spectrum with $O(p^6)$ corrections at $\hat{c} = 1.8$ is also shown in the figure. The major background to this decay mode is $K^+ \to \pi^+\pi^0$ decay with $\pi^0 \to \gamma\gamma$ (called $K_{\pi 2}$ hereafter), since the final state is identical to $K^+ \to \pi^+\gamma\gamma$ and the branching ratio is large (21%). The $K_{\pi 2}$ decay is a two-body decay and the π^+ momentum is monochromatic (205 MeV/c). The energy and direction of photons from π^0 are also different from those from $K^+ \to \pi^+\gamma\gamma$. The BNL-E787 experiment, which is the predecessor of E949, therefore divided the search region into two in order to avoid this background: one is "above $K_{\pi 2}$" and the other is "below $K_{\pi 2}$". E787 collected data in 1991 in order to study $K^+ \to \pi^+\gamma\gamma$. There was no candidate event in the above-$K_{\pi 2}$ region and only the 90%C.L. upper limit was set by assuming the phase-space distribution:

$$Br(K^+ \to \pi^+\gamma\gamma) < 5.0 \times 10^{-7} \quad . \tag{1.22}$$

In the below-$K_{\pi 2}$ region, 31 candidate events were observed with an expected background of 5.1 ± 3.3. The partial branching ratio was obtained to be

$$Br(K^+ \to \pi^+\gamma\gamma, 100\text{MeV/c} < P_{\pi^+} < 180\text{MeV/c}) = (6.0 \pm 1.5 \pm 0.7) \times 10^{-7}, \tag{1.23}$$

where the first uncertainty is statistical and the second one is systematical. The measured π^+ momentum spectrum is shown in Fig. 1.10 and was compared with the ChPT predictions. The result reproduced the ChPT predictions, while it was totally inconsistent with the phase-space distribution. A maximum likelihood fit to the data was performed to determine the value of $\hat{c}$. Without $O(p^6)$ corrections, the result was obtained to be $\hat{c} = 1.6 \pm 0.6$. With $O(p^6)$ corrections, the result was $\hat{c} = 1.8 \pm 0.6$ with a better χ^2. The data thus favors an inclusion of the $O(p^6)$ corrections, but are still consistent with $O(p^4)$.

As we have shown in the previous section, one of the consequence of the $O(p^6)$ corrections is a nonzero amplitude at the kinematic end point. It is therefore desired to search for this decay in the above-$K_{\pi 2}$ region in order to prove the existence of the $O(p^6)$ corrections conclusively. $O(p^4)$ with $\hat{c} = 1.6$ predicts the branching ratio for the region at $P_{\pi+} > 213$MeV/c to be 4.9×10^{-10}, while $O(p^6)$ with $\hat{c} = 1.8$ predicts 6.1×10^{-9}; the latter is one order of magnitude larger than the former, and within the sensitivity that the E949 experiment can reach.

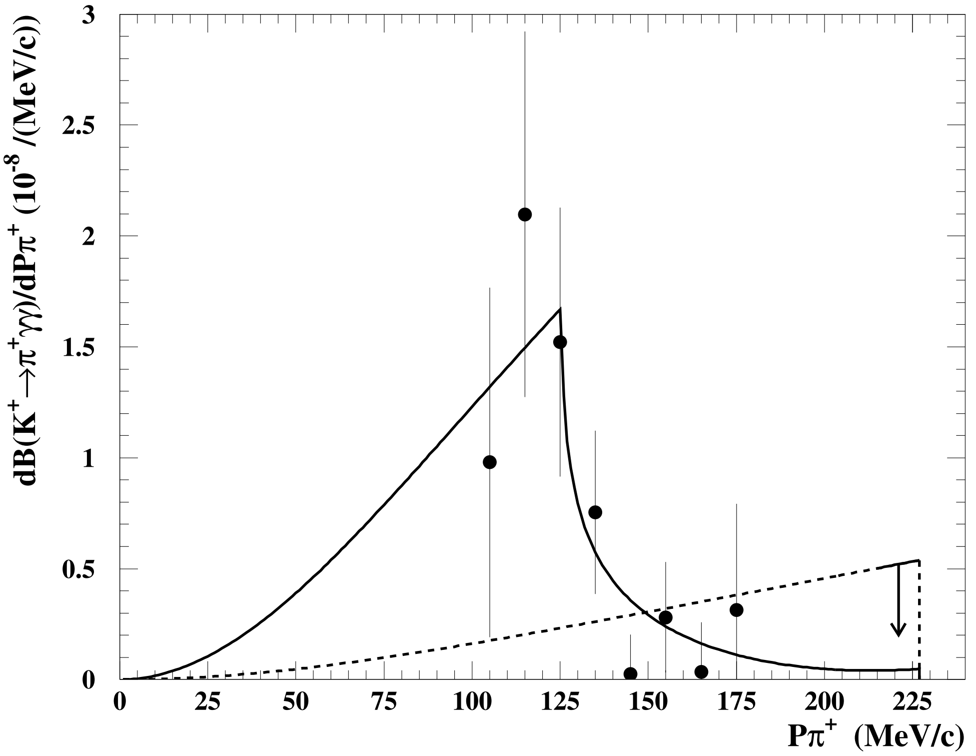

Figure 1.10: Measured π^+ momentum distribution in E787-1991 [6]. The solid line is the best fit to the data; the dashed line shows the phase-space distribution.

Chapter 2

BNL-E949 Experiment

In this chapter, the E949 experiment and the data used in this analysis are described. The experiment was carried out at the Brookhaven National Laboratory (BNL) using the Alternating Gradient Synchrotron (AGS) and the E949 detector. The experiment is overviewed in section 2.1. The production of a high-intensity kaon beam using AGS and transportation of the beam to the E949 detector are discussed in section 2.2. Each detector subsystem is described in sections 2.3, 2.4 and 2.5. The trigger, data-acquisition system and collected data set used in this analysis are explained in section 2.6.

2.1 Overview of the Experiment

The E949 experiment at BNL was primarily designed to measure the rare kaon decay $K^+ \to \pi^+\nu\overline{\nu}$, whose branching ratio is predicted to be 10^{-10} in the Standard Model. The experiment is a successor to E787, which succeeded to observe the decay for the first time with two signal events in total. Various improvements were made to E787 in order for E949 to reach a sensitivity of 10^{-11} [1]. E949 started data taking in 2002, and an additional candidate event for $K^+ \to \pi^+\nu\overline{\nu}$ was observed in the data set. Based on these three events, the branching ratio was determined to be $1.47^{+1.30}_{-0.89} \times 10^{-10}$ [19].

Fig. 2.1 shows a schematic sideview and endview of the upper half of the E949 detector. A high-intensity kaon beam is transported to the E949 detector as indicated in Fig 2.1 (a). E949 detects kaon decays at rest, and is called a "stopped kaon" experiment. An incident kaon comes to rest and decays in the Target, which is located at the center of the detector. The time difference between an incoming kaon and an outgoing charged decay product is required to be larger than a few nsec; such a "delayed-coincidence" requirement guarantees that the kaon actually decayed at rest, and suppresses the background processes that are due to pions that are in the incident beam, scatter, and enter into the detector, and due to incident kaons that decay before coming to rest. The detector is situated in a 1 Tesla magnetic field parallel to the beam axis, and the momentum of charged decay products is measured with a cylindrical drift chamber that surrounds the Target. The particles come to rest in the Range Stack consisting of 19 layers of plastic scintillators. The range and kinetic energy of charged decay products are measured in the Range Stack. The pulse

[1] One of the upgrades is the Level-0 trigger system, which is described in Appendix G.

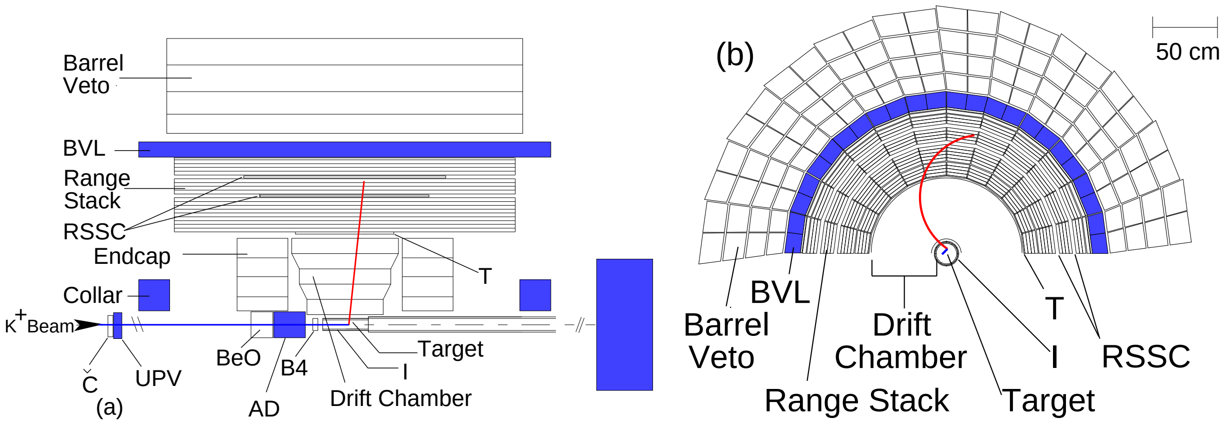

Figure 2.1: Schematic sideview (a) and endview (b) of the upper half of the E949 detector. The shaded parts of the figure are newly installed for E949, as will be described in section 2.6.

shapes of both ends of each Range Stack counter are recorded by 500-MHz transient digitizers (TDs) in order to observe the $\pi^+ \to \mu^+ \to e^+$ decay chain. By performing a pulse-shape analysis, the TD system can identify whether the charged decay product is a pion or not. Photon detectors cover the 4π solid angle; the barrel region is covered by the Barrel Veto Liner and Barrel Veto, which are lead-scintillator sampling calorimeters, and the region along the beam axis is covered by the endcaps of un-doped CsI crystals. The remaining gaps near the beam axis are covered by additional photon detectors: the collar, microcollar, upstream photon veto, active degrader, and downstream photon veto.

In summary, the functions of the E949 detector are categorized[2] as follows:

- Confirmation of an incident kaon that comes to rest and decays in the Target.
- Redundant measurement of the kinematics (momentum, range and kinetic energy) of a charged decay product.
- Identification of π^+ with high accuracy.
- Hermetic photon detection.

The high-intensity kaon beam available from AGS and the functions of the E949 detector are suitable to study other kaon decays - in particular the decay $K^+ \to \pi^+\gamma\gamma$. Fig. 2.2 shows a sideview of the E949 detector in detail. The phototubes of the counters, except for those of the endcaps, are located outside of the magnet. The locations of the magnet coil and the phototubes of the various components are shown in the figure.

[2]These categories are useful in an offline analysis.

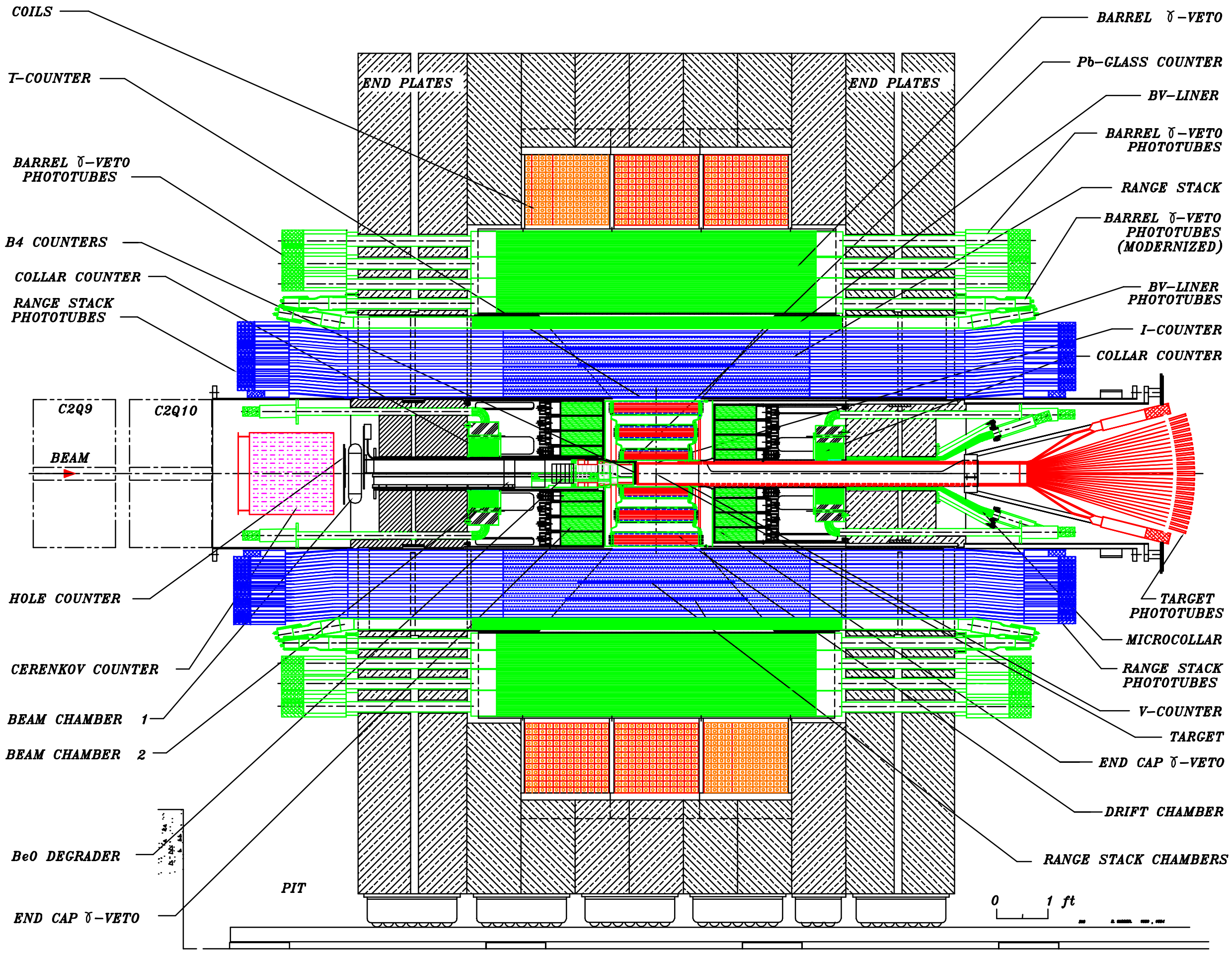

Figure 2.2: Sideview of the E949 detector.

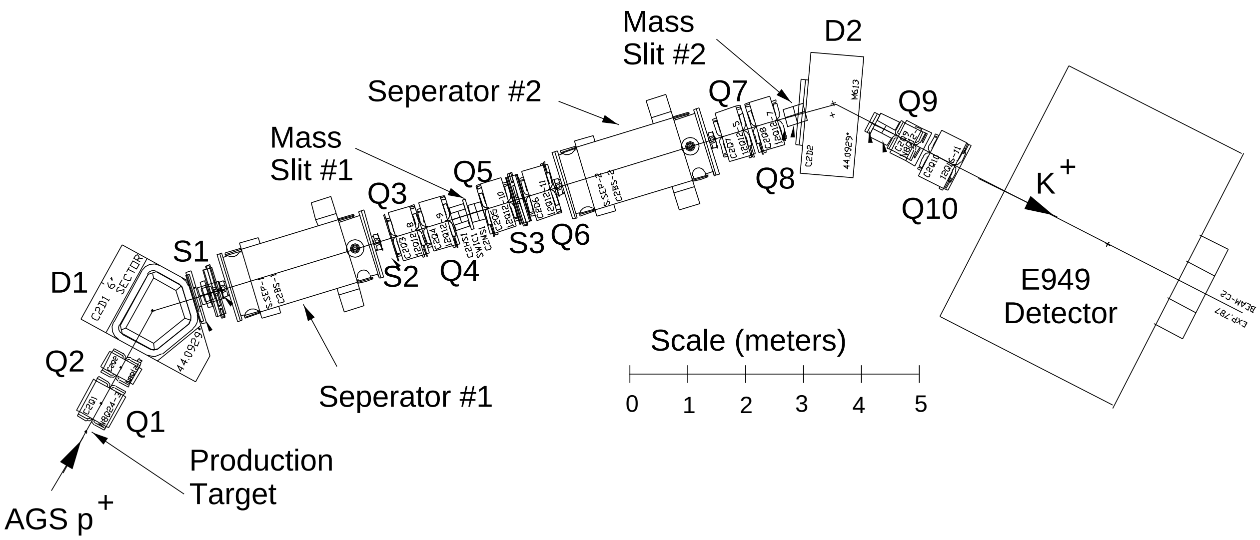

Figure 2.3: Top view of the LESB3 beamline. D1-2, Q1-Q10, S1-S3 and O1 denote dipole, quadrapole, hexapole and octapole magnets, respectively. The E949 detector is situated at the end of LESB3.

2.2 Kaon Production and Transportation

A high-intensity kaon beam with high purity is essential for this experiment, and the BNL-AGS has realized it. Protons are accelerated up to 22 GeV at AGS and slow-extracted to the "C4" beam line; kaons are produced by striking the protons to a production target of Platinum (see the left-bottom corner of Fig. 2.3). Secondary particles emitted toward the zero degree are transported to the E949 detector via the Low Energy Separated Beamline 3 (LESB3) [20], shown in Fig. 2.3. In order to select low-momentum kaons (< 800 MeV/c) within a narrow momentum range and to reduce other beam contaminations (mainly pions), LESB3 consists of various components: (1) a bending magnet called "D1" selects the momentum of secondary beam, (2) two electrostatic separators remove pion contaminations, (3) a mass slit follows each separator and selects the kaons, (4) a bending magnet called "D2" once again selects the beam momentum and (5) after Q9 and Q10, which are quadrapole magnets for focusing, the beam is delivered to the E949 detector.

During the E949-2002 run, AGS was operated typically at 70 Tera protons in each 2.2 s spill every 5.4 s, with a duty factor of 41%. After passing through the LESB3, the momentum of the transported beam was selected to be 710MeV/c and the kaon-to-pion ratio was 3:1.[3]

[3]The running conditions in 2002 run were not optimized because of a failure of the AGS power supply and a problem with one of the electrostatic separators. The conditions will be improved in future runs; according to the E949 proposal, the beam spill will be 4.1 s every 6.4 s (duty factor = 64%), the protons in AGS will be accelerated up to 24GeV, and the kaon-to-pion ratio will be 4:1.

2.3 Beam Line Instruments

In order to confirm that a kaon reaches the Target and there is no incoming particle at the decay time, a number of beam instruments are implemented (Fig. 2.4) between the Q10 magnet and the kaon stopping Target, which is located at the center of the detector. The Čerenkov counter, which is used to identify whether an incoming particle is a kaon or a pion, is located in the most-upstream region of the E949 detector. A schematic side view of the Čerenkov counter is shown in the left figure of Fig. 2.5. As illustrated in this figure, a charged particle that has a velocity β higher than $1/n$, where n is the index of refraction of the radiator, passes through the radiator and emits Čerenkov light with an angle of $\theta_{\check{C}}$. The angle $\theta_{\check{C}}$ is given by

$$\cos\theta_{\check{C}} = \frac{1}{\beta n}.$$

The angle $\theta_{\check{C}}$ is different for particles that have the same momentum, but different masses. By choosing an appropriate index of refraction of the radiator, so that the Čerenkov light produced by a pion is totally reflected, but the light by a kaon is not, the Čerenkov light is efficiently guided to the PMTs, which are labeled π or K in the figure. There are 14 PMTs for a kaon and 14 PMTs for a pion in the Čerenkov counter, and these are arranged as shown in the right figure of Fig. 2.5. By counting the number of PMT hits in each ring, an incoming particle can be identified. At the Čerenkov counter, typical beam rates for the kaon and pion are 12 MHz and 4 MHz, respectively.

After the Čerenkov counter, the beam passes through two Beam Wire Proportional Chambers (BWPC1 and BWPC2), as shown in Fig. 2.4. Each chamber has three planes: sense wires in one plane of BWPC1 are tensioned vertically (called the X-plane) and the wires in the other two planes are tensioned in the $\pm 45^\circ$ directions with respect to the vertical axis (called the U- and V-planes). Sense wires in one plane of BWPC2 are also tensioned vertically (called the X-plane) and the wires in the other two planes are tensioned in the $\pm 60^\circ$ directions with respect to the vertical axis (called the U- and V-planes). Endviews of the BWPCs are shown in Fig. 2.6

After the BWPCs, the beam is slowed down by a degrader such that it comes to rest in the Target. The degrader consists of two parts: an inactive degrader (BeO) and an active degrader (AD), as shown in Fig. 2.4. In order to minimize multiple scatterings, beryllium oxide, which has a relatively high density and a small atomic number, is used for the inactive degrader. AD is constructed of 40 layers of 2 mm-thick scintillator disks and 2.2-mm thick copper disks. AD can be used as a detector for photons that come from kaon decay in the Target and escape to the upstream direction.

The last beam instrument located between AD and Target is B4 counter, which is a hodoscope of two layers. Each layer is divided into 16 elements in the $\pm 33.5^\circ$ direction with respect to the horizontal axis, as shown in the left figure of Fig. 2.7. Each hodoscope element is made of pairs of scintillators that are displaced by 3.65 mm from each other, as shown in the right figure of Fig. 2.7. Since a kaon is slowed down by the degraders, a large amount of energy is expected to be deposited in the B4 counter. On the other hand, a pion still has a high velocity due to its lighter mass, and should deposit a smaller energy. The B4 counter can therefore be used to identify the beam particle as a kaon.

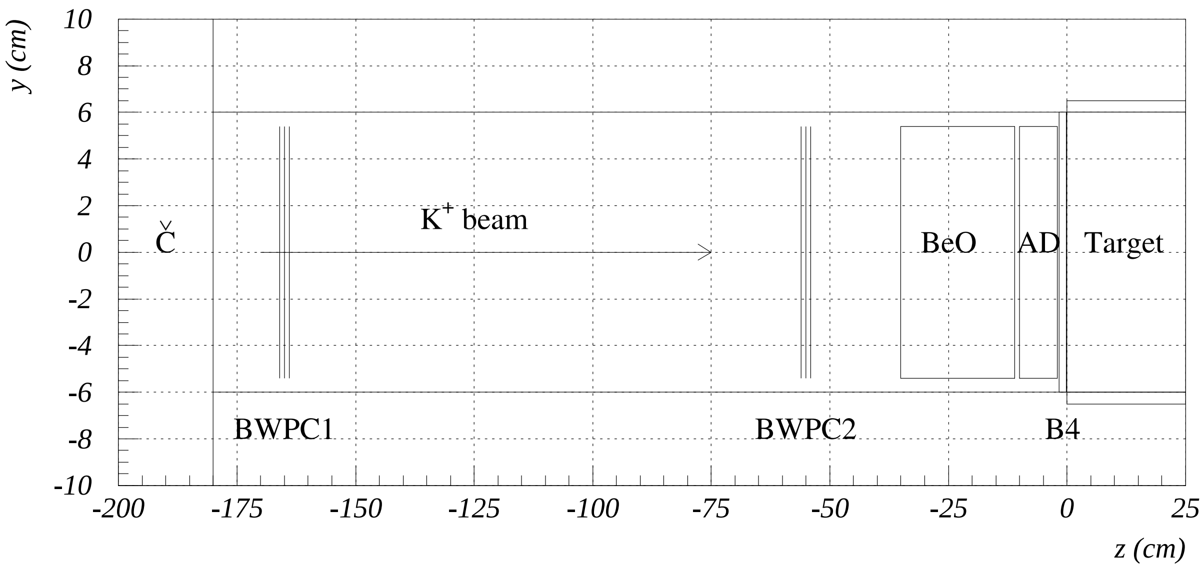

Figure 2.4: Sideview of the configuration of the beam-line instruments. The beam comes from left to right, as indicated by the arrow in the figure.

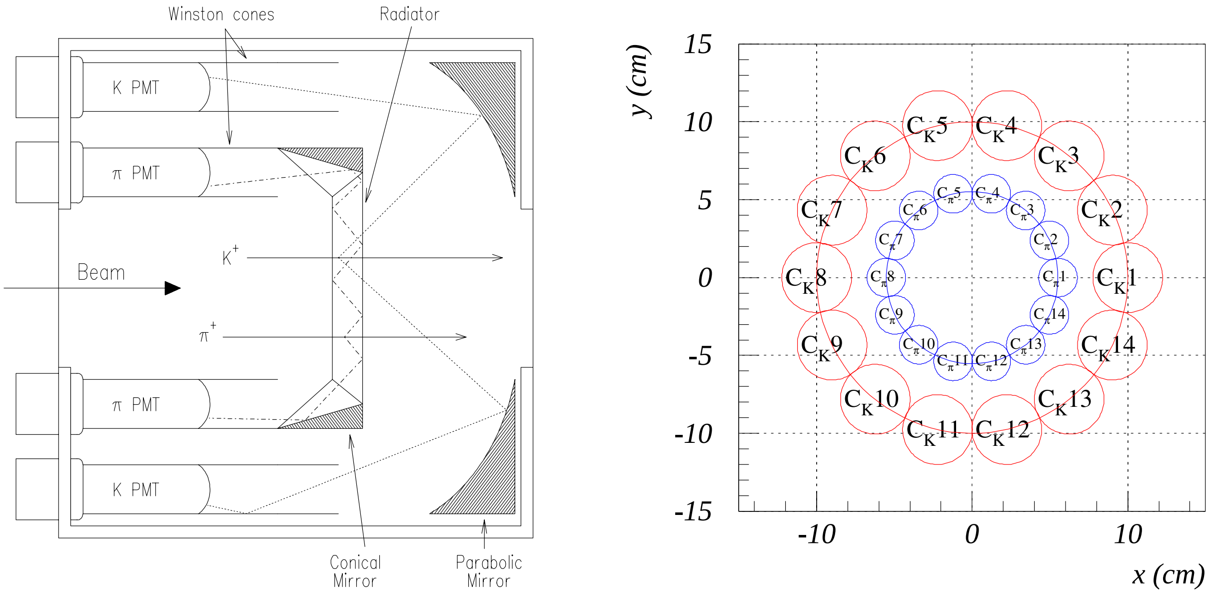

Figure 2.5: Schematic sideview of the Čerenkov counter (left) and endview of the PMT configuration (right).

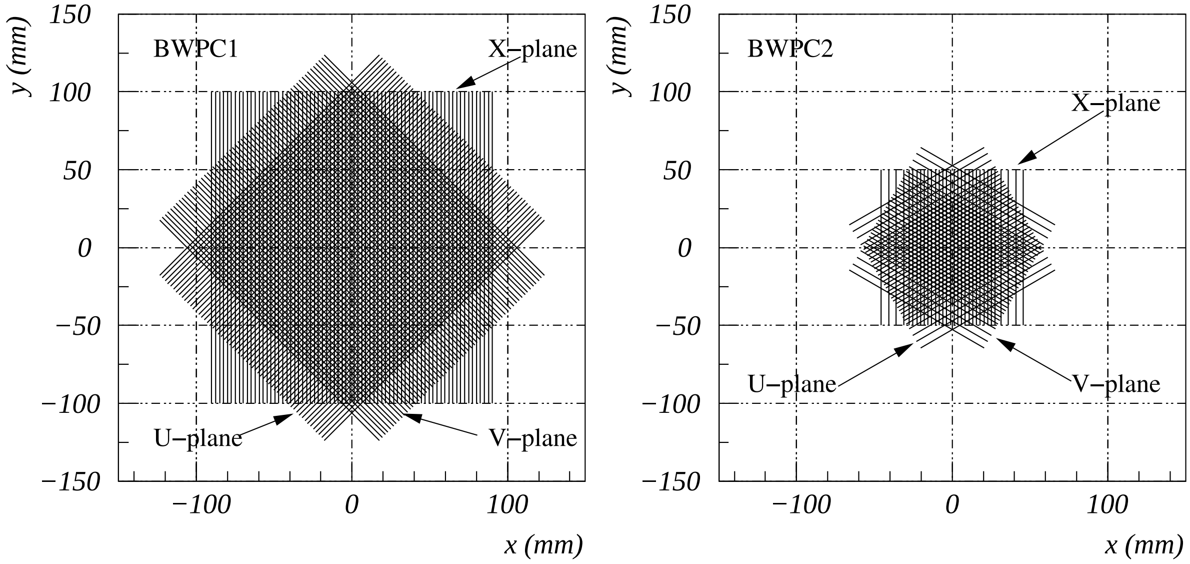

Figure 2.6: Endviews of BWPC1 (left) and BWPC2 (right).

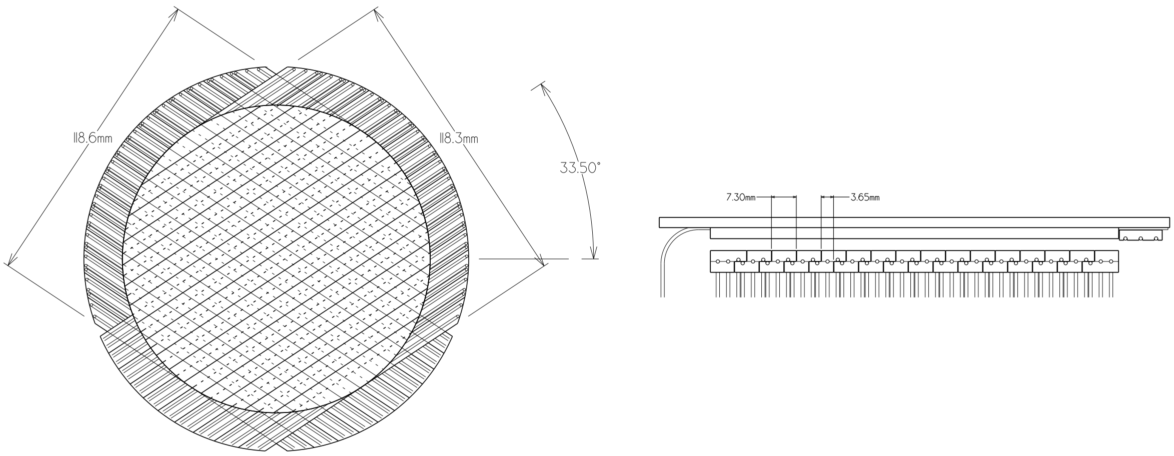

Figure 2.7: Schematic endview (left) and topview (right) of the B4 counter.

2.4 Kaon Stopping Target

After the B4 counter, the kaon beam enters and comes to rest in the kaon stopping Target, which is a bundle of plastic scintillating fibers. The left figure of Fig. 2.8 shows an endview of the Target. The Target is composed of 413 5mm $\times$ 5mm scintillating fibers.[4] Each Target fiber is 3.1 meters in length, and is instrumented with a PMT at the downstream end. PMT signals are sent to the ADC, TDC and 500 MHz CCD-based transient digitizers (CCD's) [21] so that the timing, energy and pulse-shape information can be recorded.

As described in section 2.1, the delayed-coincidence requirement is effective to discriminate kaon decays at rest from backgrounds of pion scattering or kaon decay-in-flight. In an offline analysis, the fibers are classified into hits due to kaons or hits due to charged decay products using information concerning their time and energy. The averaged time of the fibers due to the charged decay product is required to be at least 2 nsec later than the average time of the kaon fibers. The details of the Target reconstruction in the offline analysis are described in section 3.2.1. A typical event display in the Target is shown in the bottom-left of Fig. 3.3.

The fiducial region in the beam direction is defined by six I-counters and six V-counters, which are made of plastic scintillators with a thickness of 6.4 mm and 5.0 mm, respectively. The I-counters surround and support the Target, and the V-counters surround the light guides of the I-counters (right figure of Fig. 2.8). All of the reconstructed events should have I-counter hits from a charged decay product, and should not have other hits in the I-counters and the V-counters. Thus, the fiducial region of the Target in the beam direction is determined to be 24.2cm.

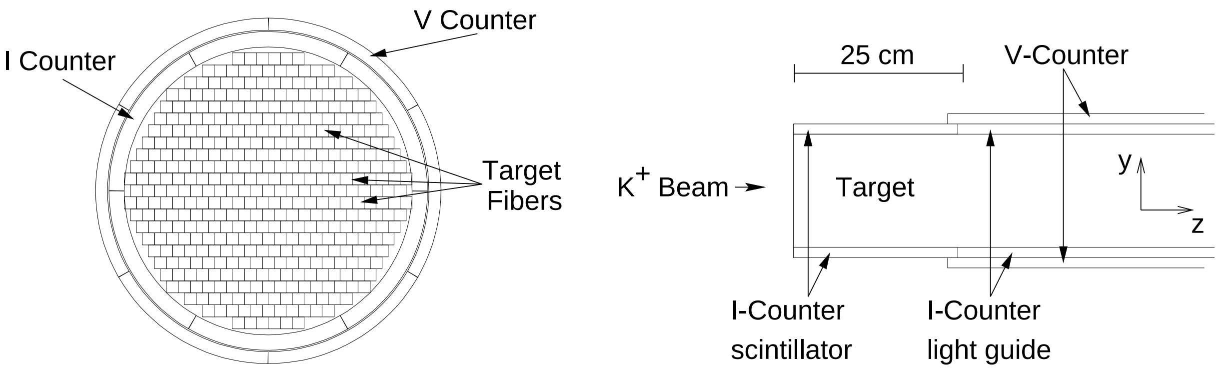

Figure 2.8: Schematic sideview (left) and endview (right) of the Stopping Target, I-counters and V-counters.

[4]The peripheral region of the Target is filled with smaller fibers in order to maximize the active region. The overall shape of the cross-section of the Target is a circle with a diameter of 12 cm.

2.5 Charged Track Measurement

2.5.1 Drift Chamber

After leaving the Target, a charged decay product enters a Drift Chamber, called Ultra Thin Chamber (UTC) [22]. The UTC is cylindrical with a length of 51 cm in the beam direction and a radius of 43 cm. The momentum of a charged decay product is measured with the UTC from the track curvature in a 1-Tesla magnetic field parallel to the beam axis. A schematic view of the UTC is shown in Fig. 2.9. In order to reduce multiple scatterings and to achieve better momentum resolution, the UTC is designed to minimize the amount of materials.[5] The UTC has five layers, separated by kapton cathode foils, which are supported by the difference in the gas pressures between neighboring layers. Three active "superlayers", each of which is filled with a mixture of Argon-Ethane-Ethanol gases (49.6:49.6:0.8) and two inactive regions between the superlayers are filled with a nitrogen gas. Each superlayer consists of four layers of square drift cells having dimensions of 11 mm $\times$ 19 mm. A cell consists of one Tungsten sense-wire surrounded by eight aluminum cathode-wires. In the x-y plane (perpendicular to the beam axis), a charged decay product is reconstructed by fitting a circle to the positions from the sense-wire hits.[6] In order to reconstruct a charged decay product in the beam direction, the cathode foils have copper strips tilted at 45° with respect to the beam direction (z). The cathode hits are fitted by a straight line in the r-z plane, and the polar angle of the charged decay product can be obtained. The details concerning the Drift Chamber reconstruction in the offline analysis are described in section 3.2.1. The momentum resolution has been achieved to be $\delta P/P \sim 1.2\%$ from the monochromatic π^+ from $K_{\pi 2}$ decay (refer to Fig. 3.4).

2.5.2 Range Stack

After the UTC, a charged decay product is slowed down and comes to rest in Range Stack (RS) counters consisting of 19 layers of plastic scintillators segmented into 24 azimuthal sectors. The range and kinetic energy are measured in the RS.[7] The scintillator where the charged decay product comes to rest is called the stopping counter. Each RS counter is made of a scintillator plate with a length of 1.82 m and a thickness of 1.905 cm, except for the inner-most and the outer-most layers, which are 0.52 m and 1.82 m in length and 0.700 cm and 0.9525 cm in thickness, respectively. The inner-most layer is called the T-counter, whose length defines the fiducial region in which a charged decay product should pass through. There are two straw chambers, called Range Stack Straw Chambers (RSSCs), in the RS. The inner (outer) RSSC is located between RS layer 10 and 11 (14 and 15). The trajectory of a charged decay product in the RS is reconstructed with the RSSC hits for a refined range measurement. The details of the Range Stack reconstruction in the offline analysis have been described in section 3.2.1. The range and energy resolutions

[5] The total thickness of UTC is 3×10^{-2} radiation lengths.

[6] The mean drift velocity is 5cm/μm and the gain is 8.0×10^4.

[7] The energy losses in the Target should be taken into account in order to obtain the "total" momentum, range and kinetic energy of the track at the decay point.

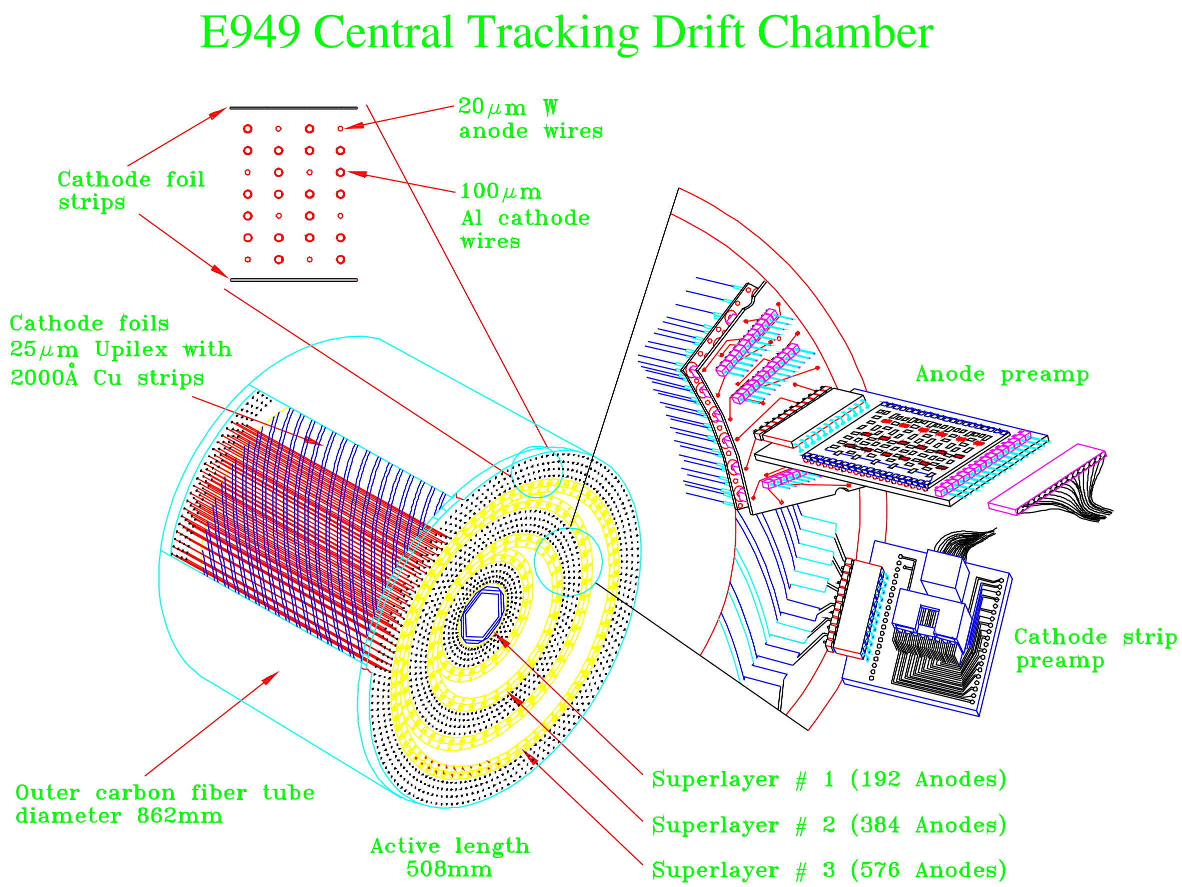

Figure 2.9: Schematic view of the Drift Chamber.

are achieved to be 3.3% and 2.9%, respectively, from monochromatic π^+ from $K_{\pi 2}$ decay (refer to Fig. 3.4).

Signals from the RS counters are read out by PMTs and recorded at both ends by ADCs, TDCs and 500-MHz Transient Digitizers (TDs) [23]. The pulse shapes recorded by the TDs are used to identify the $\pi^+ \to \mu^+ \to e^+$ decay chain in the stopping counter. Fig. 2.10 shows an example of $\pi^+ \to \mu^+ \to e^+$, which is recorded by TDs at the upstream and downstream ends of the RS counters from layer 11 through 14. Since a muon in $\pi^+ \to \mu^+\nu$ has a monochromatic kinetic energy of 4 MeV, most of the muons come to rest and decay in the stopping counter. A positron from the muon decay can penetrate to the outer layers. In Fig. 2.10, only a pion is recorded at layer 11 (inner most). A muon from the pion decay and a positron from the muon decay are recorded at layer 12, which is the stopping counter. The positron then passes through layers 13 and 14. In an offline analysis, double and single-pulse fittings are performed to the pulse shapes in the stopping counter. By comparing the fitting qualities, the charged decay product is identified as being a pion or not. A typical fitting result is shown at the bottom-right of Fig. 3.3. In order to find a positron from muon decay, the TD and TDC signals from counters other than the stopping counter are used.[8] This helps to remove any events that

[8]The TD pulse shape is recorded up to 2 μsec. The TDC information is recorded up to 10 μsec.

mimic a $\pi^+ \to \mu^+ \to e^+$ decay chain due to a "fake" pulse, at a muon time or a positron time in the stopping counter, made by accidental particles.

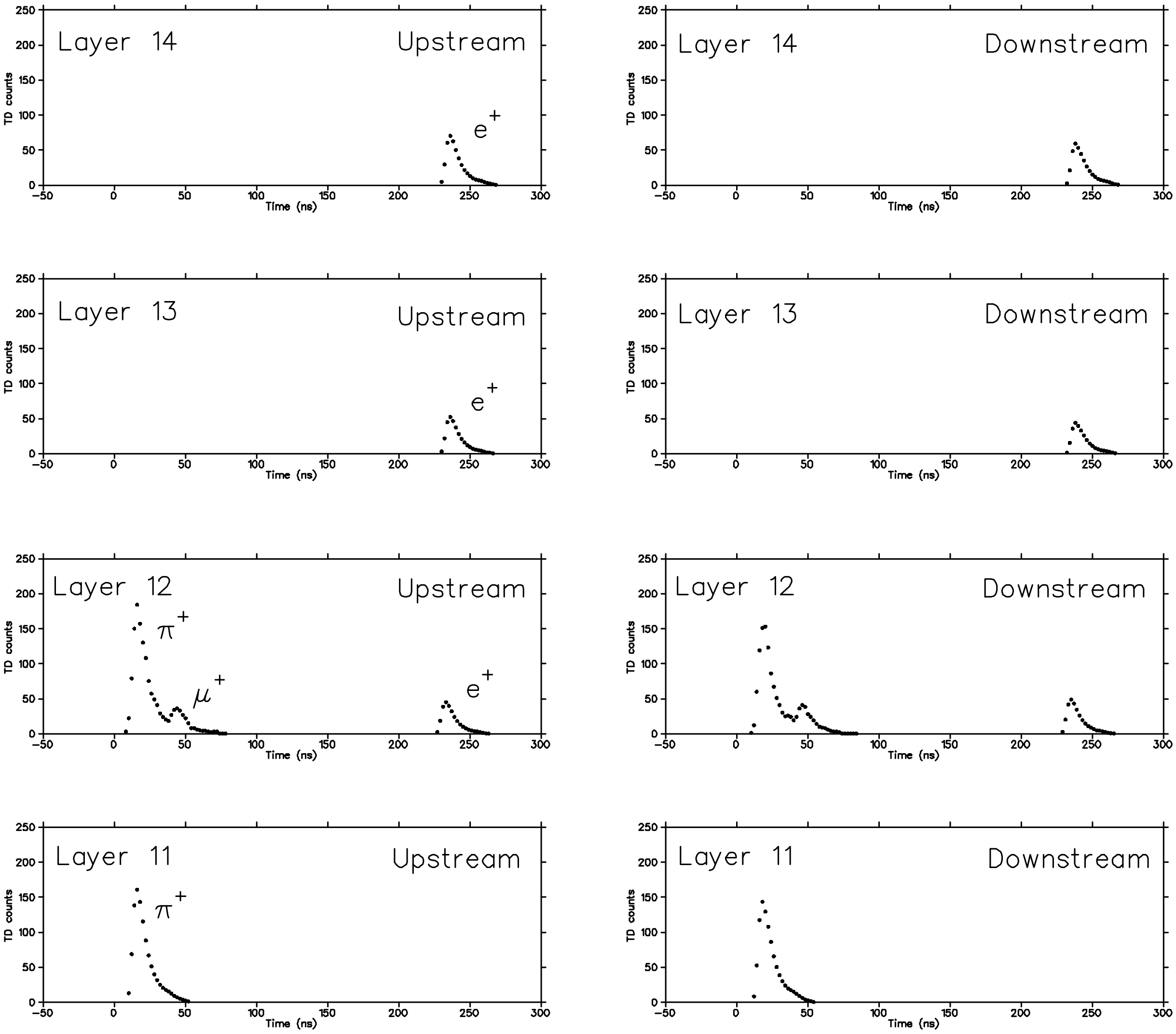

Figure 2.10: Example of the $\pi^+ \to^+ \mu \to e^+$ decay chain recorded by TDs.

2.6 Photon Detector

2.6.1 Barrel Photon Detector

The photon detector in the Barrel region consists of two parts, which are called Barrel Veto Liner (BVL) and Barrel Veto (BV). These detectors are used to reconstruct photons in an offline analysis, although these are primarily designed as a detector to remove the $K^+ \to \pi^+\pi^0$ background to $K^+ \to \pi^+\nu\bar{\nu}$ by catching photons from π^0. This function of the photon detector is called "photon veto". The BVL, which was installed to the detector for E949, is located just outside the RS, as shown in Fig. 2.11. The BVL is a sandwich-type electromagnetic calorimeter made of 1 mm-thick lead and a 5 mm-thick plastic scintillator, and is segmented to 48 sectors azimuthally. Each RS sector corresponds to two BVL sectors. One BVL module consists of 13 plastic scintillator sheets and 12 lead sheets, and has a length of 220 cm to the beam direction. The thickness in the radial direction is 2.3 radiation lengths in total. The BV is located outside of the BVL, as shown in Fig. 2.11. The BV is a sandwich-type electromagnetic calorimeter, as well as the BVL, made of 1 mm-thick lead and a 5 mm-thick plastic scintillator, like BVL, and is segmented to 48 sectors azimuthally and 4 layers radially. One BV module in each layer consists of 16, 18, 20 and 21 lead/scintillator layers, and is 190 cm in length to the beam direction. The length in the radial direction is 14.3 radiation lengths in total. The boundaries are tilted so that the photons that come from the Target do not escape.

Signals from each BVL or BV counter are read out by the ADCs and TDCs. In an offline analysis, the adjacent counters that have a timing close to the time of a charged track are grouped to be a photon cluster. Because of the sampling structure, the energy deposit recorded by the ADCs is a fraction of the photon energy, and must be corrected in order to measure the energy. This correction factor is called the "visible fraction", and is about 30%. The details of the photon reconstruction in the offline analysis are described in section 3.2.2.

2.6.2 CsI Endcaps

There are two endcaps (ECs) [24], which are located at the upstream and downstream ends of the UTC, as shown in Fig. 2.12. Each EC consists of four rings, which are formed by pentagonal-shape undoped-CsI crystals, as can be seen in Fig. 2.12. The numbers of crystals are 13, 14, 21 and 27 for the upstream endcap, and 11, 13, 19 and 25 for the downstream endcap, respectively. Each CsI crystal is instrumented with 3-inch fine-meshed PMTs except for the inner-most rings, which are with 2-inch fine-meshed PMTs [25]. The PMT was designed to work in a high magnetic field. This subsystem is used for photon veto in this study.

2.6.3 Other Photon Detectors

The gaps near the beam axis are covered by a collar, a microcollar, an upstream photon veto, an active degrader and a downstream photon veto. In addition, the Target, RS, I-counters and V-counters, except for the counters with a hit due to a charged decay product, can be used for photon veto.

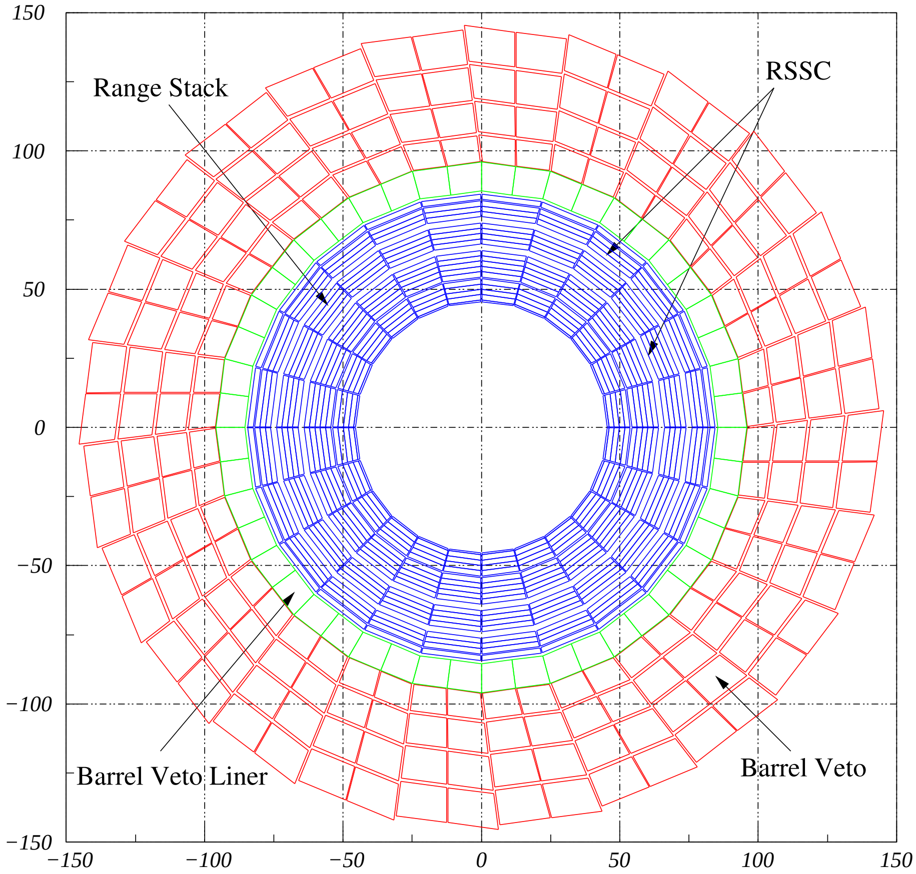

Figure 2.11: Schematic endview of the E949 detector: Range Stack (RS), Range Stack Straw Chamber (RSSC), Barrel Veto Liner (BVL) and Barrel Veto (BV).

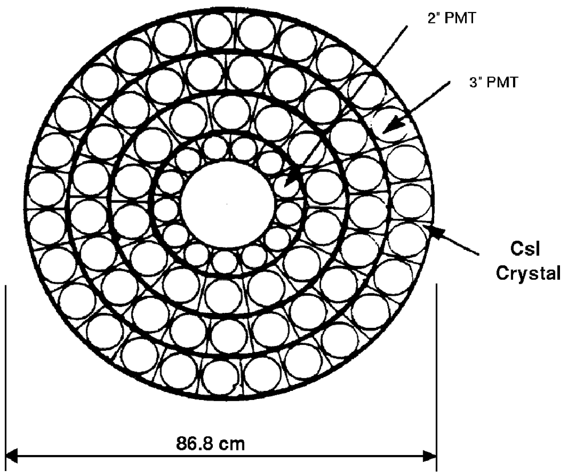

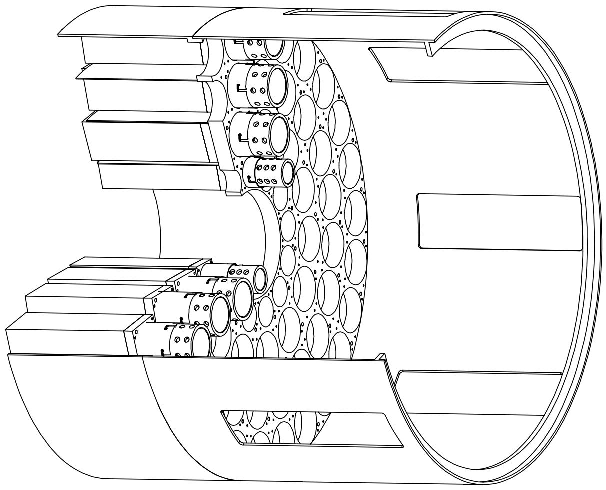

Figure 2.12: Schematic endview (left) and backview (right) of the endcaps (EC).

2.7 Trigger, Data Acquisition and Collected Data

2.7.1 $K_{\pi\gamma\gamma}$ Trigger

In order to detect $K^+ \to \pi^+\gamma\gamma$ above the $K_{\pi2}$ region, the trigger conditions for $K^+ \to \pi^+\gamma\gamma$ in E949 ($K_{\pi\gamma\gamma}$ trigger) were designed as follows.

- Kaon comes to rest and decays in the Target:

  A kaon enters the detector and reaches the Target. This trigger bit is labeled as K_B, which has coincident hits of the Kaon Čerenkov counter, the B4 counter and the Target. In order to ensure that the kaon comes to rest and decays in the Target, an I-counter hit is required to be at least 1.5 nsec later than that of a Kaon Čerenkov. This trigger bit is called online delayed-coincidence, labeled as DC.

- A charged decay product, which has a longer range than that expected for the $K_{\pi2}$ decay:

  A charged decay product entering the RS is ensured by the trigger bit labeled as $T \bullet 2$, which is a coincidence of the first and second inner-most layers of the RS in the same sector. The online stopping layer is required to be 16 or 17, in order to reduce the $K_{\pi2}$ decay that typically comes to rest in layer 12. The online stopping sector should be associated with a $T \bullet 2$ by the trigger bits, labeled as n_{ct}, where n is the layer number and "*ct*" designates the RS sectors that are in the $T \bullet 2$ sector or in the next two clockwise sectors; this is the direction that a positively-charged particle passes through in a magnetic field.

- Online π^+ identification:

  Online particle identification (PID) is performed by using the TD information. The ratio of the pulse height to the area in each end of the stopping counter is used to find a secondary pulse due to μ^+. A control board with Application Specific Integrated Circuits (ASICs) was implemented on each TD board, and the decision time was 15∼20 μsec.

- An electromagnetic shower in the Barrel region:

  An activity due to photon hits in both BVL and BV is required. There should be no activity in the RS counters that are not related to the charged decay product and in the EC. Note that the number of photon clusters is not counted in the trigger.

A logical expression of the $K^+ \to \pi^+\gamma\gamma$ trigger ($K_{\pi\gamma\gamma}$) conditions is written as follows:

$$K_{\pi\gamma\gamma} = K_B \cdot T \bullet 2 \cdot \mathrm{DC} \cdot (6_{ct} - 16_{ct}) \cdot \overline{18_{ct} - 19_{ct}} \cdot \mathrm{BV} \cdot \mathrm{BVL} \cdot \overline{\mathrm{EC}} \cdot \overline{\mathrm{RS}} \cdot \mathrm{PID}$$

2.7.2 Monitor Triggers

In addition to the $K_{\pi\gamma\gamma}$ trigger, there are monitor triggers for the purpose of calibration and normalization. The trigger conditions to collect the $K_{\pi 2}$ decay, $K_{\mu 2}$ decay and the beam π^+ that scatters and enters RS (π_{scat}) are as follows:

$$K_{\pi 2} = K_B \cdot T \bullet 2 \cdot \mathrm{DC} \cdot (6_{ct} + 7_{ct}) \cdot \overline{19_{ct}} \cdot \overline{\mathrm{RS}} \cdot \mathrm{PID},$$

$$K_{\mu 2} = K_B \cdot T \bullet 2 \cdot (6_{ct} + 7_{ct}) \cdot 19_{ct},$$

$$\pi_{scat} = \pi_B \cdot T \bullet 2 \cdot \overline{\mathrm{DC}} \cdot (6_{ct} + 7_{ct}) \cdot \overline{\mathrm{BV}} \cdot \overline{\mathrm{BVL}} \cdot \overline{\mathrm{EC}} \cdot \overline{\mathrm{RS}}.$$

The trigger bit, labeled as π_B, is the same one as the K_B bit, except that the Kaon Čerenkov hit is replaced by the Pion Čerenkov hit. The monitor trigger, which requires only K_B, is also prepared in order to count the number of kaons at rest and to measure the $T \bullet 2$ efficiency (explained section 5.2).

2.7.3 Data Acquisition and Collected Data

The E949 Data Acquisition (DAQ) system is based on Fastbus, with front-end readout into the SLAC Scanner Processors (SSP), as shown in the Fig. 2.13. The system has four Cable Segments, and the data are transferred via the Cable Segments to the VME processors (200 MHz Power PC's). The data are then transferred, during the spill-to-spill intervals, from the VME processors to the 4-CPU SGI Origin 200 computer. The data are written to magnetic tapes between spills.

During the E949-2002 run, the DAQ was typically operated at a 10 MByte/sec data transfer speed and 74% live time. The data for $K^+ \to \pi^+\gamma\gamma$ were taken from April 24 (run number 49036) to June 9 (run number 50218), 2002, simultaneously with the data taking for $K^+ \to \pi^+\nu\bar{\nu}$, which started on March 9 (run number 47592) and ended on June 9 with a beam break from April 6 to 17. The trigger rate for $K_{\pi\gamma\gamma}$ was 20 events/spill without prescaling and 1.1×10^7 triggers were accumulated in total. The monitor data were collected simultaneously with appropriate prescale factors so that the average number of events per spill would be ~ 10 in total. While the $K_{\pi\gamma\gamma}$ trigger was active, 1.2×10^{12} [9] K_B hits were counted in the scaler. This number was used to calculate the single-event sensitivity of this analysis.

[9] 1.8×10^{12} K_B hits were counted in the scaler while the $K^+ \to \pi^+\nu\bar{\nu}$ trigger was active.

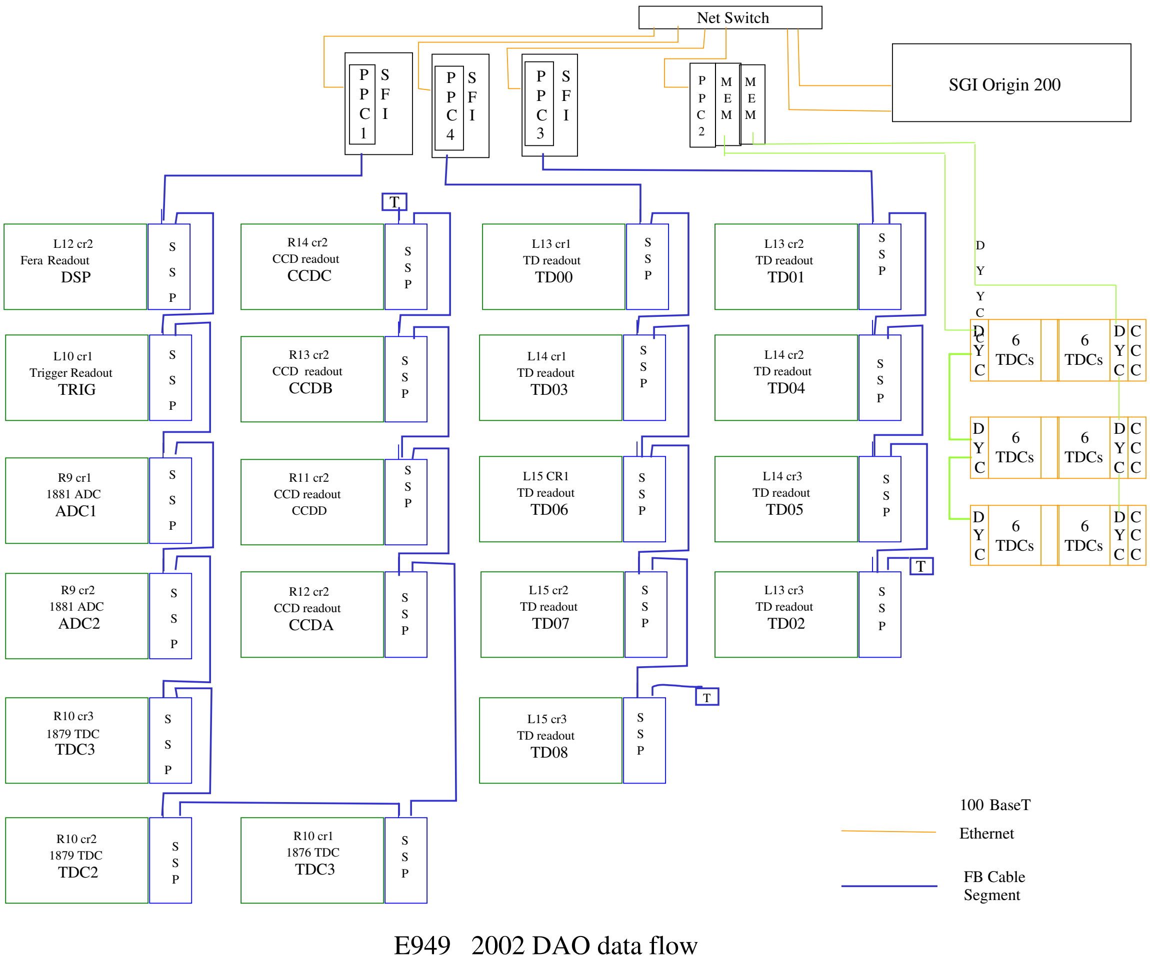

Figure 2.13: Block diagram of the E949 Data Acquisition System.

Chapter 3

Offline Analysis

In this chapter, details of the offline analysis are described. After overviewing the analysis in section 3.1, the reconstruction of the charged track and the photons in the final state is explained in section 3.2. The background sources are categorized in section 3.3, and the analysis methods used in the background estimation are described in section 3.4.

3.1 Overview of the Offline Analysis

The goal of offline analysis is to select the $K^+ \to \pi^+\gamma\gamma$ signal, which is defined to be the events that remain in the search region after imposing all of the selection criteria (Cuts). For this purpose, the offline analysis is divided into various steps. The first step is reconstruction of the charged track and the photons in each event. The next step is a background estimation. As described in later chapters, the expected sensitivity is just below the ChPT prediction, which means that the expected signal events to be observed is a handful of events, or zero. In order to have confidence in the observed signal events, it is important, not only to suppress the background to be much smaller than one event, but also to understand the mechanisms of the background. During the course of the background estimation, the real data instead of a Monte-Carlo simulation is used so that "rare" background processes, which could not be reproduced in simulation, and the "artifact" backgrounds due to hardware problems etc during the data taking can be correctly taken into account. In order to avoid any bias in tuning the Cuts, the real data are divided into uniformly-sampled one-third and two-third portions. The Cuts are studied and frozen with the one-third sample, and the background level in the search region is estimated with the remaining (and independent) two-third sample by using a special technique, named the "bifurcation method", explained in section 3.3. Historically, this method was developed by the BNL-E787 experiment in order to estimate the background level for the $K^+ \to \pi^+\nu\bar{\nu}$ decay without relying a Monte-Carlo simulation. The concept was developed during the E787 studies in Phase-1 (with the data sets from 1988 to 1991); the scheme was established in the E787 analysis with the 1995 data set, which succeeded as the first evidence for $K^+ \to \pi^+\nu\bar{\nu}$ [26]. Since that time, the method has been used in E787 and E949 in order to estimate the background level for $K^+ \to \pi^+\nu\bar{\nu}$ and other rare-kaon decay modes with the real data. The search region should always be masked out in the above samples, because a bias could easily be introduced by directly examining the small number of candidate events in the search region before determining the Cuts and the background level. The background sources are categorized by their mechanisms, and each background is characterized by a set of "background probability functions". These functions can be used for a confirmation of the validity of the background estimation as well as for a Likelihood analysis [27] (if the signal events were observed). After determining all of the Cuts and completing the background estimation, the signal events in the search region are examined. The signal events are defined if the following basic conditions are satisfied:

- A single K^+ comes to rest and decays in the Target. No extra beam particle should be observed at the decay time.
- The kinematic values (momentum, range and kinetic energy) of the charged decay product are higher than those of the π^+ from the $K_{\pi 2}$ decay, and are lower than those of the μ^+ from the $K_{\mu 2}$ decay.
- The charged decay product is definitely identified as a π^+.
- One or two photon clusters are reconstructed in the Barrel region, and there is no extra activity in other detector subsystems. In addition, the higher-energy photon cluster should be located opposite to the π^+ direction.

In the acceptance calculation for the single event sensitivity, we also use real data as much as possible. It should be noted that the events with one photon cluster are also accepted as signals, although the number of photons in the final state is two. The left figure of Fig. 3.1 is a scatter plot of the π^+ momentum and the cosine of the opening angle of two photons from a Monte-Carlo $K^+ \to \pi^+\gamma\gamma$ simulation with the assumption of ChPT with $O(p^6)$ corrections and $\hat{c} = 1.8$; the right figure of Fig. 3.1 is the distribution of the cosine of the opening angle of two photons for an event whose π^+ momentum is larger than 215 MeV/c. The opening angle between two photons from $K^+ \to \pi^+\gamma\gamma$ becomes narrower for events whose π^+ momentum is near to the kinematic end point. These photons could be fused and detected as a single cluster in the Barrel region, due to the limited position resolution of the detector. The left figure of Fig. 3.2 is the distribution of the number of reconstructed photon clusters in the Barrel Veto Liner and Barrel Veto from the Monte Carlo data.[1] About 50% of the events are reconstructed as "one-cluster" events in the detector. In addition, the higher-energy photon cluster should be opposite to the π^+ direction. The right figure of Fig. 3.2 shows the distribution of the cosine of the angle between π^+ and the higher-energy photon for the events, whose π^+ momentum is larger than 200 MeV/c. It is clear that the higher-energy photon tends to be emitted in the opposite direction to the π^+ at the kinematic end point.

[1] The Monte-Carlo software used to simulate the E949 detector is based on the EGS4 electromagnetic shower package [28] and the energy losses of charged particles with the Bethe-Bloch formula. The output data can be analyzed by the same analysis code as used for real data.

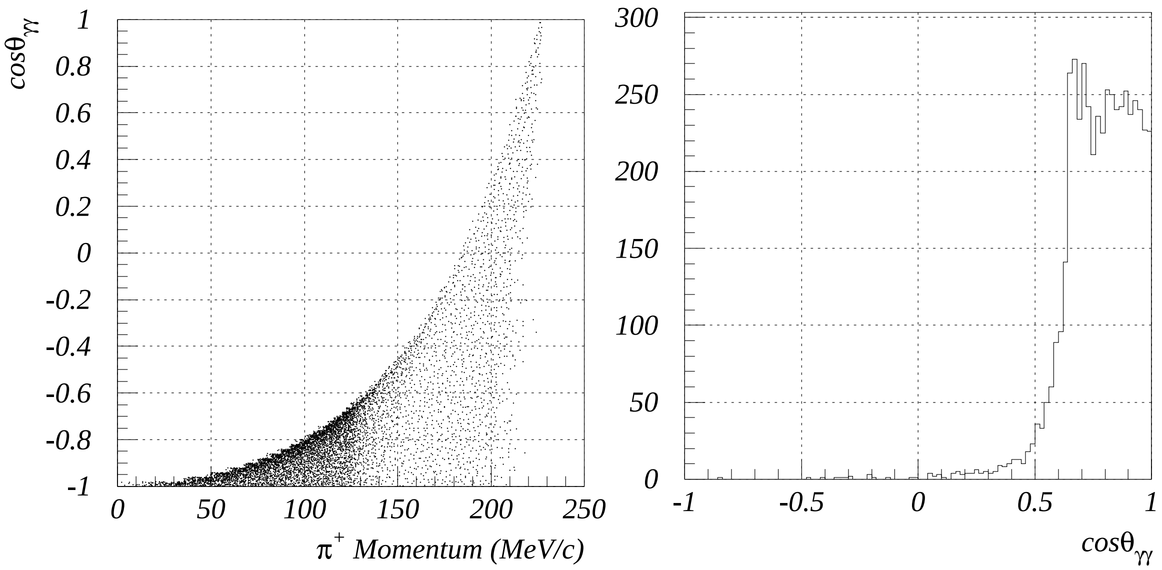

Figure 3.1: Scatter plot of the π^+ momentum and the cosine of the opening angle of two photons ($\cos\theta_{\gamma\gamma}$) from the Monte-Carlo $K^+ \to \pi^+\gamma\gamma$ events without detector simulation (left); the distribution of $\cos\theta_{\gamma\gamma}$ for events whose π^+ momentum is larger than 215 MeV (right).

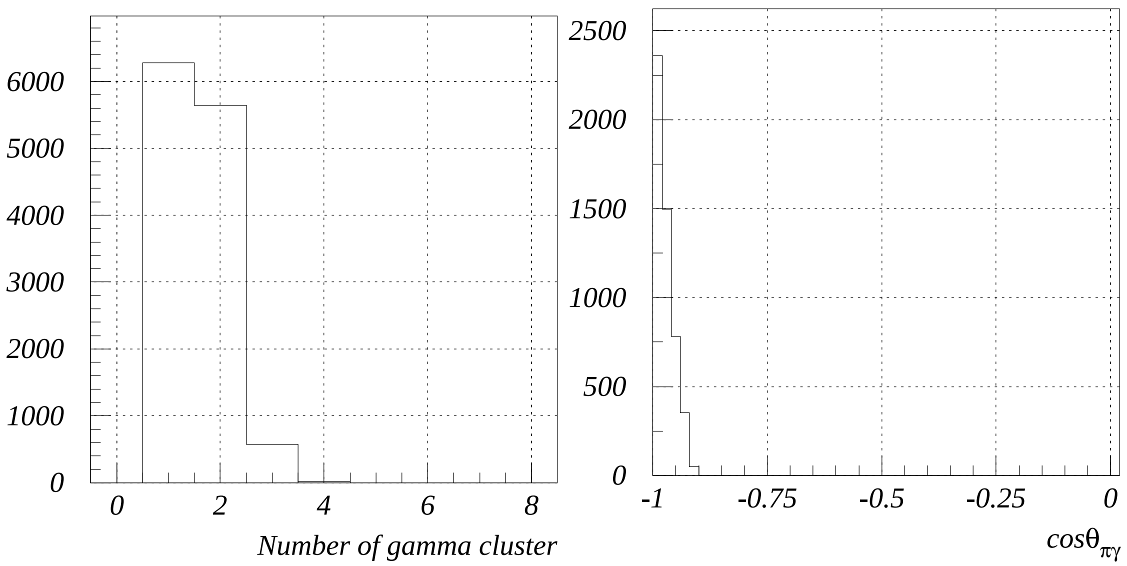

Figure 3.2: Distribution of the number of reconstructed photon clusters in the BVL and BV from the Monte-Carlo data (left); distribution of the cosine of the angle between π^+ and the higher-energy photon cluster (right). In both of these distributions, Monte-Carlo $K^+ \to \pi^+\gamma\gamma$ events whose π^+ momentum is greater than 200 MeV/c are generated.

3.2 Event Reconstruction

Event reconstruction consists of charged-track reconstruction and photon reconstruction. Fig. 3.3 shows event displays of a reconstructed $K_{\pi 2}$ event.

3.2.1 Charged-Track Reconstruction

A charged track is reconstructed in each of the Target, Drift Chamber and Range Stack. The results from these subsystems are integrated to obtain charged-track information: momentum, range and kinetic energy at the kaon decay vertex. The momentum, range and kinetic energy for the reconstructed $K_{\pi 2}$ and $K_{\mu 2}$ events are shown in Fig. 3.4, and those for Monte-Carlo events are shown in Fig. 3.5. Their means and sigmas are listed in Table3.1. The kinematic values of each Monte-Carlo event are smeared with random numbers so as to reproduce the distributions of real data.

Target Reconstruction

The charged-track reconstruction in the Target starts by assigning each fiber, based on information of both the energy and timing, to "kaon fibers", "charged-decay-product fibers" or "photon fibers" by using a likelihood technique. A charged track reconstructed by the Drift Chamber is extrapolated to the Target and assists the reconstruction. The fibers that have a large energy with a time around the incoming beam and clustered near the extrapolated Drift Chamber track are identified as kaon fibers. The fibers that have a small energy with a time consistent with the timing determined by the Range Stack hits, and are located on the extrapolated Drift Chamber track within a certain width (called "swath") are identified as charged-decay-product fibers. The times are averaged and the energies are summed up in order to obtain the time and energy of the kaon or charged decay product in the Target. The fibers that have a time consistent with the Range Stack time, but are located outside of the swath, are identified as photon fibers, which are thought to be due to photons from the kaon decay, or due to secondary incoming particles. The kaon decay vertex in the x-y plane is determined by using the information of the B4-counter hit position and the kaon fibers on the swath. The range of a charged track is then defined as the distance from the kaon decay vertex to the edge of the Target along the extrapolated Drift Chamber track. The Target has information only in the x-y plane, and the z position of the kaon decay vertex is determined by the extrapolated Drift Chamber track to the vertex. An event display in the Target view is shown in the bottom-left figure of Fig. 3.3.

Drift Chamber Reconstruction

In the Drift Chamber analysis, the momentum and the polar angle of the charged decay product are obtained. The charged-track reconstruction in the Drift Chamber is twofold: one is fits in the x-y plane; the other is fits in the r-z plane. The positions from the sense wire hits are fitted by a circle in the x-y plane. The cathode strip hits are fitted by a straight line in the r-z plane, and the polar angle of the charged decay product is obtained by this z fitting. After reconstruction in the Target is performed, fitting in

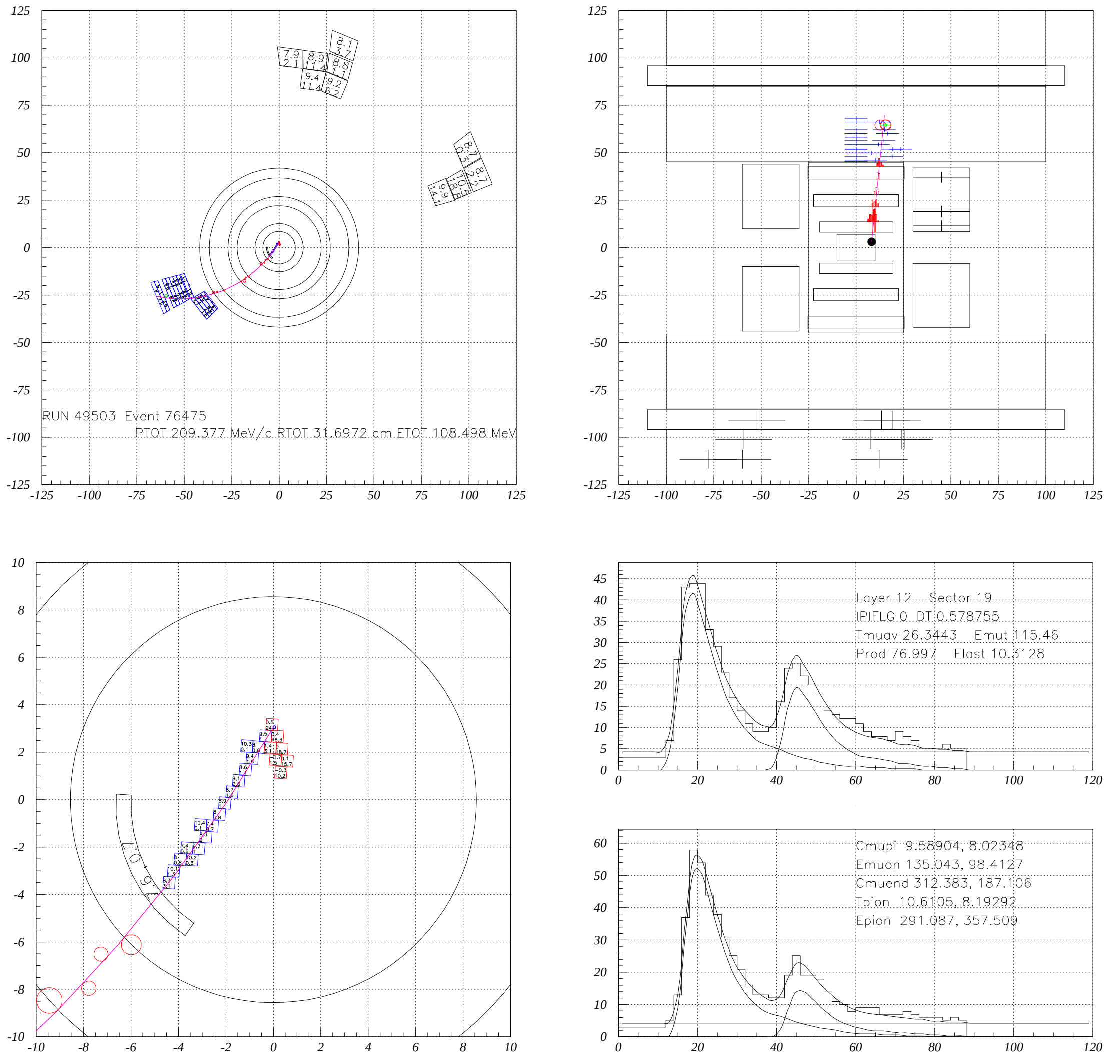

Figure 3.3: Event displays of a reconstructed $K_{\pi 2}$ event: x-y view (top-left), r-z view (top-right), the Target view (bottom-left) and the result of pulse shape analysis by the Transient Digitizer in the stopping counter (bottom-right).

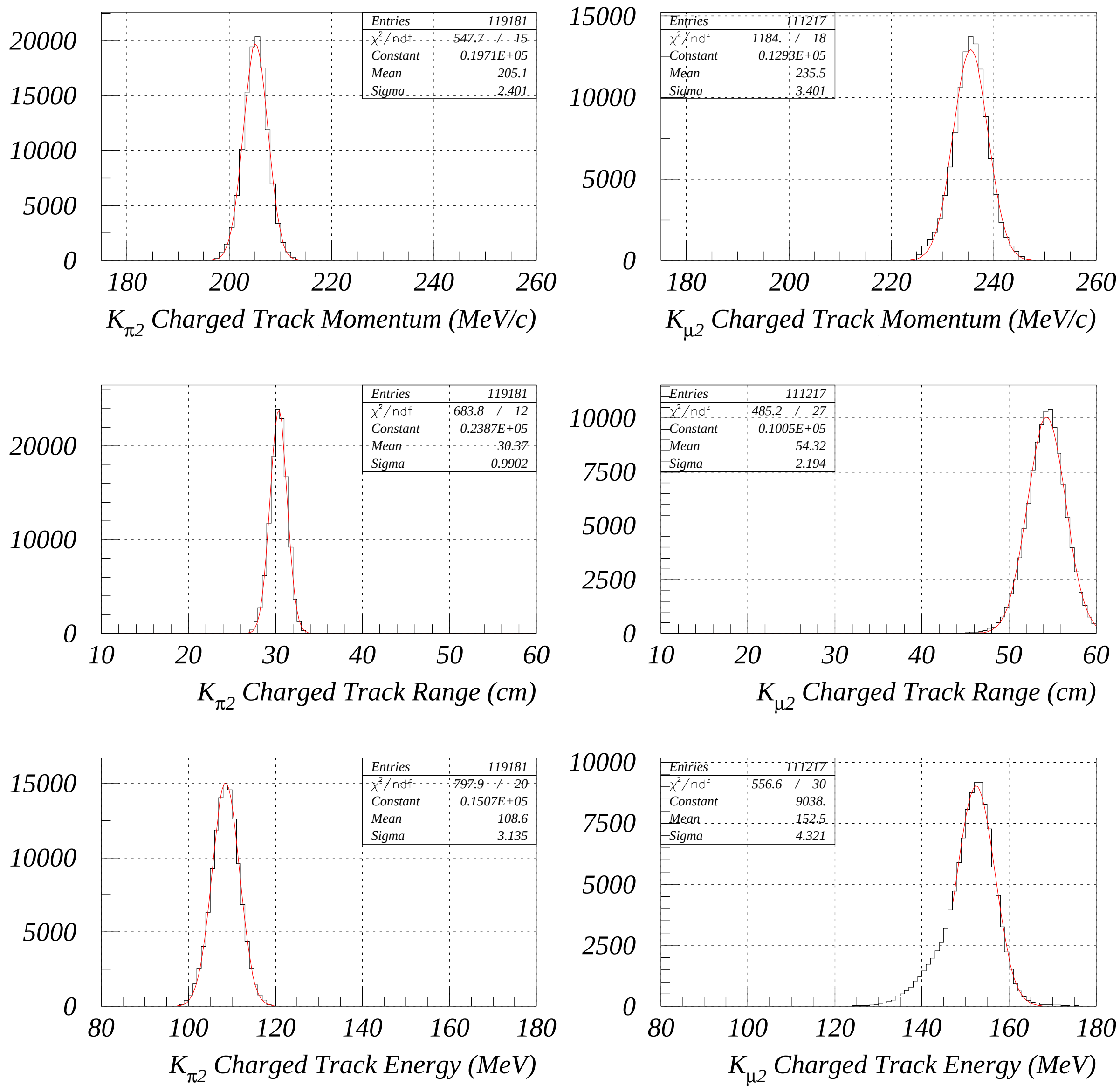

Figure 3.4: Charged track momentum (top), range (middle) and energy (bottom) for successfully reconstructed $K_{\pi 2}$ (left) and $K_{\mu 2}$ (right) events in the real data.

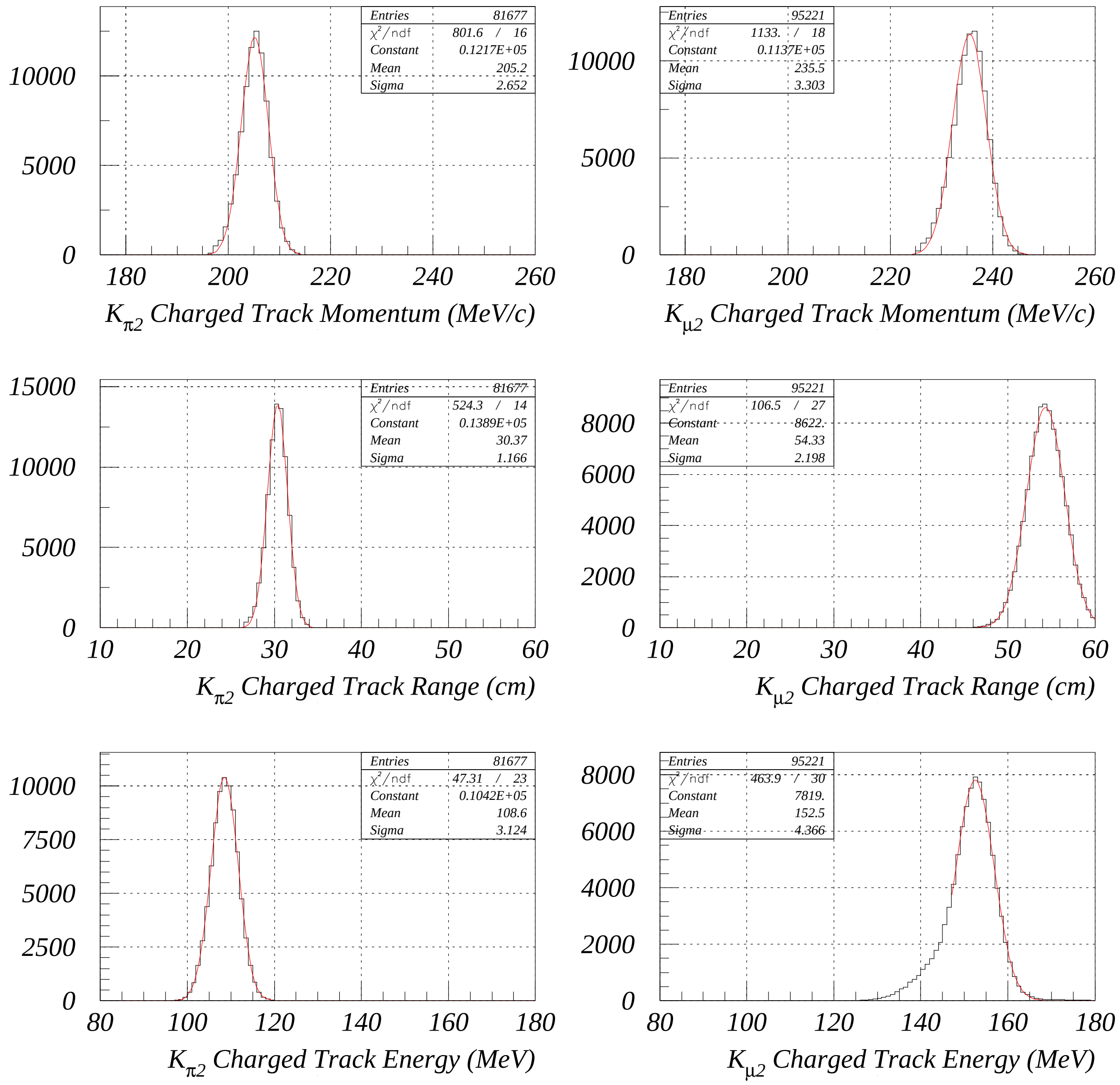

Figure 3.5: Charged track momentum (top), range (middle) and energy (bottom) for successfully reconstructed $K_{\pi 2}$ (left) and $K_{\mu 2}$ (right) events in the Monte-Carlo data.

the x-y plane is performed once again by taking into account the x-y positions of the reconstructed charged-decay-product fibers in the Target. The momentum in the Drift Chamber is obtained from the radius of the fitted circle, and is corrected by taking into account the ranges in the Target, the I-counter, and the inner and outer walls and gas of the Drift Chamber, in order to obtain the total momentum at the decay point.

Range Stack Reconstruction

Charged-track reconstruction in the Range Stack starts by looking for the $T \bullet 2$ sector, which has coincidence hits in the first and second inner-most layers in the same sector. Starting from the $T \bullet 2$ sector, the Range Stack counters in which a charged decay product passes through (Track Counters) are searched for as follows:

- First of all, a counter which is in the same sector and is one layer outside is examined.
- If there is no such hit, a counter that is in the same layer, but is located in an adjacent sector, in clockwise is examined.
- If there is no such hit, a counter which is in the adjacent sector in clockwise and one layer outside is examined.

If a hit counter is found, a search for the next counter is performed with the same procedure and is repeated until no more hit-counter is found. The last counter is defined as the "stopping counter" where the charged decay product comes to rest. This procedure is illustrated in Fig. 3.6. Note that, when a hit counter is found, the search procedure immediately proceeds to the next step; the double-hatched counter in the figure is therefore ignored and is not considered to be a track counter, even if it has an intime hit. The times of the track counters are averaged to obtain the Range Stack time. The energy and the range of the charged decay product are obtained by assuming that the track is a π^+. The energy in the Range Stack is calculated by summing up the energies in the track counters and subtracting the muon energy from the $\pi^+ \to \mu^+\nu$ decay at rest in the stopping counter. In order obtain get the total kinetic energy of the charged track, the energy in the Target, the energy in the I-counter and the expected energy loss in the Drift Chamber walls and gas are added to the Range Stack energy. In order to obtain the range of a charged track, a "track fitting" is performed. By assuming that the charged track is a π^+, the track is propagated in the Range Stack by losing energy based on the Bethe-Bloch formula and by bending in the magnetic field. The propagations are repeated until the track matches the point where the sector is changed (sector crossing), the RSSC hit positions and the energy in the stopping counter, by varying the momentum and the incident angle at the inner-most radius of the Range Stack. The range in the Range Stack is calculated from the path length of the fitted track. In order to obtain the total range of the charged track, the range in the Target, the range in the I-counter and range in the dead material are added to the range in the Range Stack.

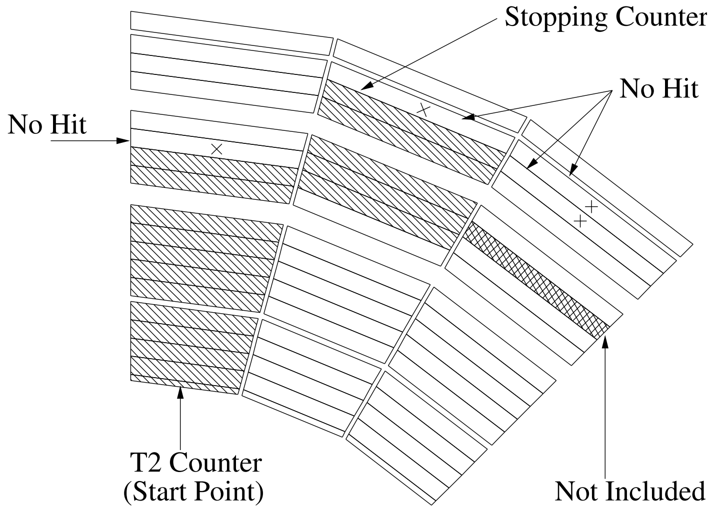

Figure 3.6: Illustration of track reconstruction in Range Stack. The hatched counters are those where a charged decay product has passed through. The counters marked by a cross and a counter with double-hatched counter in this figure are not included to the track counters.

		$K^+ \to \pi^+\pi^0$		$K^+ \to \mu^+\nu_\mu$	
		Peak	σ	Peak	σ
Charged Track Momentum (MeV/c)	Real Data	205.13	2.40	235.52	3.40
	Monte Carlo	205.18	2.65	235.51	3.30
	True Value	205.14	-	235.53	-
Charged Track Range (cm)	Real Data	30.37	0.99	54.32	2.19
	Monte Carlo	30.37	1.17	54.33	2.20
	True Value	30.37	-	54.34	-
Charged Track Energy (MeV)	Real Data	108.59	3.14	152.46	4.32
	Monte Carlo	108.57	3.12	152.48	4.37
	True Value	108.55	-	152.48	-

Table 3.1: Means and sigmas of the charged track momentum, range and energy distributions for successfully reconstructed $K_{\pi 2}$ and $K_{\mu 2}$ events. Values from the Monte-Carlo events and of true values are also listed.

3.2.2 Photon Reconstruction

A photon shower in the Barrel Veto Liner and Barrel Veto is reconstructed by grouping those modules whose timing is close to the Range Stack time. As illustrated in Fig. 3.7, only the adjacent modules are grouped and considered as a single photon cluster. Once a cluster is reconstructed, offline information on the cluster, such as the time and energy, is obtained. The photon-cluster time is calculated by averaging the time of each module in the cluster. As mentioned in section 2.6.1, the Barrel Veto Liner and Barrel Veto are a sampling calorimeter; the energy recorded in each module (visible energy) is not equal to, but should be proportional to, the photon energy deposited in the module. In order to obtain the real photon energy, one needs to divide the visible energy by a correction parameter, named the "visible fraction". The visible fraction for Barrel Veto Liner and Barrel Veto might be different because the Barrel Veto Liner was just recently installed to E949, while the Barrel Veto have been working in the detector since 1988. In the calibration, the visible fraction for the Barrel Veto is obtained with the clusters whose shower is contained exclusively in the Barrel Veto. The energy sum of the two photons from π^0, which is monochromatic (245.6 MeV) in $K_{\pi 2}$ decay, is used as a calibration source. The visible fraction for the Barrel Veto Liner is then obtained by clustering a photon shared in both the Barrel Veto and Barrel Veto Liner. The energy sum of the two photons from π^0 in the $K_{\pi 2}$ events is compared with the expected value. The visible fractions for the Barrel Veto and the Barrel Veto Liner are listed in the Table3.2. Fig. 3.8 shows the distribution of the energy sum of the two photons from π^0 in $K_{\pi 2}$ events. The achieved mean and sigma after calibration are also given in Table3.2.

The positions of the photon cluster are also calculated. The x-y positions are obtained by taking the energy-weighted mean of the center positions of those modules that form the cluster. In calculating the z position for each module, the following empirical formula is used [29]:

$$z_{com} = \frac{z_{tdc} + z_{adc} \times \sqrt{E/10}}{1 + \sqrt{E/10}},$$

where E is the measured energy in MeV in the module, $z_{tdc} \equiv \frac{c}{2}(t_1 - t_2)$, and $z_{adc} \equiv \frac{\lambda}{2} \log \frac{a_2}{a_1}$. Here, t_1 and t_2 are the TDC values for upstream and downstream of the module, respectively, and a_1 and a_2 are the ADC values for upstream and downstream of the module, respectively. c is a speed of light in the modules and λ is the attenuation length in each module. The z positions of the modules in the cluster are averaged to obtain the cluster z position.

	Peak (MeV)	σ	vsfr BV	vsfr BVL
Real Dara	245.56	34.70	0.2954	0.3101
Monte Carlo	245.58	34.79	0.2895	0.2734

Table 3.2: Means and sigmas for the energy sum of the two reconstructed photons in Barrel Veto Liner and Barrel Veto from the π^0 of $K_{\pi 2}$ events. The visible fractions for Barrel Veto and Barrel Veto Liner are also listed in the 4th and 5th columns, respectively. The calibrations for read data and Monte-Carlo data have been performed separately.

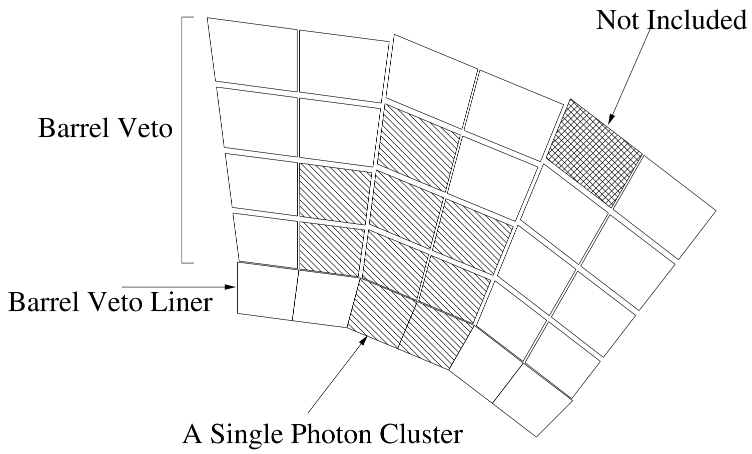

Figure 3.7: Illustration of photon reconstruction in the Barrel Veto Liner and Barrel Veto. The double hatched module is not included in the photon cluster and is regarded as an isolated photon.

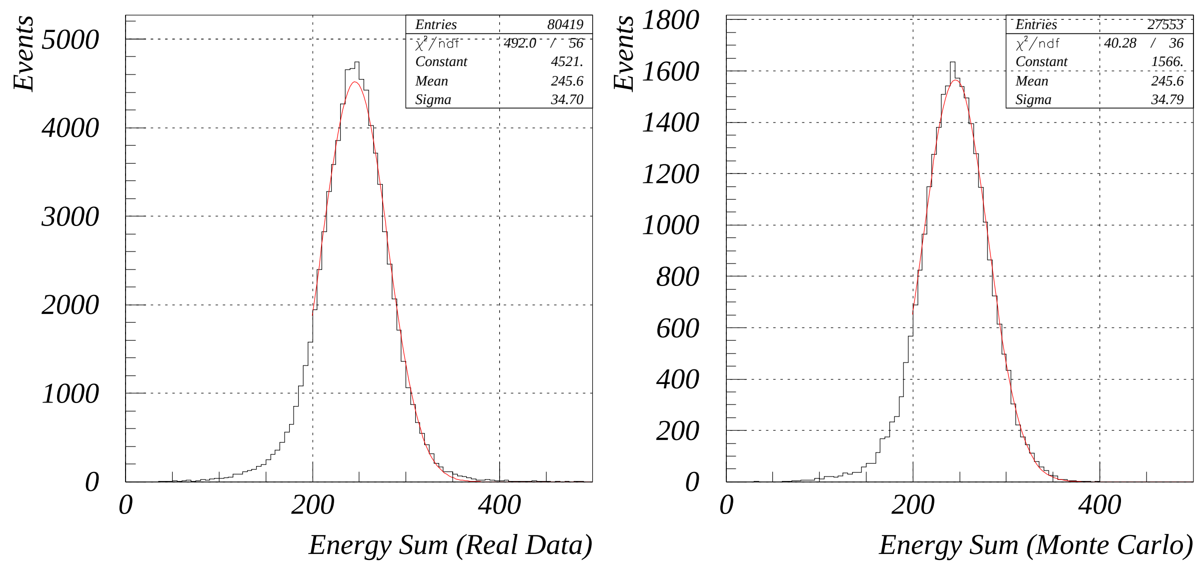

Figure 3.8: Energy sum of the two reconstructed photons in the Barrel Veto Liner and the Barrel Veto from the π^0 of $K_{\pi 2}$ events in the real data (left) and Monte-Carlo data (right) after correction with the visible fractions.

3.3 Background Categorization

Fig. 3.9 shows a scatter plot of the momentum and range of the charged tracks from successfully reconstructed events in the $K^+ \to \pi^+\gamma\gamma$ triggers. The search region is indicated by the box in the figure. As can be seen, the region is contaminated by backgrounds from the other K^+ decays and the beam particles. Background studies are performed by categorizing each background source as follows.

3.3.1 Backgrounds due to Kaon Decays

$K_{\pi2}$ Background

$K_{\pi2}$ decay is the major background source because the final state is identical to $K^+ \to \pi^+\gamma\gamma$. The kinematic tail of the $K_{\pi2}$ peak (events clustered at P=205 MeV/c and R=30 cm in the figure) could sneak into the search region due to the limited detector resolution. Cuts on charged track kinematics effectively remove this background. The relation between the energy ratio and the opening angle of the two photons also discriminates the signal from background because of the different kinematics of photons in the $K^+ \to \pi^+\gamma\gamma$ and $K_{\pi2}$ decays. If two photons from the $K_{\pi2}$ decay hit the same modules in the Barrel Veto Liner and the Barrel Veto, they could be reconstructed as a single-photon cluster, and would be a background. This background is illustrated in Fig. 3.10. In this case, the maximum discrepancy among the z-measurements in the cluster discriminates the signal from background. These cuts are explained in detail in section 4.1.

Overlapping Photon Background

Another background source from $K_{\pi2}$ decay is called "Overlapping photon background". The opening angle of two photons from $K^+ \to \pi^+\gamma\gamma$ is small for events whose π^+ momentum is near the kinematic end point (227 MeV/c), as can be seen in the right-hand figure of Fig3.1. These photons could be detected as a single cluster in the Barrel Veto Liner and the Barrel Veto. On the other hand, the higher energy photon from the π^0 in $K_{\pi2}$ decays tends to be emitted in the opposite direction to the π^+, and a shower due to the lower energy photon could be overlapped with the π^+ track in the Range Stack. This process causes a background because a single photon cluster in the final state is accepted as a signal event, as mentioned in section 3.1. In this case, the kinetic energy of the charged track is overestimated due to the presence of the energy of the overlapped photon, but the momentum and range should still be consistent with those from $K_{\pi2}$. Cuts on the charged track are therefore effective to this background source. Cuts on the dE/dx in the Range Stack are also effective to reject this background, because dE/dx in the counters with overlapped photons would be different from that expected from π^+. Fig. 3.11 illustrates the overlapping photon background.

Muon Background

The kaon decays with a muon and a photon (or photons) in the final state, such as the $K^+ \to \mu\nu\gamma$ ($K_{\mu2\gamma}$) and $K^+ \to \pi^0\mu\nu$ ($K_{\mu3}$) decays, could be a source of background if the muon is mis-identified as a π^+. $K_{\pi 2}$ decay whose π^+ decays in flight in the detector is also categorized in this analysis as muon background. Particle identification using Transient Digitizer data is the most powerful tool to remove the muon background. However, there are three background processes in the case of mis-identifying the muon as a π^+ in the shape analysis of a pulse recorded in the stopping counter:

- Fluctuation of the pulse mimicked the double pulses due to $\pi^+ \to \mu^+$ by itself (tail fluctuation).
- An accidental hit mimicked the muon signal in the $\pi^+ \to \mu^+$ decay chain (muon time accidental).
- An accidental hit mimicked the electron signal in the $\pi^+ \to \mu^+ \to e^+$ decay chain (electron time accidental).

Fig. 3.12 illustrates these processes together with the true signal process. In Fig. 3.9, the range-momentum relation discriminates pions from muons ("pion band" and "muon band" in the figure); cuts on the charged track kinematics are also useful.

3.3.2 Backgrounds due to Beam Particles

Single Beam Background

There are backgrounds due to the incident beam particles. The kaon decay-in-flight to $\pi^+\pi^0$ is a source of background from a kaon because a π^+ from the $K_{\pi 2}$ decay-in-flight in the beam before coming to rest could be Lorentz-boosted and satisfy the kinematics of $K^+ \to \pi^+\gamma\gamma$. This background is called "single beam background"; the mechanism is illustrated in Fig. 3.13. The delayed coincidence confirms that K^+ comes to rest in the Target and suppresses this background. Also, particle detection in the Cerenkov counter at the Range Stack time is an effective tool against this background.

Double Beam Background

After suppressing the single beam background, there is another type of background from the incident beam particles. This background is called "double beam background", its mechanisms are illustrated in Fig. 3.14. There are two types of double-beam background:

- A primary kaon enters the target; a secondary kaon follows and decays in flight to $\pi^+\pi^0$, and a π^+ enters and comes to rest in the Range Stack.
- A primary kaon enters the target and decays to $\pi^+\pi^0$ at rest; a secondary pion follows and is scattered into the Range Stack.

The double-beam background can not be removed by delayed coincidence because the kaon time and the pion time in the Target come from different particles. This background is rejected by looking for any extra activity in the beam instruments at the time when a charged track enters the Range Stack. Target pattern-recognition cuts also help to suppress the background.

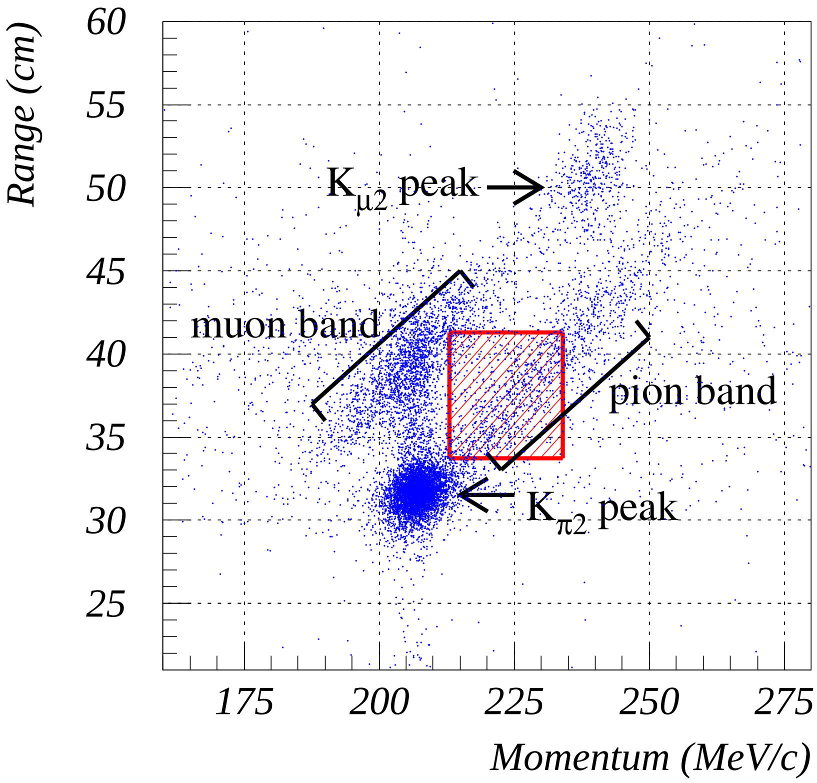

Figure 3.9: Scatter plot of the range and momentum of charged tracks from successfully reconstructed events in the $K^+ \to \pi^+\gamma\gamma$ triggers.

In summary, there are five background sources: three from kaon decays and two from incident beam particles. The backgrounds are tabulated in Table 3.3 together with the effective cuts that are used in background studies.

	Kinematics	Photon	Particle ID	Timing
$K^+ \to \pi^+\pi^0$	$\surd$	$\surd$		
Overlapping Photon	$\surd$		$\surd$	
Muon	$\surd$		$\surd$	
Single Beam			$\surd$	$\surd$
Double Beam				$\surd\surd$

Table 3.3: Categorization of background sources. The cuts for background studies are also listed.

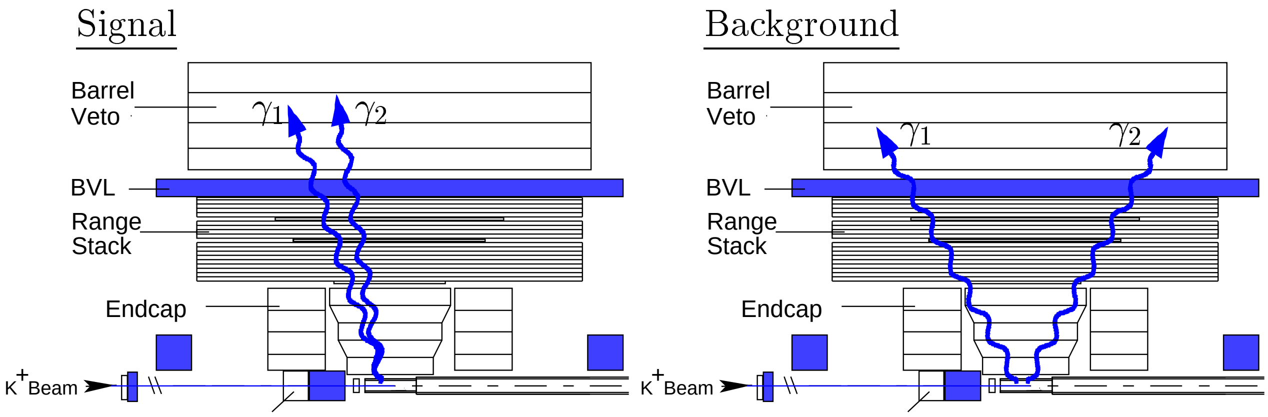

Figure 3.10: Illustration of the $K_{\pi2}$ background.

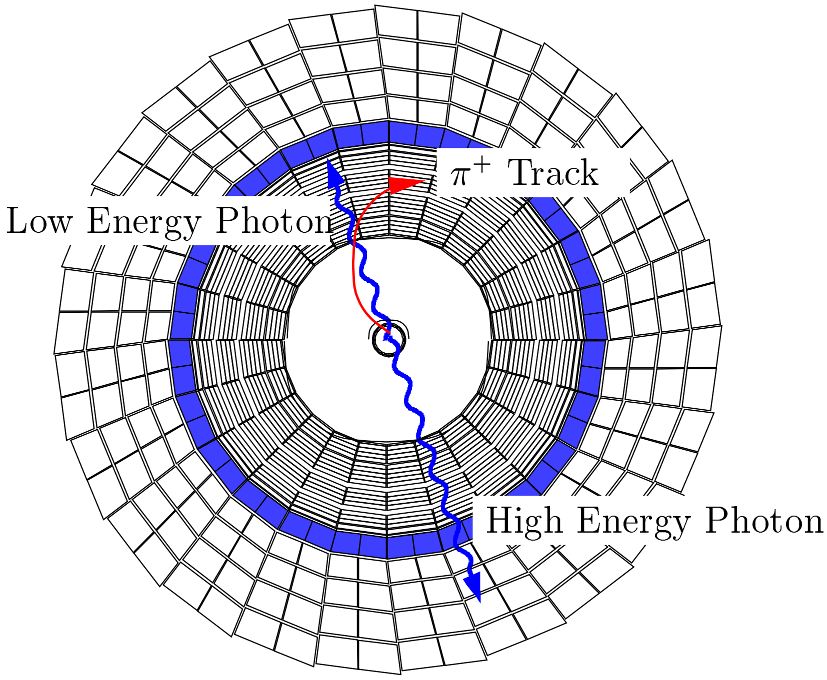

Figure 3.11: Illustration of the overlapping photon background.

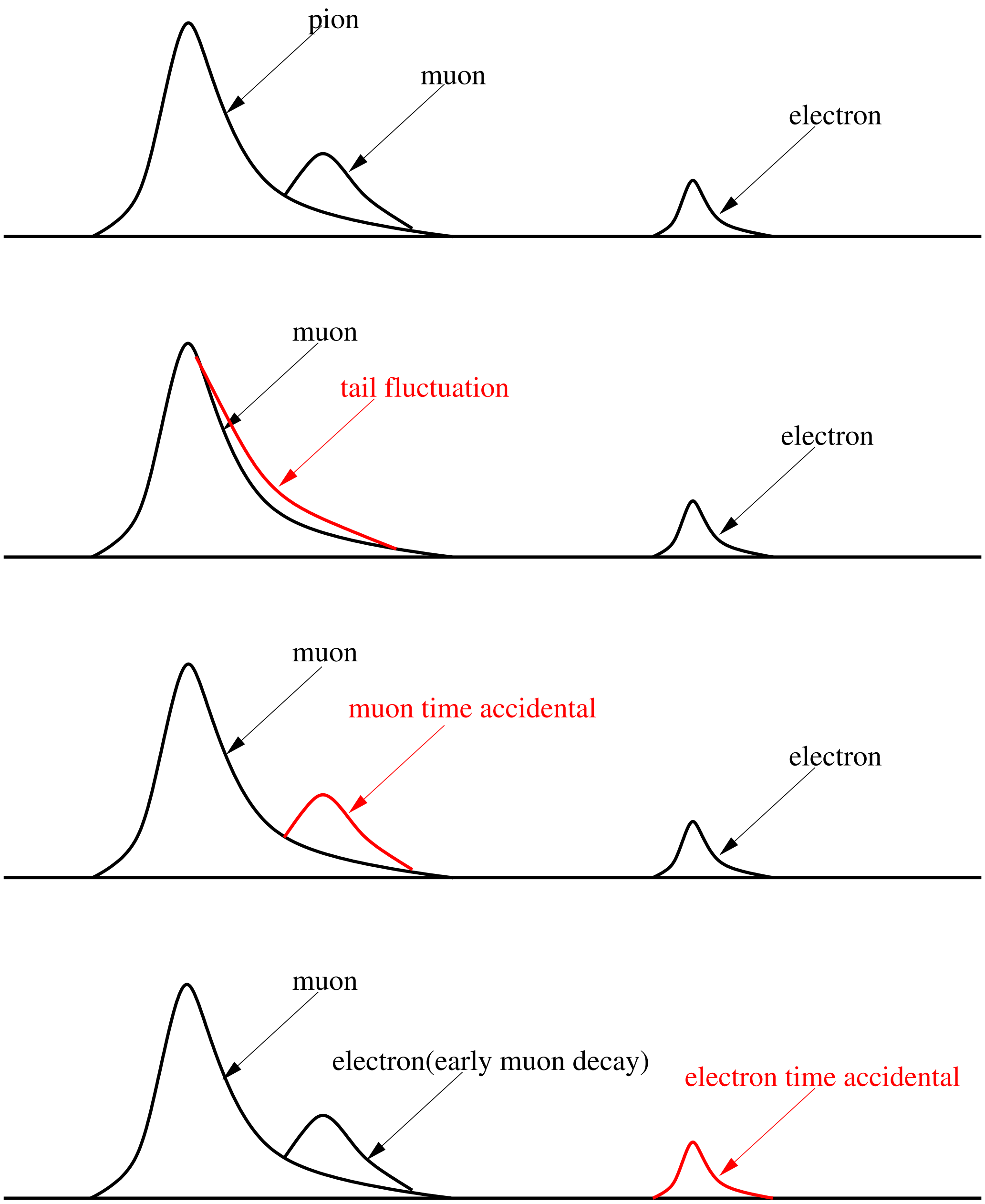

Figure 3.12: Scenarios of π^+ mis-identification in the stopping counter.

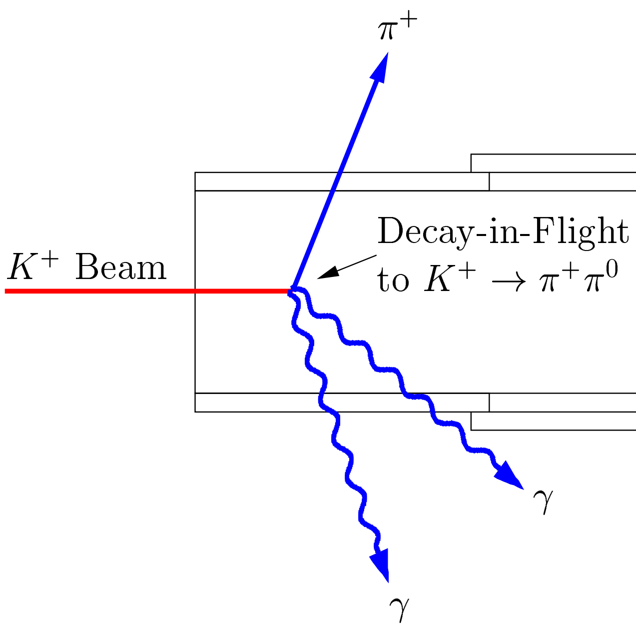

Figure 3.13: Illustration of the single-beam background.

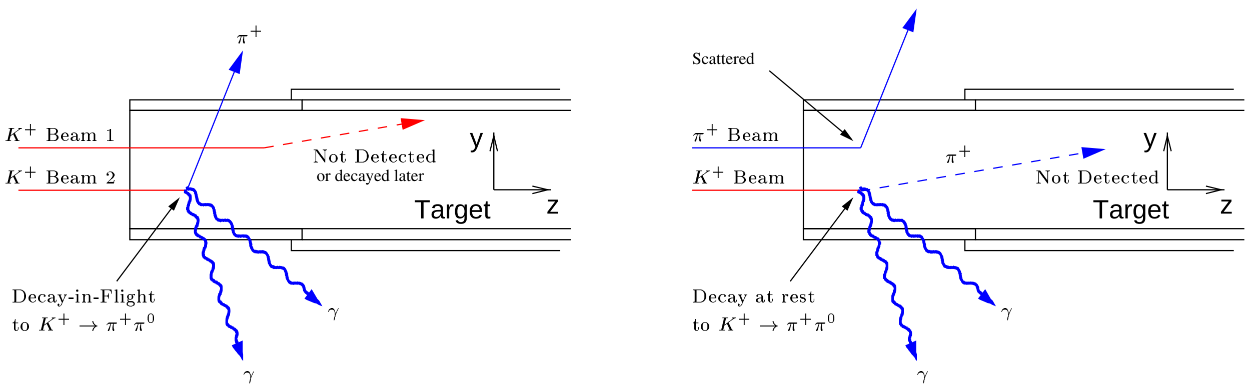

Figure 3.14: Illustrations of the double-beam background.

3.4 Analysis Method

3.4.1 Bifurcation Method

After categorizing each background source, as discussed in the previous section, each background level is estimated by using the "Bifurcation Method" developed by the E787 and E949 experiments. The concept of the method is illustrated in Fig. 3.15. The first step of background estimation is to select two "uncorrelated" Cuts (cut1 and cut2 in the figure), both of which have large rejection against a targeting background. In the top figure of Fig. 3.15, the tightness of cut1 and cut2 are represented in the vertical and horizontal axes, and the lower-left corner is the tightest point by these two cuts. The data sample is divided into four regions (labeled A, B, C and D in the figure) by each cut position, and region A is defined as the search region. If cut1 and cut2 are totally uncorrelated, the ratio of the numbers of events in region A to B should be the same as that of C to D. The background level in the search region is therefore expressed as

$$A = B \times \frac{C}{D}. \tag{3.1}$$

One policy used in the E949 analysis is to avoid examining the search region during background studies; we have to develop a method to estimate the background level without looking at the search region. In the Bifurcation Analysis, the sample is divided into two branches, called the "Normalization Branch" and the "Rejection Branch".

- Normalization Branch:
  The normalization branch in the bifurcated method is illustrated by the middle figure of Fig. 3.15. The events that are tagged by inverting cut1 are used in the normalization branch (shaded part of the middle-left figure). Then, cut2 is applied to the events and the number of events that remain are counted. In this figure, B is the number of events in the normalization branch.

- Rejection Branch:
  The rejection branch in the bifurcated method is illustrated in the bottom figure of Fig. 3.15. The events that are tagged by inverting cut2 are used in the rejection branch; cut1 is applied to the events, and the rejection factor R of cut1 is obtained as

$$R = \frac{C + D}{C}.$$

By using the above numbers and Eqn. 3.1 the background level in the search region (N_{BG}) is estimated to be [2]

$$N_{BG} = \frac{B}{R - 1}. \tag{3.2}$$

By using the Bifurcated Method, we can enhance the backgrounds in the read data, prevent signal events from being examined, and estimate the background levels below one event. The bifurcation method for the case of the $K_{\pi 2}$ background is shown in Fig. 3.16

[2] More precisely speaking, the "-1" in Eqn.3.2 comes from the "tagging efficiency" ϵ, which is expressed as $\epsilon = 1 - 1/R$ in the normalization branch. The background level is estimated to be $N_{BG} = N/\epsilon \times 1/R = N/(R-1)$ and is identical to Eqn.3.2.

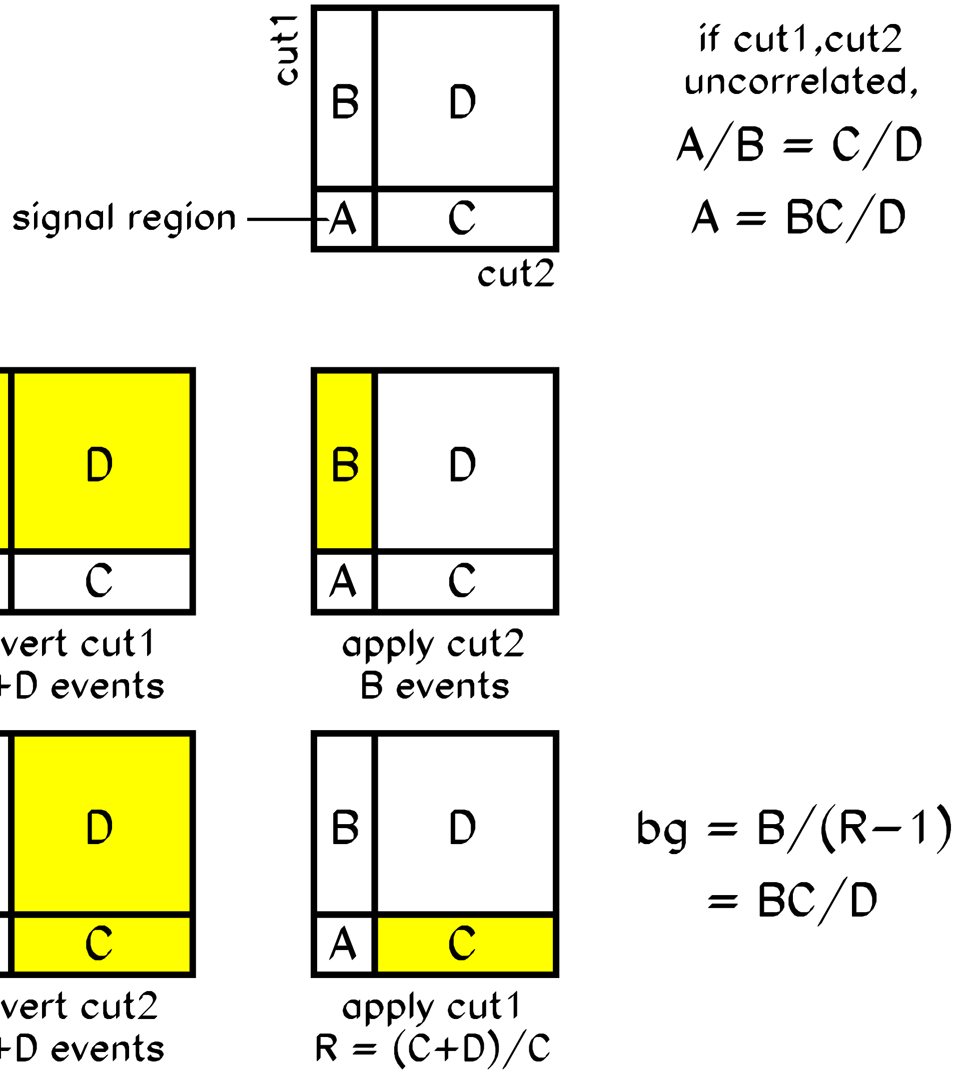

Figure 3.15: Illustration of the bifurcation method.

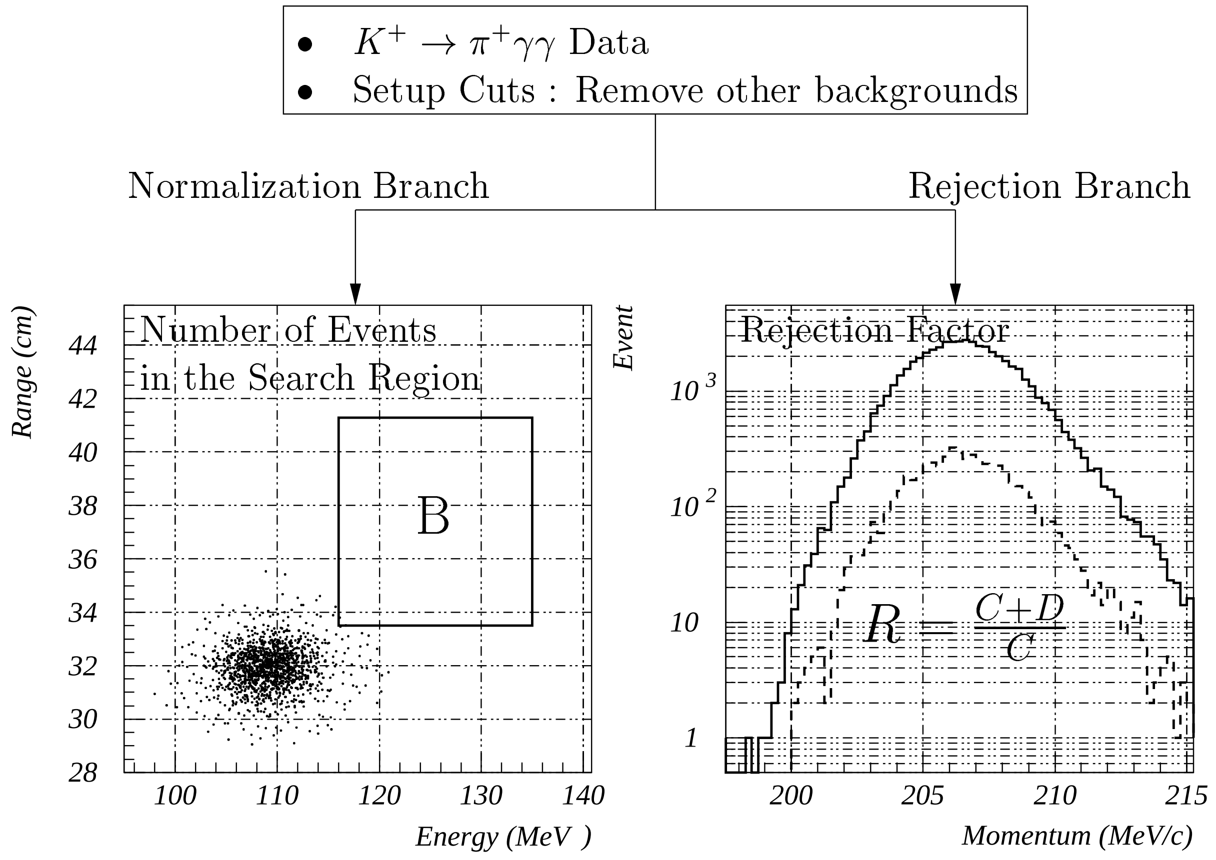

Figure 3.16: Example of the bifurcation method for a $K_{\pi 2}$ background study.

as an example. At first, in order to remove backgrounds other than $K_{\pi 2}$, "Setup Cuts" are imposed to the $K^+ \to \pi^+\gamma\gamma$ data. Note that basic reconstruction cuts, such as the fiducial cuts on the charged track and photons, are also included in the Setup Cuts. The two cuts for the bifurcated method are cuts on the charged-track kinematics and cuts on photons, as explained in the previous section. In the normalization branch (left part of the figure), the events that failed one of the photon cuts are tagged and the kinematic distributions of π^+ from the $K_{\pi 2}$ backgrounds are provided. The number of events B which survived the $K^+ \to \pi^+\gamma\gamma$ kinematic cuts are counted. In the rejection branch (right part of the figure), the events that satisfy the $K_{\pi 2}$ kinematic cuts (momentum, range and energy consistent with $K_{\pi 2}$) are tagged. The rejection factor (R) of photon cuts are then measured by taking the ratio of the numbers of events before and after imposing photon cuts (solid and dashed lines in the figure, respectively). The $K_{\pi 2}$ background level is finally obtained by using Eqn. 3.2.

3.4.2 Correlation Check

The Bifurcation Method is based on the assumption that the two bifurcated cuts are uncorrelated; otherwise, the background estimation would be screwed up. Checks of the possible correlation between two bifurcated cuts are therefore important. Fig. 3.17 illustrates the concept of a correlation check. In the bifurcation method, cut1 and cut2 are simultaneously loosened by factors of M and N, respectively. We should be able to observe

$$N'_{BG} = \frac{BC}{D}(M \times N - 1)$$

in the outside-the-box region (labeled by A'). Note that the estimated background level to the search region (BC/D) should have been subtracted, because we always masked out the search region during a correlation check. The loosening factors are obtained from the background probability functions that characterize the distribution of each background. The construction of the background probability function is shown in Fig. 3.18 for the case of the $K_{\pi2}$ background as an example. The top figure of Fig. 3.18 is the normalization branch of the $K_{\pi2}$ background study. The thick line shows the standard cut position of the $K^+ \to \pi^+\gamma\gamma$ kinematic cut, and thin lines are the loosened and tightened cut-positions. The background level and the acceptance are re-measured at each cut position. The bottom figure of Fig. 3.18 presents the background probability function for the $K_{\pi2}$ background. Each point is normalized by the background level and the acceptance at the standard cut position.

If there is a candidate event in the search region, we perform a likelihood analysis.

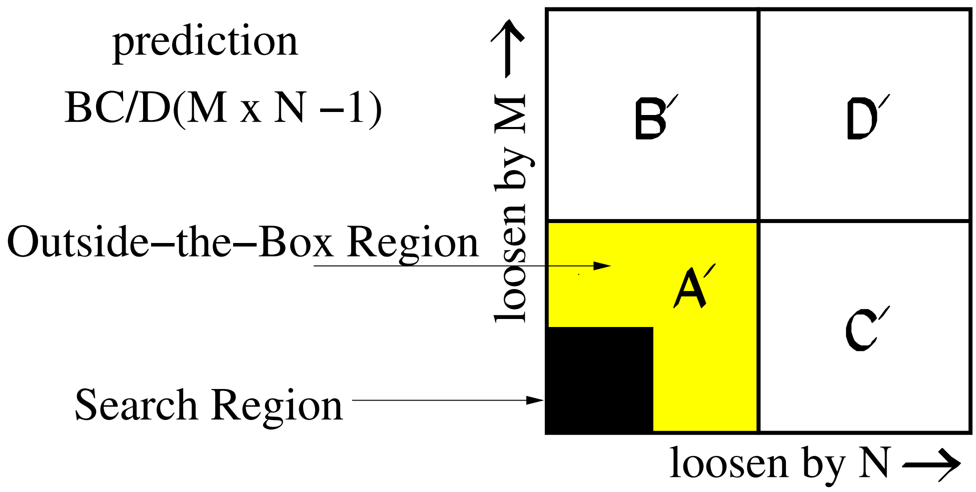

Figure 3.17: Illustration of a correlation check between two bifurcation cuts.

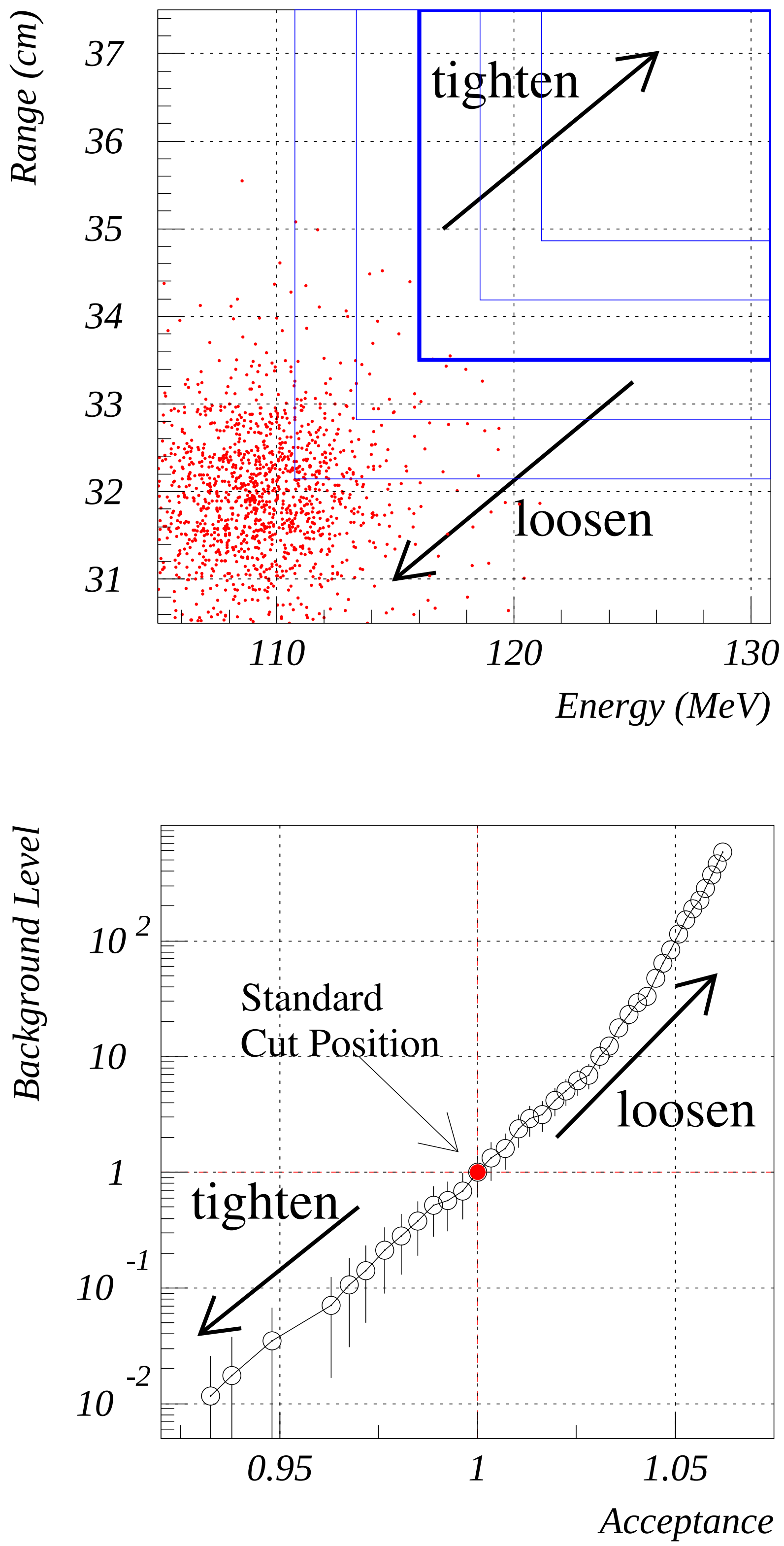

Figure 3.18: Example of the constriction of the background probability function for the $K_{\pi 2}$ background.

Chapter 4

Background Studies

Discussions in this chapter are concentrated on estimations of background levels derived from sources, such as $K_{\pi 2}$, overlapping photon, muon, single beam and double beam backgrounds. Each section starts with a subsection that explains the "two cuts" for the bifurcation method; the background level is estimated in the next, and a possible correlation between two bifurcated cuts is checked at the end.

The background samples used in these studies are selected from the $K^+ \to \pi^+\gamma\gamma$ trigger events (real data), for the normalization branch and for the rejection branch in the bifurcation method, by reversing some of the "two cuts". We point out that the samples used in determining the cut positions (selected from the "1/3 portion" of the real data) and the samples in estimating the background level (selected from the "2/3 portion" of the real data) are different and independent. The sample for a cut determination is selected by picking up one third of the whole $K^+ \to \pi^+\gamma\gamma$ data uniformly; the cuts are studied and frozen with the one-third sample. The remaining (and independent) two-thirds sample is used to estimate the background level, and a factor of 1.5 is multiplied in order to obtain the background level to the full sample. Since the cuts have been designed and tuned up by looking at and minimizing the background level to the one-third sample, it should be safer and less biased to perform an "unbiased" background estimation by imposing pre-determined cuts from the one-third sample to the independent two-third sample.

4.1 $K_{\pi 2}$ Background

4.1.1 $K_{\pi 2}$ Cuts

The two bifurcation cuts for the $K_{\pi 2}$ background estimation are:

- cuts on the charged-track kinematics, and
- cuts on the photon cluster in the Barrel Veto and the Barrel Veto Liner,

each of which is described below.

Kinematic Cuts

The $K_{\pi 2}$ decay is a two-body decay, which is removed by cuts on the charged track kinematics: momentum, range and kinetic energy of π^+. Fig. 4.1 shows the distributions of the momentum, range and kinetic energy for the $K^+ \to \pi^+\gamma\gamma$ Monte-Carlo events and the real $K_{\pi 2}$ events in the background sample. The cut positions, indicated by the arrows in each distribution, are set to be

$$\begin{array}{ccccc} 213.3 \text{ MeV/c} & < & \text{Momentum} & < & 234.0 \text{ MeV/c}, \\ 33.5 \text{ cm} & < & \text{Range} & < & 41.3 \text{ cm}, \\ 116.0 \text{ MeV} & < & \text{Energy} & < & 135.0 \text{ MeV}. \end{array}$$

Note that the cuts on the upper side are also useful to remove the muon background.

Photon Cuts

When one photon from $K_{\pi 2}$ is detected in the Barrel Veto Liner and the Barrel Veto, the other photon might be detected in the other detector subsystem. The photon veto cuts on the other detector subsystems, therefore, remove the background. The time window and energy threshold are set to each subsystem, and are listed in the Appendix A.3.

If two reconstructed photon-clusters are found in the Barrel Veto Liner and the Barrel Veto, the ratio of the photon energies ($E_{\gamma 2}/E_{\gamma 1}$) and the cosine of the opening angle of two photons ($\cos\theta_{\gamma\gamma}$) are effective to discriminate the signal from the background. Here, the higher energy photon is designated as γ_1, and the other photon as γ_2. The relation between $E_{\gamma_1}/E_{\gamma_2}$ and $\cos\theta_{\gamma\gamma}$ is expressed as

$$\frac{E_{\gamma 2}}{E_{\gamma 1}} = \frac{E_0 - \sqrt{E_0^2 - \frac{2M_{\gamma\gamma}^2}{1-\cos\theta_{\gamma\gamma}}}}{E_0 + \sqrt{E_0^2 - \frac{2M_{\gamma\gamma}^2}{1-\cos\theta_{\gamma\gamma}}}},$$

where

$$E_0 \equiv \frac{M_{K^+}^2 - M_{\pi^+}^2 + M_{\gamma\gamma}^2}{2M_{K^+}}.$$

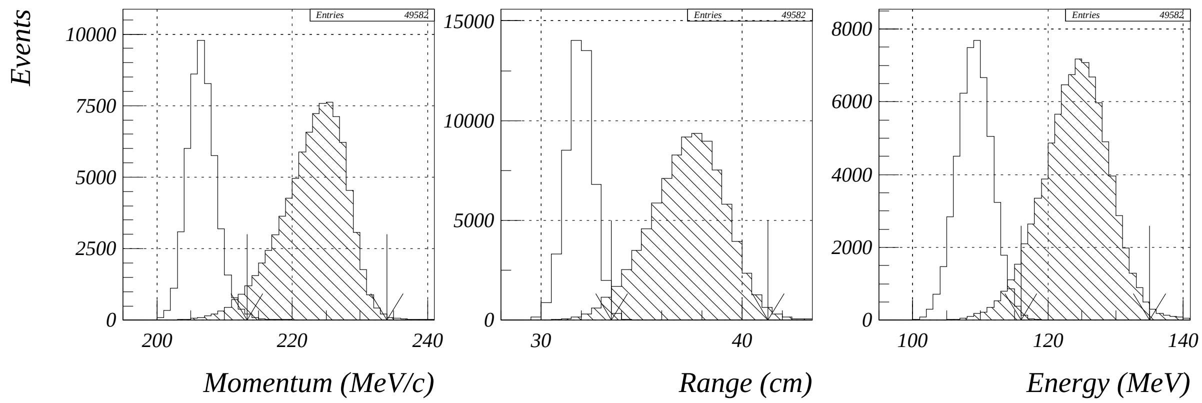

Figure 4.1: Momentum (left), range (middle) and kinetic energy (right) of the charged track for the $K^+ \to \pi^+\gamma\gamma$ Monte-Carlo events (shaded) and the real $K_{\pi 2}$ events in the background sample (opened). The cut positions are indicated by the arrows in each figure.

$M_{\gamma\gamma}$ is the invariant mass of the two photons, and M_{K^+} and M_{π^+} are the mass of K^+ and π^+, respectively. Fig. 4.2 shows scatter plots of $E_{\gamma_1}/E_{\gamma_2}$ and $\cos\theta_{\gamma\gamma}$ for the $K^+ \to \pi^+\gamma\gamma$ Monte-Carlo events and the real $K_{\pi 2}$ events in the background sample. The cut position, indicated by a curve in each plot, is set to be

$$M_{\gamma\gamma} \leq 100\mathrm{MeV/c^2}.$$

If two photons from π^0 of the $K_{\pi 2}$ decay hit the same or adjacent Barrel modules, they form a single photon cluster in the offline reconstruction. The two photons should have hit at different z positions because the opening angle of the two photons from π^0 in $K_{\pi 2}$ decay should be large. If only one reconstructed photon cluster is found in the Barrel Veto Liner and the Barrel Veto, a cut on the maximum discrepancy among z measurements[1] (z_{disc}) of the photon cluster removes such background events. The distributions of z_{disc} are shown in Fig. 4.3 for the $K^+ \to \pi^+\gamma\gamma$ Monte-Carlo events and the real $K_{\pi 2}$ events in the background sample. The cut position is set to be

$$z_{disc} < 112.5\mathrm{cm},$$

and is indicated by the arrow in the figure. The events that remain in the right figure of Fig. 4.3 after the z_{disc} cut are such a background that one photon from $K_{\pi 2}$ is detected in the Barrel Veto Liner and the Barrel Veto, and the other photon goes undetected due to the photon inefficiency of the E949 detector. We mention that the photon veto cuts on the other detector subsystems are already imposed on the sample.

[1]The z position is calculated for each module which forms the photon cluster.

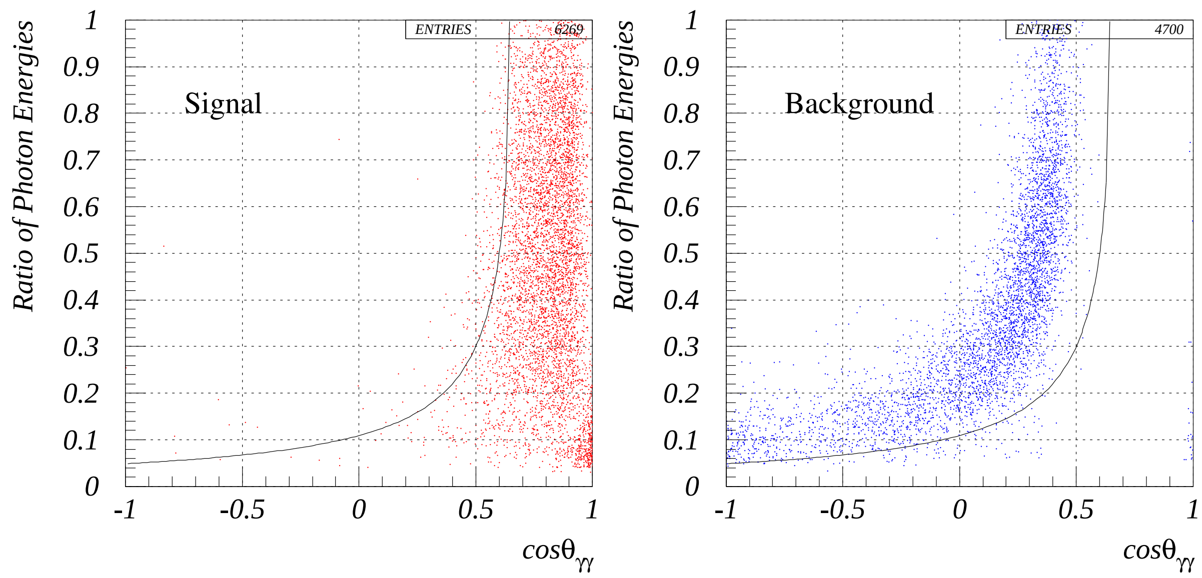

Figure 4.2: Scatter plot of the ratio of the photon energies (vertical axis) and the cosine of the opening angle between two photons (horizontal axis) for the $K^+ \to \pi^+\gamma\gamma$ Monte-Carlo events (left) and the real $K_{\pi 2}$ events in the background sample (right).

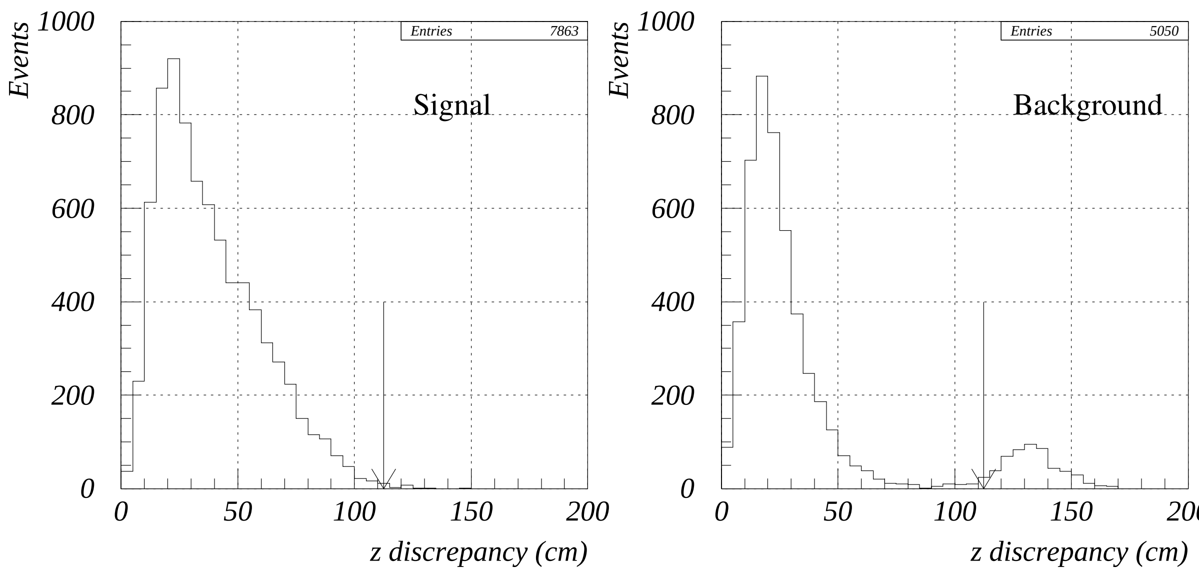

Figure 4.3: Distributions of the maximum discrepancy among z measurements in the photon clusters for the $K^+ \to \pi^+\gamma\gamma$ Monte-Carlo events (left) and the real $K_{\pi 2}$ events in the background sample (right).

4.1.2 $K_{\pi 2}$ Background Estimation

Backgrounds in the kinematic tail are studied in the normalization branch, in which the events that failed any one of the Photon Cuts are tagged. The kinematic tail of $K_{\pi 2}$ should be identical for one-cluster events and two-cluster events. Range-energy plots of the events in the normalization branch, after the Photon Cuts reversed and after the $K^+ \to \pi^+\gamma\gamma$ momentum cut, are shown in the left figure of Fig. 4.4. No event was left within the range and energy cuts. Instead of setting an upper limit, the normalization branch is further bifurcated (2nd bifurcation), based on the assumption that the range-momentum cuts and the energy cut are uncorrelated, in order to estimate the expected number of events in the normalization branch (N_{norm}); 13 events are left in the normalization branch of the 2nd bifurcation in the sample after the energy cut is reversed ($N_{RP} = 13$). On the other hand, in a sample after the range-momentum cuts are reversed, 13 events out of 1782 events survived after imposing the energy cut, and the rejection R_E was estimated to be 1782/13=137.1. The number of events in the normalization branch from the 2nd bifurcation is therefore estimated to be

$$\begin{aligned} N_{norm} &= \frac{N_{RP}}{R_E - 1} \\ &= \frac{13}{1782/13 - 1} = 0.096 \pm 0.035. \end{aligned}$$

Photon Cuts were studied in the rejection branch with the events that failed the $K^+ \to \pi^+\gamma\gamma$ kinematic cuts. Kinematic cuts for selecting $K_{\pi 2}$ (box cuts on the momentum, range and energy) were imposed to purify the sample. 5600 events out of 53723 events survived after imposing all of the photon cuts. The rejection of the photon cuts R_{PTN} is estimated to be

$$R_{PTN} = \frac{53723}{5600} = 9.59 \pm 0.12.$$

The range and energy distributions before and after imposing the photon cuts are shown in the right figure of Fig. 4.4. Based on these numbers, the $K_{\pi 2}$ background from the 2/3 sample is estimated to be

$$\begin{aligned} N_{K_{\pi 2}} &= \frac{N_{norm}}{R_{PTN} - 1} \\ &= \frac{0.096}{9.59 - 1} = 0.011 \pm 0.004. \end{aligned}$$

By multiplying a factor of 1.5, the $K_{\pi 2}$ background to the full sample is <u>0.017±0.006</u>. Details of the $K_{\pi 2}$ background study are described in Appendix B.1.

The background probability functions for the $K_{\pi 2}$ background are constructed as follows. The $K_{\pi 2}$ kinematic function is constructed by varying the cut positions of the kinematic cuts on the lower side (213.3 MeV/c for the momentum, 33.5 cm for the range and 116.0 MeV for the energy) simultaneously. The photon-cut function is constructed by varying the cut positions of the Photon Cuts (100 MeV/c^2 for $M_{\gamma\gamma}$ and 112.5 cm for z_{disc}) simultaneously. The $K_{\pi 2}$ kinematic function and photon-cut function are shown in Fig. 4.5.

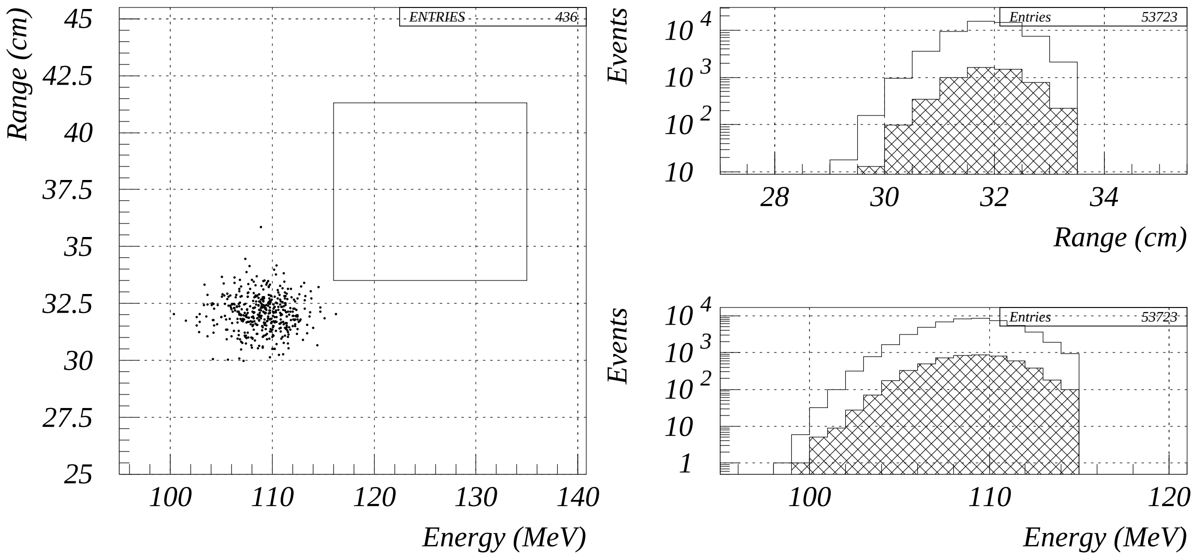

Figure 4.4: Range-energy plots of the events in the normalization branch after Photon Cuts reversed and after the $K^+ \to \pi^+\gamma\gamma$ momentum cut (left); range (top-right) and energy (bottom-right) distributions of the events in the rejection branch. The shaded histograms represent the distributions after imposing the Photon Cuts.

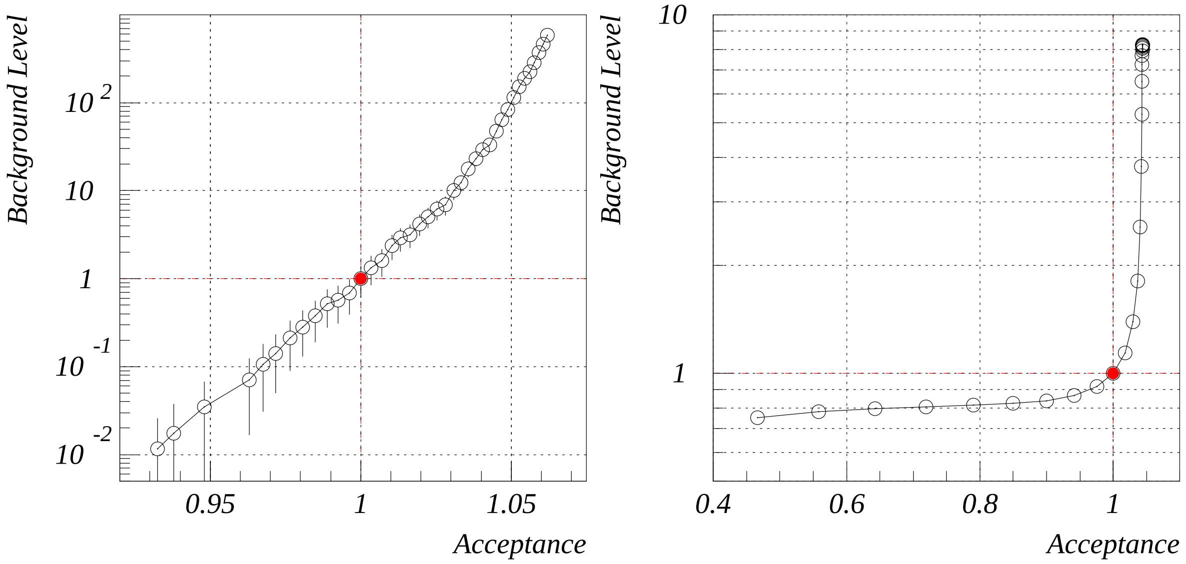

Figure 4.5: $K_{\pi 2}$ kinematic function (left) and photon-cut function (right). The original cut position is indicated by the filled circle in each figure.

4.1.3 Correlation Check

The correlation between two bifurcation cuts was studied by simultaneously loosening the cut positions of the kinematic cuts and the photon cuts. The loosening factors were obtained from the background probability functions. The results are shown in Fig. 4.6 and Table 4.1. The open circles are the observed number of events outside of the search region, and the filled circles are the predicted number of events from the background probability functions. The observed numbers of events are consistent with the predictions, which indicates that there is no or negligible correlation between the kinematic cuts and photon cuts.

The validity of the 2nd bifurcation between the range-momentum cuts and the energy cut was also studied. Fig. 4.7 shows the numbers of events in the normalization branch from the 1st bifurcation (histogram) and from the 2nd bifurcation (open-circles) as a function of the cut position of kinematic cuts on linear (top-left) and logarithmic (top-right) scales. The ratio of the number of events in the normalization branch from the 1st bifurcation to the corresponding number from the 2nd bifurcation is also shown in the bottom figure of Fig. 4.7. Since the line shape agrees with each other outside to the search region, the number of events in the normalization branch from the 2nd bifurcation can be used in a $K_{\pi 2}$ background study.

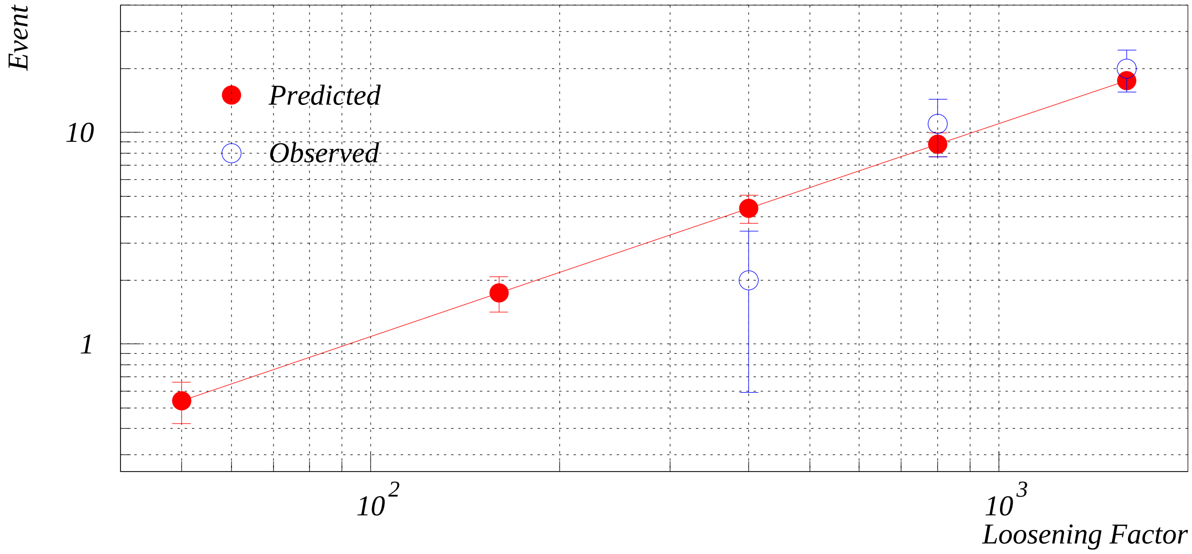

Figure 4.6: Results of a correlation check for the $K_{\pi 2}$ background study. The open-circles are the observed number of events outside of the search region. The filled-circles are the predicted number of events from the background probability functions.

KIN×PTN	prediction	observed
10×5	0.54±0.12	0±0
20×8	1.75±0.33	0±0
50×8	4.39±0.67	2±1.41
100×8	8.79±1.14	11±3.32
200×8	17.59±1.94	20±4.47

Table 4.1: Correlation check for the $K_{\pi 2}$ background study. The left column gives the loosening factors obtained from each background probability function. The middle column gives the predicted number of events from the background probability functions. The right column gives the observed number of events outside of the search region.

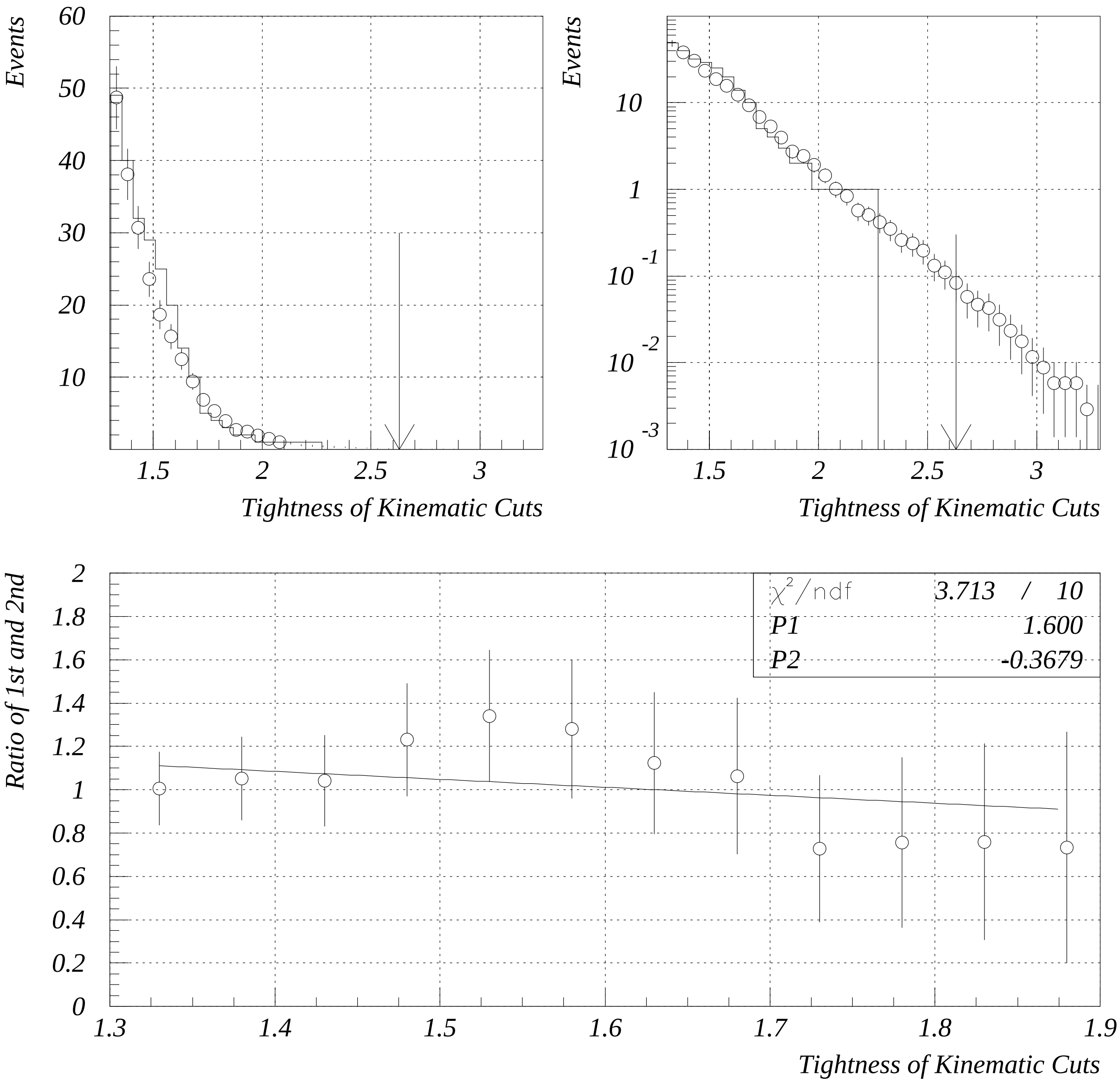

Figure 4.7: Numbers of the events in the normalization branch from the 1st bifurcation (histogram) and from the 2nd bifurcation (open-circles) as a function of the cut position of kinematic cuts in linear (top-left) and logarithmic (top-right) scales; the ratio of the number of events in the normalization branch from the 1st bifurcation and the corresponding number from 2nd bifurcation (bottom).

4.2 Overlapping Photon Background

4.2.1 Overlapping Photon Cuts

The two bifurcation cuts for the overlapping-photon background estimation are:

- cuts on the charged track kinematics, and
- cuts on dE/dx in the Range Stack counters,

each of which is described below.

Kinematic Cuts

The overlapping photon background is removed by cuts on the momentum, range and kinetic energy of the π^+ track. The cut positions are the same as those described in the $K_{\pi 2}$ background section.

Range Stack dE/dx Cuts

The cuts on the dE/dx in the Range Stack counters consist of three cuts based on the measured energy deposits ($E_{meas.}$) and the expected energy deposits from the measured range ($E_{expt.}$) in the Range Stack counters. χ_{RSDEDX} is defined as

$$\chi_{RSDEDX} \equiv \frac{\Delta \log(E)}{\sigma_E},$$

where $\Delta \log(E)$ is an expression of the residual of the measured and expected energies,

$$\Delta \log(E) \equiv \log(E_{expt.}) - \log(E_{meas.}).$$

σ_E is obtained for each layer as a function of the stopping layer of the charged track. The confidence level is computed by summing χ^2_{RSDEDX} for all track counters, except for the T-counter, sector crossing counters and the stopping counter, and the cut position is set to be $\geq 2\%$. The top figure of Fig. 4.8 is confidence-level distributions for the π^+-track events in the π_{scat} monitor data and for the overlapping photon events in the background sample. The top-right figure is a zoom up of the top-left figure; the cut position is indicated by the arrow. The maximum value among the χ_{RSDEDX} measurements (χ^{MAX}_{RSDEDX}) also rejects the background efficiently. The middle figure of Fig. 4.8 shows the χ^{MAX}_{RSDEDX} distributions for the π^+-track events in the π_{scat} monitor data and for the overlapping photon events in the background sample. The cut positions are indicated by the arrows in the figure; it is is required that $|\chi^{MAX}_{RSDEDX}| \leq 4$. A likelihood formed by the $\Delta \log(E)$ also discriminates the signal from the background. The bottom figure of Fig. 4.8 is the likelihood distributions for the π^+-track events in the π_{scat} monitor data and for the overlapping photon events in the background sample. The cut position is indicated by the arrow in the figure, and is set to be 10.0.

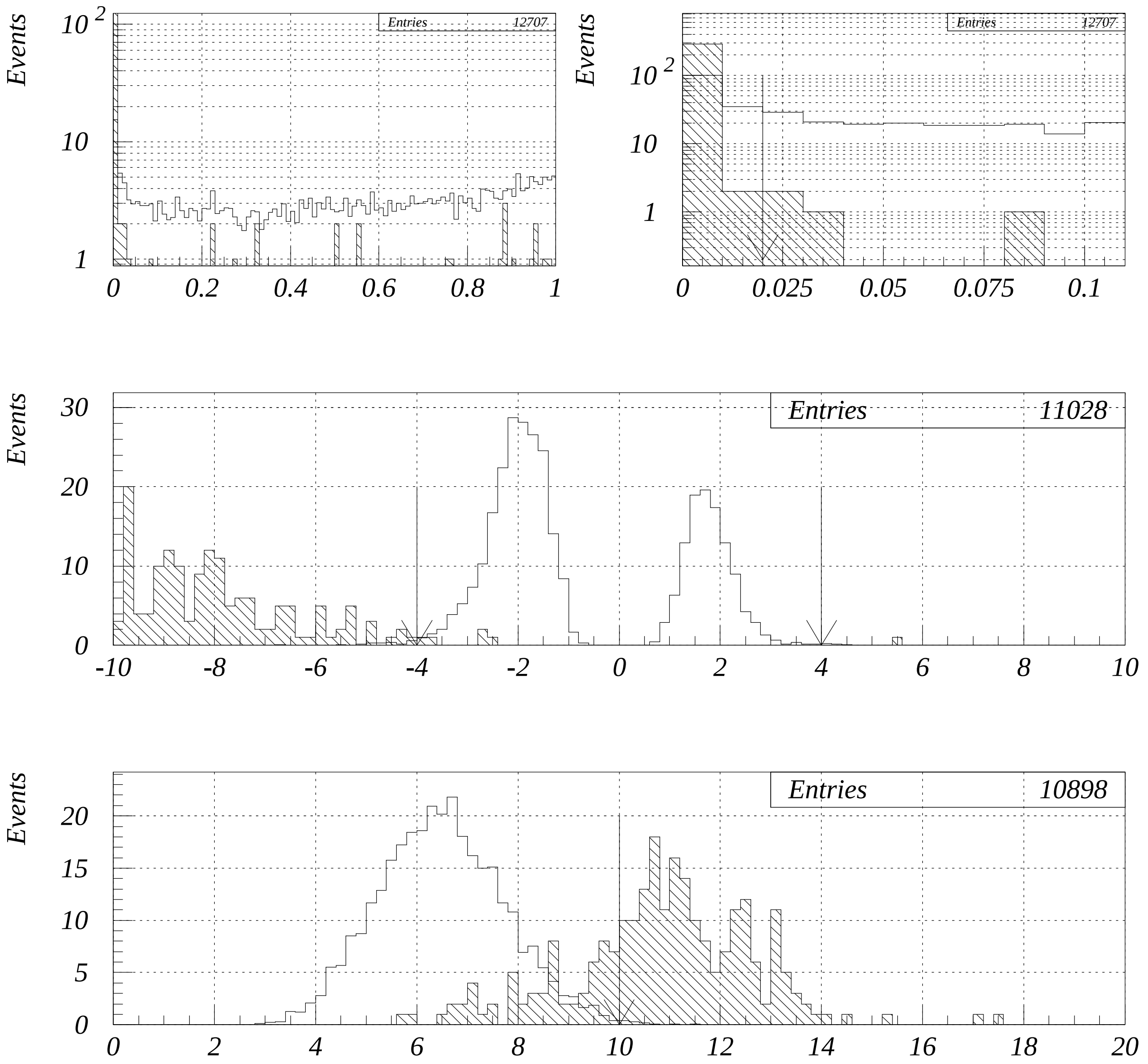

Figure 4.8: Distributions of the confidence level (Top), the maximum value among the χ_{RSDEDX} measurements (middle) and the likelihood value (bottom) for for the π^+-track events (open histogram) in the π_{scat} monitor data and the overlapping photon events (shaded histogram) in the background sample.

4.2.2 Overlapping-Photon Background Estimation

Backgrounds in the kinematic tail are studied in the normalization branch, in which the events that fail the Range Stack dE/dx cuts are tagged. Range-energy plots of the events in the normalization branch, after the Range Stack dE/dx cuts reversed (left) and after the $K^+ \to \pi^+\gamma\gamma$ momentum cut (right) are shown in Fig. 4.9. The events whose energy is 20MeV higher than the $K_{\pi 2}$ peak are the π^+ tracks on which the lower energy photon from π^0 is overlapped. One event is left within the $K^+ \to \pi^+\gamma\gamma$ range and the energy cuts.

The Range Stack dE/dx cuts are studied in the rejection branch, in which events in the $K_{\pi 2}$ sample are used. Fig. 4.10 shows the range-energy plot (left) and the energy distribution (right) of the $K_{\pi 2}$ sample within the $K_{\pi 2}$ momentum and range cuts, after imposing all of the cuts, except for the Range Stack dE/dx cuts and the $K^+ \to \pi^+\gamma\gamma$ energy cut. In order to estimate the Range Stack dE/dx rejection, the $K_{\pi 2}$ contamination within the $K^+ \to \pi^+\gamma\gamma$ energy cut (116MeV $< E <$ 135MeV) had to be estimated in advance. For this purpose, the $K_{\pi 2}$ peak was fitted by a Gaussian, and the contributions were subtracted from each bin; 7.2 events out of 177.2 survived within the $K^+ \to \pi^+\gamma\gamma$ energy cut after imposing the Range Stack dE/dx cuts. The rejection of the Range Stack dE/dx cuts is therefore estimated to be

$$R_{RSDEDX} = \frac{177.2}{7.2} = 24.5.$$

Based on these numbers, the overlapping photon background from the 2/3 sample is estimated to be

$$\begin{aligned} N_{Overlap} &= \frac{N_{norm}}{R_{RSDEDX} - 1} \\ &= \frac{1}{177.2/7.2 - 1} = 0.043 \pm 0.043. \end{aligned}$$

Since the number of event in the normalization branch N_{norm} is one, and it is hard to do a 2nd bifurcation for this background, a statistical error of 100% is assigned to the estimation. By multiplying a factor of 1.5, the overlapping photon background to the full sample is $\underline{0.065 \pm 0.065}$. Details of the overlapping-photon background study are described in Appendix B.2.

The background probability function was not constructed due to a lack of statistics.

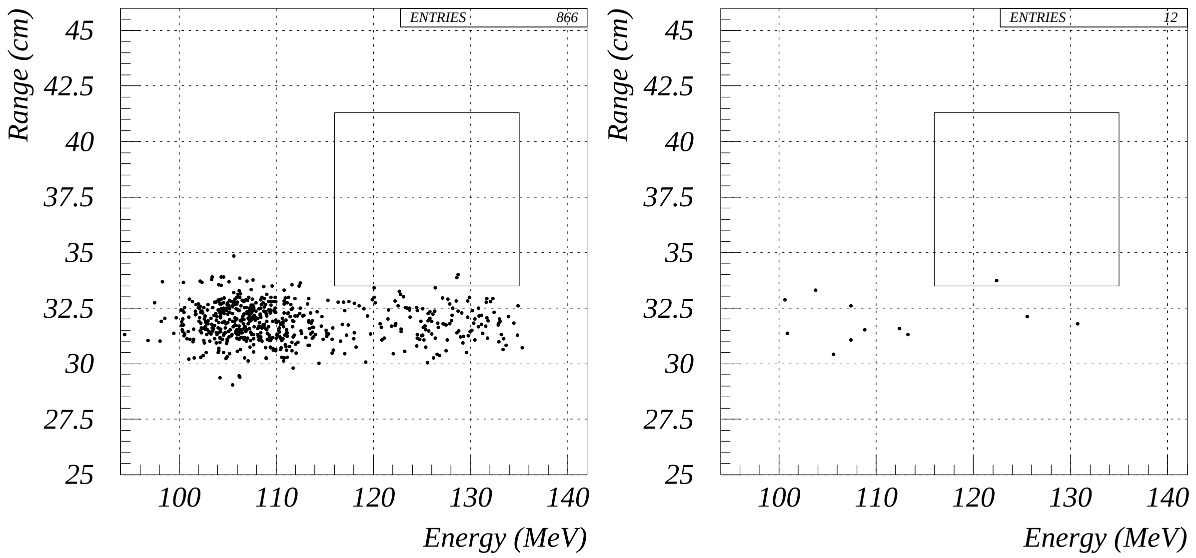

Figure 4.9: Range-energy plots of the events in the normalization branch before (left) and after (right) imposing the $K^+ \to \pi^+\gamma\gamma$ momentum cut.

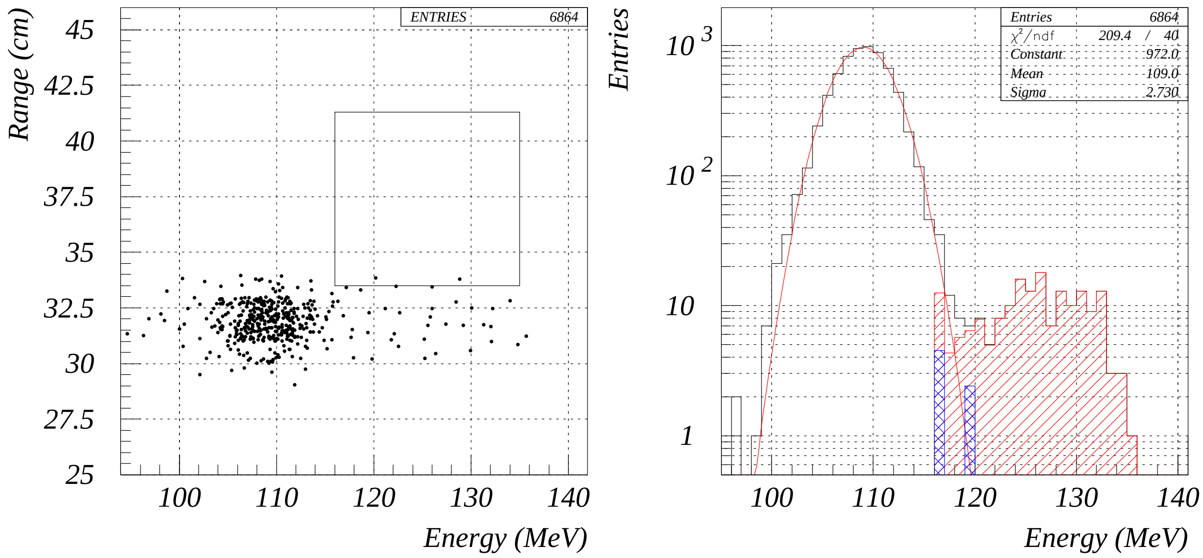

Figure 4.10: Range-energy plot (left) and energy distribution (right) of events in the rejection branch. The hatched histogram represents the distribution after subtracting the $K_{\pi 2}$ peak. The double-hatched histogram represent the distribution after imposting the Range Stack dE/dx cuts.

4.3 Muon Background

4.3.1 Muon Background Cuts

The two bifurcation cuts for the muon background estimation are:

- cuts on the charged track kinematics, and
- cuts on the requirement of a $\pi^+ \to \mu^+ \to e^+$ decay chain in the stopping counter,

each of which is described below.

Kinematic Cuts

The cuts on the momentum, range and kinetic energy remove the muon background, as in the case of the $K_{\pi 2}$ background. In addition, a cut on the relation between the momentum and the range (χ_{RP}) discriminates the π^+ efficiently from μ^+. χ_{RP} is defined as

$$\chi_{RP} \equiv \frac{R_{meas.} - R_{expt.}}{\sigma_R},$$

where $R_{meas.}$ is the measured range in the Range Stack, $R_{expt.}$ is the expected range from the momentum by assuming that the track is a π^+, and σ_R is the sigma of the range distribution at the measured momentum. Fig. 4.11 shows the χ_{RP} distributions for the π^+-track events in the π_{scat} monitor data and for the μ^+-track events in the background sample. The cut position is set to be $\chi_{RP} < 2.2$ and is indicated by the arrow in the figure.

Particle Identification Cuts

As described in section 3.3.1, a μ^+ could be mis-identified as a π^+ in the stopping counter. A number of cuts requiring a $\pi^+ \to \mu^+ \to e^+$ decay chain are prepared to remove this background. The neural network (NN) cut has the largest rejection among these cuts. The NN cut is formed by using five variables from the fitting of the pulse shapes recorded in the Transient Digitizer; the χ^2 of the single-pulse fit, the χ^2 ratio of the single-pulse fit to the double-pulse fit, μ^+ energy, time difference of μ^+ between both ends and μ^+ time. Fig. 4.12 shows the output value of the NN for the π^+-track events in the π_{scat} monitor data and the μ^+-track events in the background sample. The cut position is indicated by the arrow in the figure; the NN output value is required to be greater than 0.76.

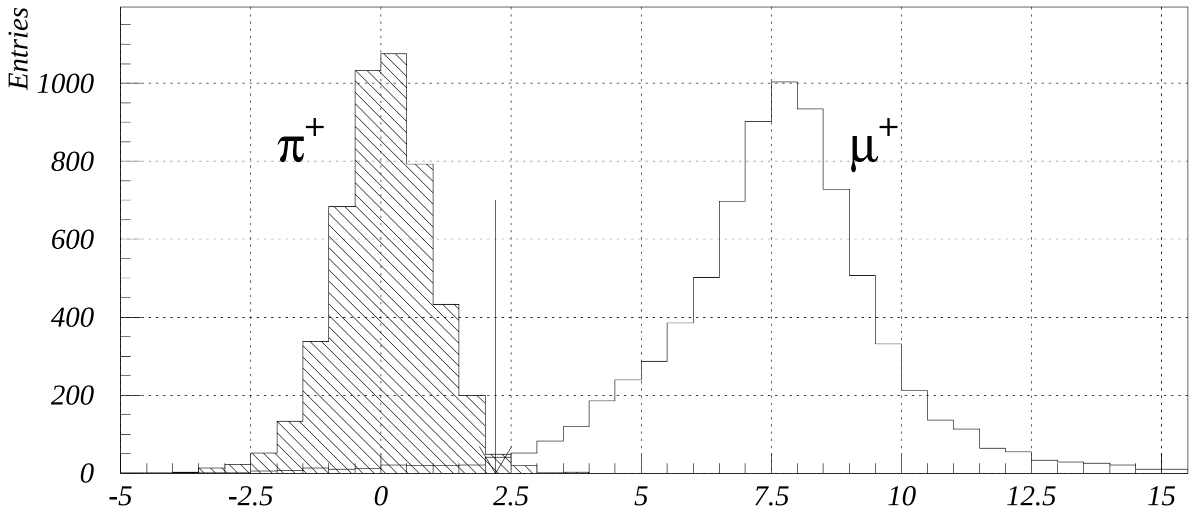

Figure 4.11: χ_{RP} distribution for the π^+ track events (shaded histogram) in the π_{scat} monitor data and the μ^+ track events (open histogram) in the background sample.

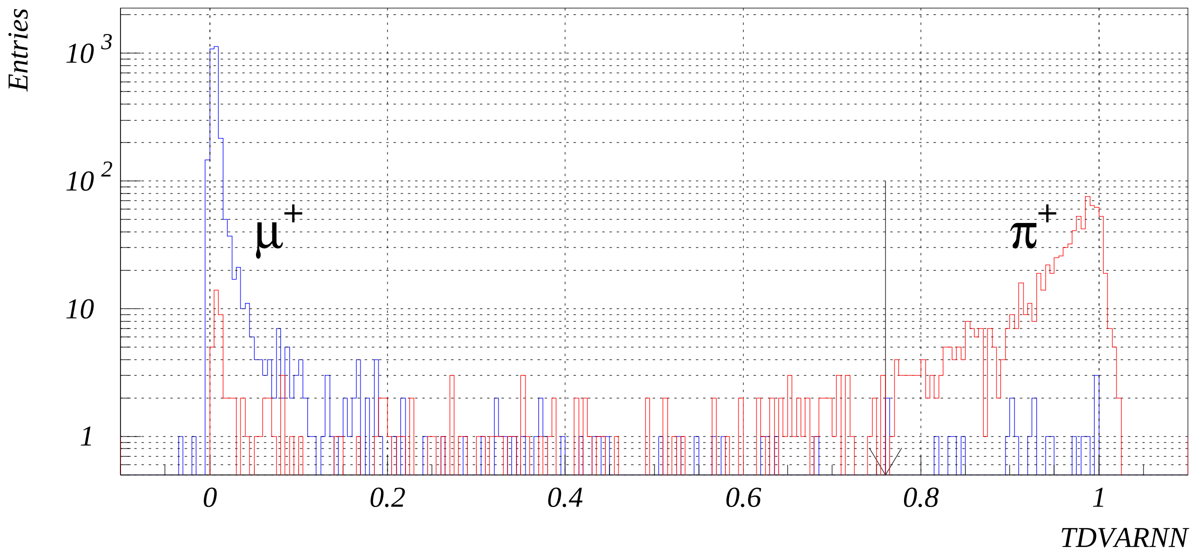

Figure 4.12: Output value of the neural network for the π^+ track events in the π_{scat} monitor data and the μ^+ track events in the background sample.

4.3.2 Muon Background Estimation

Backgrounds in the muon kinematic tail are studied in the normalization branch, in which the events that failed one of the $\pi^+ \to \mu^+ \to e^+$ requirement cuts are tagged. The range-energy plot of the events in the normalization branch, after the $K^+ \to \pi^+\gamma\gamma$ momentum cut, is shown in the left figure of Fig. 4.13; 44 events are left within the $K^+ \to \pi^+\gamma\gamma$ range and energy cuts ($N_{norm} = 44$).

The $\pi^+ \to \mu^+ \to e^+$ requirement cuts are studied in the rejection branch. The energy distributions of the events in the rejection branch before and after the $\pi^+ \to \mu^+ \to e^+$ requirement cuts are shown in the right figure of Fig. 4.13. The rejection of the $\pi^+ \to \mu^+ \to e^+$ requirement cuts is calculated to be

$$R_{TD} = \frac{34680}{47} = 737.9 \pm 107.6.$$

Based on these numbers, the muon background from the 2/3 sample is estimated to be

$$\begin{aligned} N_{Muon} &= \frac{N_{norm}}{R_{TD} - 1} \\ &= \frac{44}{34680/47 - 1} = 0.060 \pm 0.013. \end{aligned}$$

By multiplying a factor of 1.5, the muon background to the full sample is $\underline{0.090 \pm 0.020}$. Details concerning the muon background study are described in Appendix B.3.

The background probability functions for the muon background are constructed as follows. The muon kinematic function is constructed by varying the cut positions of the kinematic cuts on χ_{RP} (2.2), the lower momentum (213.3 MeV/c) and the upper range (41.3 cm) simultaneously. The $\pi^+ \to \mu^+ \to e^+$ requirement-cut function is constructed by varying the cut position of the NN cut (0.76). The muon kinematic function and $\pi^+ \to \mu^+ \to e^+$ requirement-cut function are shown in Fig. 4.14.

4.3.3 Correlation Check

The correlation between two bifurcation cuts are studied by simultaneously loosening the cut positions of the kinematic cuts and the $\pi^+ \to \mu^+ \to e^+$ requirement cuts. The loosening factors are obtained from the background probability functions. The results are shown in Fig. 4.15 and Table 4.2. The opened-circles are the observed number of events outside of the search region, and the filled-circles are the predicted number of events from the background probability functions. The observed number of events are statistically consistent with the predictions, which indicates that there are no or negligible correlation between the kinematic cuts and the $\pi^+ \to \mu^+ \to e^+$ requirement cuts.

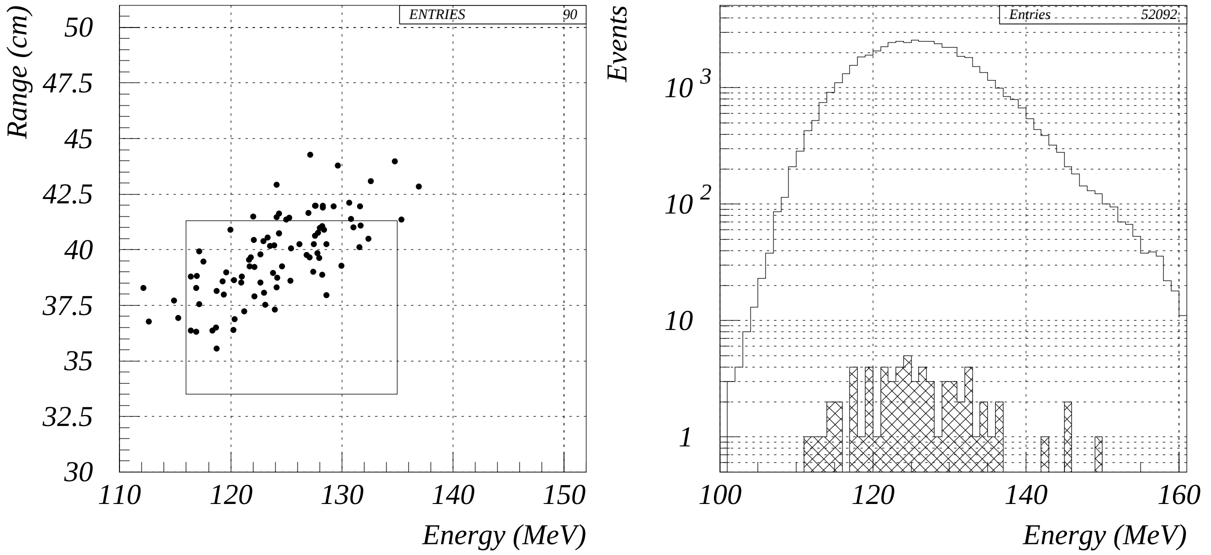

Figure 4.13: Range-energy plot of the events in the normalization branch after the $K^+ \to \pi^+\gamma\gamma$ momentum cut (left); energy distributions of the events in the rejection branch before (open histogram) and after (shaded histogram) the $\pi^+ \to \mu^+ \to e^+$ requirement cuts.

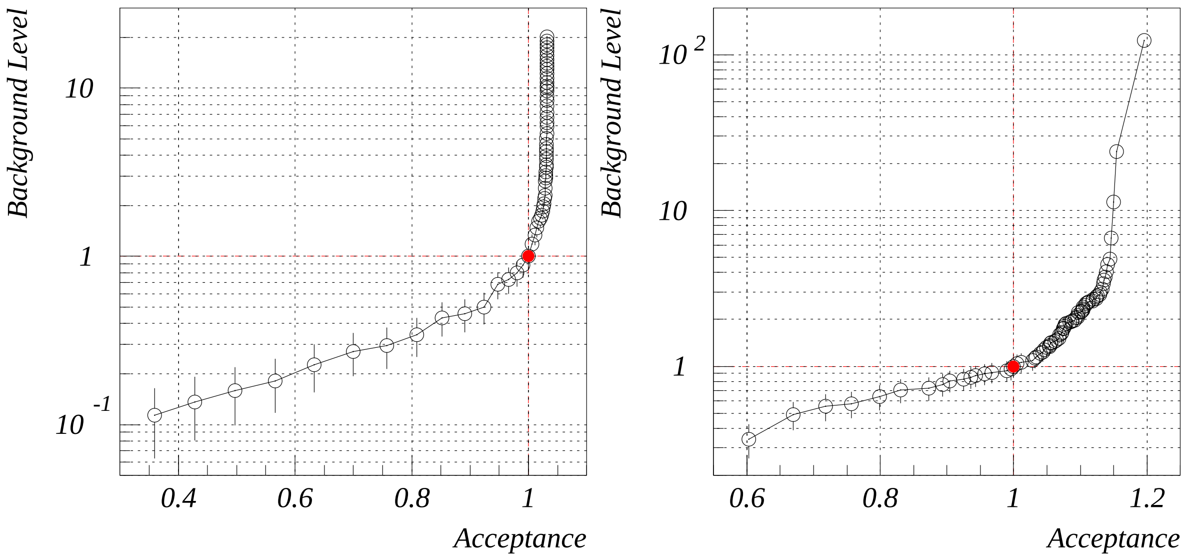

Figure 4.14: Muon kinematic function (left) and $\pi^+ \to \mu^+ \to e^+$ requirement-cut function (right). The original cut position is indicated by the filled circle in each figure.

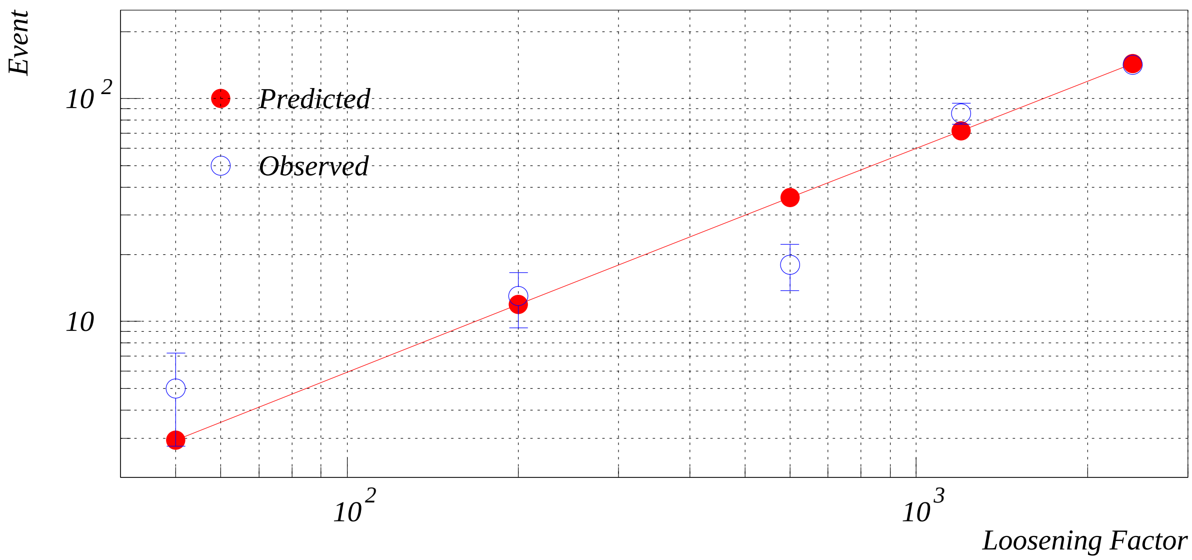

Figure 4.15: Results of the correlation check for the muon background study. The open-circles are the observed number of events outside of the search region. The filled-circles are the predicted number of events from the background probability functions.

TD×KIN	prediction	observed
10×5	2.94±0.24	5±2.24
20×10	11.94±0.68	13±3.61
40×15	35.94±1.62	18±4.24
80×15	71.94±2.94	86±9.27
120×20	143.94±4.86	142±11.92

Table 4.2: Correlation check for the muon background study. The left column gives the loosening factors obtained from each background probability function. The middle column gives the predicted number of events from the background probability functions. The right column gives the observed number of events outside of the search region.

4.4 Single-Beam Background

4.4.1 Single Beam Cuts

The two bifurcation cuts for the single-beam background estimation are:

- offline delayed-coincidence cuts and
- timing cut on the Kaon Čerenkov counter,

each of which is described below.

Delayed Coincidence Cuts

Fig. 4.16 shows the distribution of the time difference between the incoming kaon and the outgoing charged-decay product in the Target for the $K_{\mu 2}$ decay (after imposing the online delayed coincidence) and for the kaon decay-in-flight events in the background sample. The Delayed Coincidence basically requires that the decay product should be observed at least 2 nsec later than the time when a kaon comes to rest in the Target. The cut position is indicated by the arrow in the figure. The cut position is slightly tightened according to the quality of the timing reconstructions in the Target.

Kaon Čerenkov Cut

Events are rejected if there is a reconstructed hit in the Kaon Čerenkov counters at the Range Stack time. A Kaon Čerenkov hit is reconstructed with the coincident hits of 4 or more PMTs; the reconstruction is performed by using the timing information from TDCs and CCDs. Fig. 4.17 shows the distributions of the times from the Kaon Čerenkov-counter hits based on TDCs (left) and CCDs (right), relative to the Range Stack time, for the $K_{\mu 2}$ events and for the kaon decay-in-flight events in the background sample. The time window is set to be ± 2 nsec, and is indicated by the arrows in the figure.

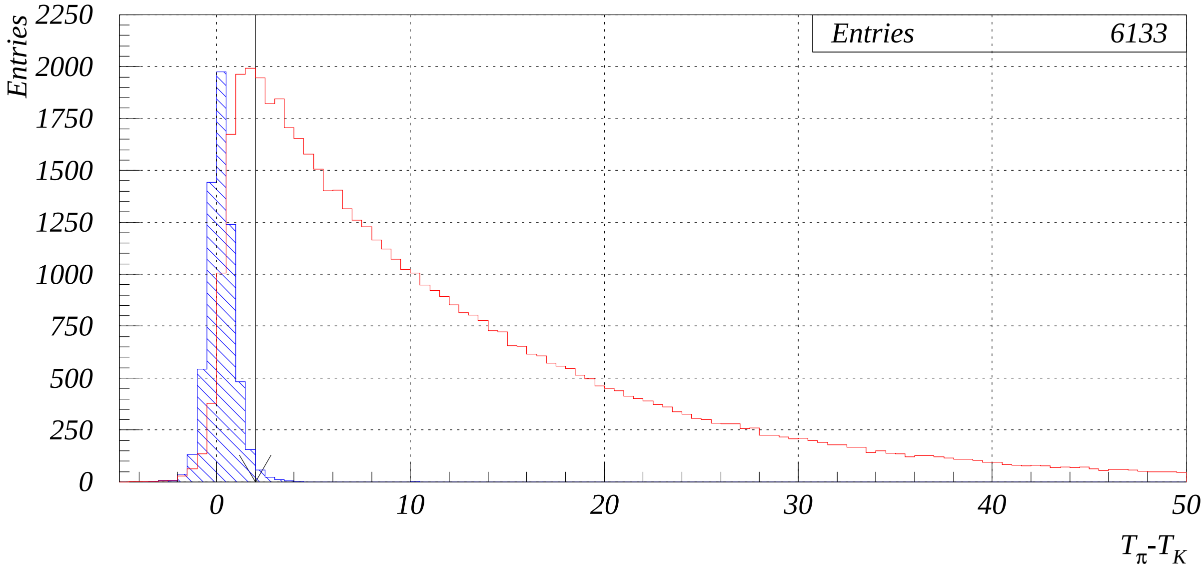

Figure 4.16: Distribution of the time difference between the incoming and outgoing particles in the Target for the $K_{\mu2}$ events (open histogram) and for the kaon decay-in-flight events (shaded histogram) in the background sample.

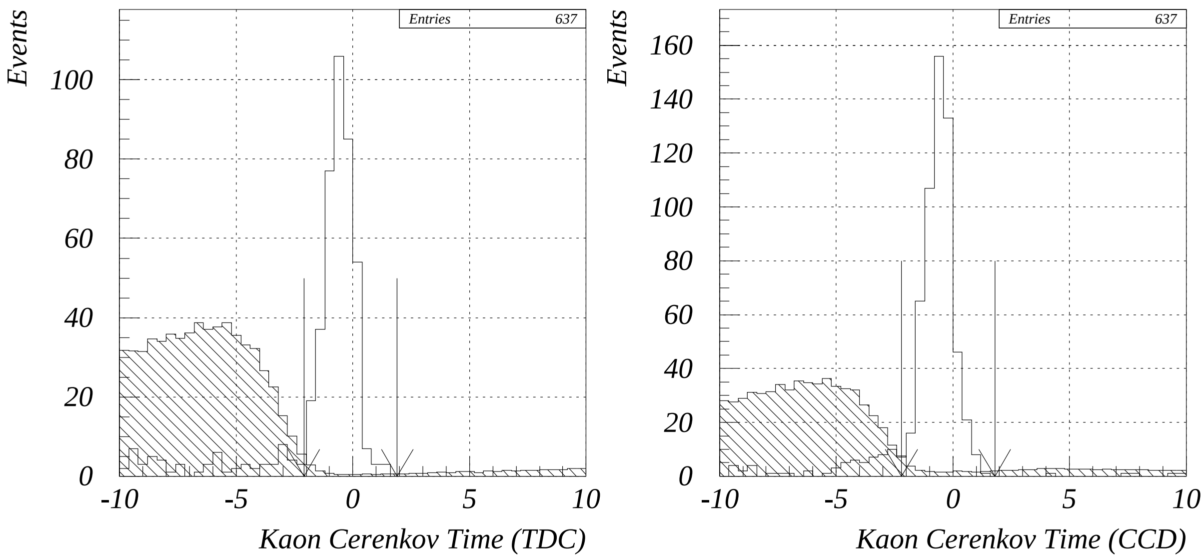

Figure 4.17: Distributions of the time from the Kaon Cerenkov-counter hit based on TDCs (left) and CCDs (right), relative to the Range Stack time, for the $K_{\mu2}$ events (shaded histogram) and the kaon decay-in-flight events in the background sample (open histogram).

4.4.2 Single-Beam Background Estimation

Backgrounds due to the kaon decay-in-flight are studied in the normalization branch, in which the events that failed the Delayed Coincidence cuts are tagged. The number of events in the normalization branch was estimated using the 2nd bifurcation based on the assumption that the Kaon Čerenkov cuts, and the $\pi^+ \to \mu^+ \to e^+$ requirement and Photon cuts are uncorrelated. For the events that failed the Kaon Čerenkov cuts, 28 events survived after the $\pi^+ \to \mu^+ \to e^+$ requirement cuts and Photon cuts ($N_k = 28$); for the 401 events that failed the $\pi^+ \to \mu^+ \to e^+$ requirement or Photon cuts, 43 events survived the Kaon Čerenkov cuts ($R_k = 401/43 = 9.33$). The number in the normalization branch N_{norm} was estimated to be

$$\begin{aligned} N_{norm} &= \frac{N_k}{R_k - 1} \\ &= \frac{28}{401/43 - 1} = 3.36 \pm 0.80. \end{aligned}$$

The Delayed Coincidence cuts are studied in the rejection branch, in which the events that fail one of the timing cuts on the Kaon Čerenkov counter are tagged. Fig. 4.18 shows the time difference between the incoming kaon and outgoing charged-decay product in the Target before and after imposing the Delayed Coincidence cuts; 4 events[2] out of 820 events survived after imposing the Delayed Coincidence cuts. The rejection of Delayed Coincidence cuts R_{DELC} is estimated to be

$$R_{DELC} = \frac{820}{4} = 205.0 \pm 102.2.$$

Based on these numbers, the single beam background from the 2/3 sample is estimated to be

$$\begin{aligned} N_{1beam} &= \frac{N_{norm}}{R_{DELC} - 1} \\ &= \frac{3.36}{820/4 - 1} = 0.016 \pm 0.009. \end{aligned}$$

By multiplying a factor of 1.5, the single-beam background to the full sample is $\underline{0.025 \pm 0.014}$. Details of the single-beam background study are described in Appendix B.4.

The background probability functions for the Single Beam background are constructed as follows. The Delayed Coincidence function is constructed by varying the cut positions of the Delayed Coincidence cuts. The Kaon Čerenkov function is constructed by varying the window on the Kaon Čerenkov time. The Delayed Coincidence function and Kaon Cerenkov function are shown in Fig. 4.19.

[2]Since the Kaon Čerenkov cut is also effective to remove the double-beam background, the inverted Kaon Čerenkov cut could tag the non-prompt events, which can not be removed by the Delayed Coincidence cuts. The remaining non-prompt events are consistent with the estimation from the double beam background study in the next section. Here, the rejection of the Delayed Coincidence cuts is estimated conservatively with the 4 events.

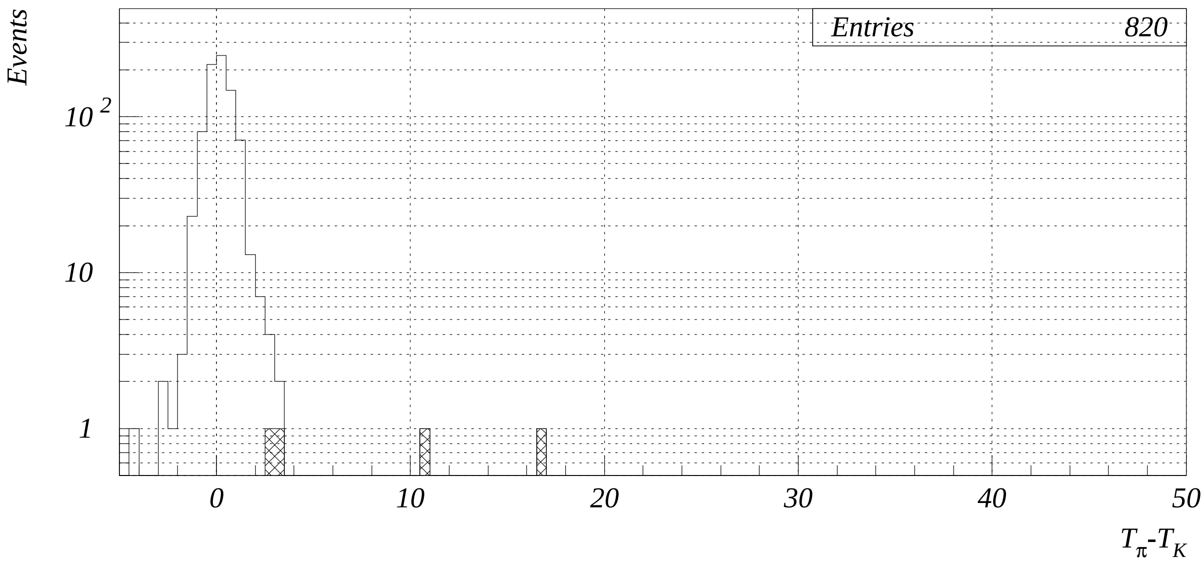

Figure 4.18: Time difference between the incoming K^+ and the charged decay product in the Target before (open histogram) and after (shaded histogram) imposing the Delayed Coincidence cuts.

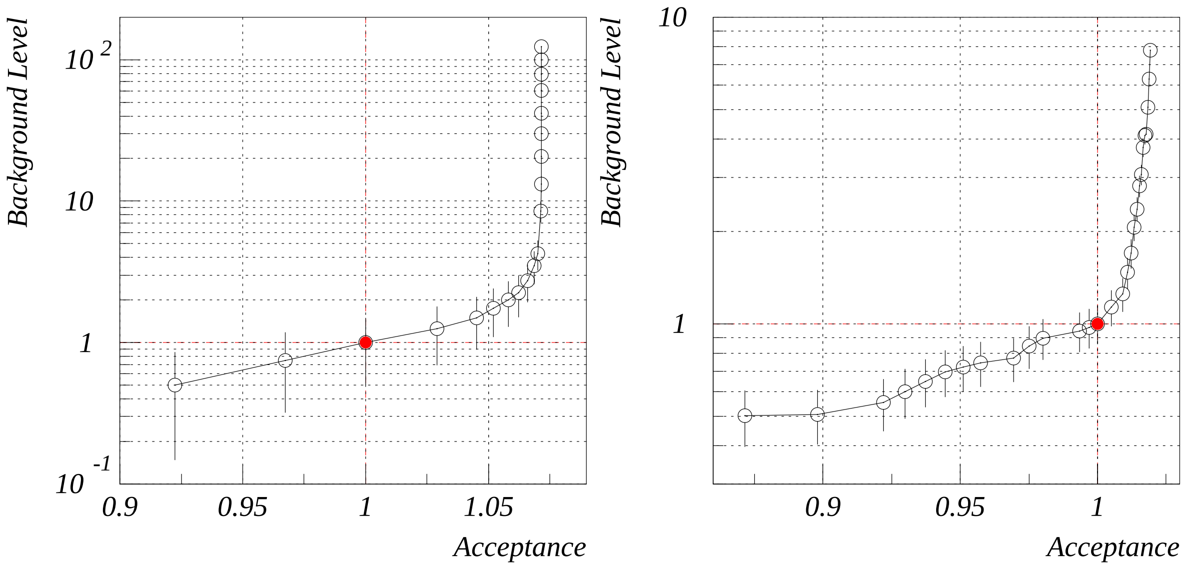

Figure 4.19: Delayed Coincidence function (left) and Kaon Čerenkov function (right). The original cut position is indicated by the filled circle in each figure.

4.4.3 Correlation Check

The correlation between two bifurcation cuts is studied by simultaneously loosening the cut positions of the Delayed Coincidence cuts and the Kaon Čerenkov cut. The loosening factors are obtained from the background probability functions. The results are shown in Fig. 4.20 and Table 4.3. The open circles are the observed number of events outside of the search region, and the filled circles are the predicted number of events from the background probability functions. The observed number of events are consistent with the predictions, which indicates that there is no, or negligible, correlation between the Delayed Coincidence cuts and the Kaon Čerenkov cut.

The validity of the 2nd bifurcation between the Kaon Čerenkov cut, and the $\pi^+ \to \mu^+ \to e^+$ requirement and Photon cuts in the normalization branch is also studied. Fig. 4.21 shows the numbers of events in the normalization branch from the 1st bifurcation (histogram) and from the 2nd bifurcation (open-circle) as a function of the cut position of kinematic cuts in linear (top-left) and logarithmic (top-right) scales. The ratio of the number of events in the normalization branch from the 1st bifurcation and the corresponding number from the 2nd bifurcation is also shown in the bottom figure of Fig. 4.21. Since the line shape agrees with each other outside of the search region, the number of events in the normalization branch from the 2nd bifurcation can be used in a single-beam background study.

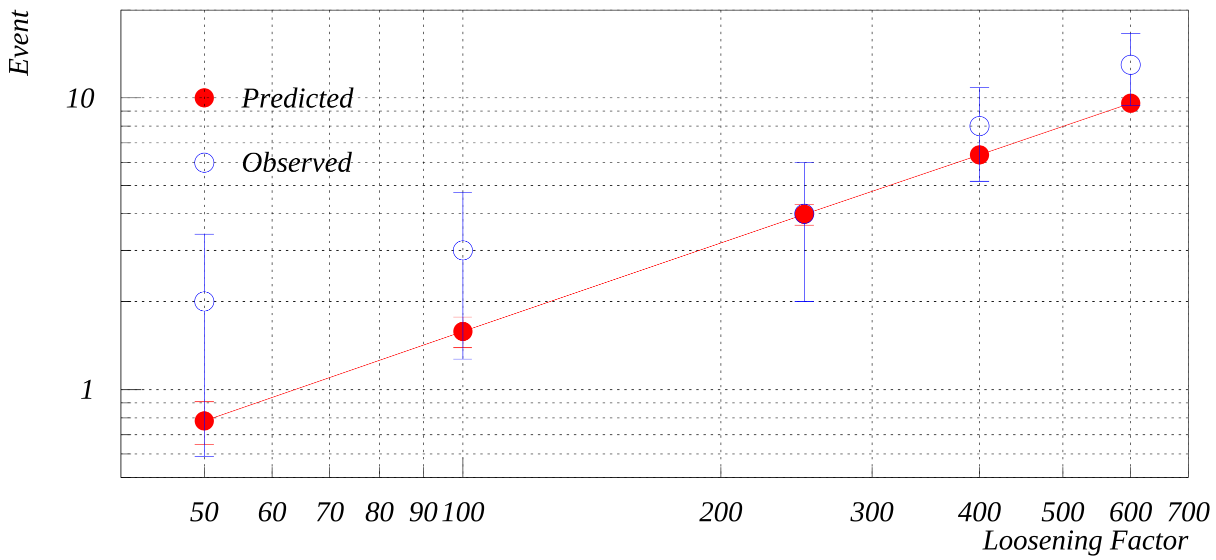

Figure 4.20: Results of the correlation check for the single beam background study. The open-circles are the observed number of events outside of the search region; the filled-circles are the predicted number of events from the background probability functions.

DELC×CKTRS	prediction	observed
10×5	0.78±0.13	2±1.41
20×5	1.58±0.19	3±1.73
50×5	3.98±0.32	4±2.00
80×5	6.38±0.43	8±2.83
120×5	9.58±0.56	13±3.61

Table 4.3: Correlation check for the single beam background study. The left column gives the loosening factors obtained from each background probability function. The middle column gives the predicted number of events from the background probability functions. The right column gives the observed number of events outside of the search region.

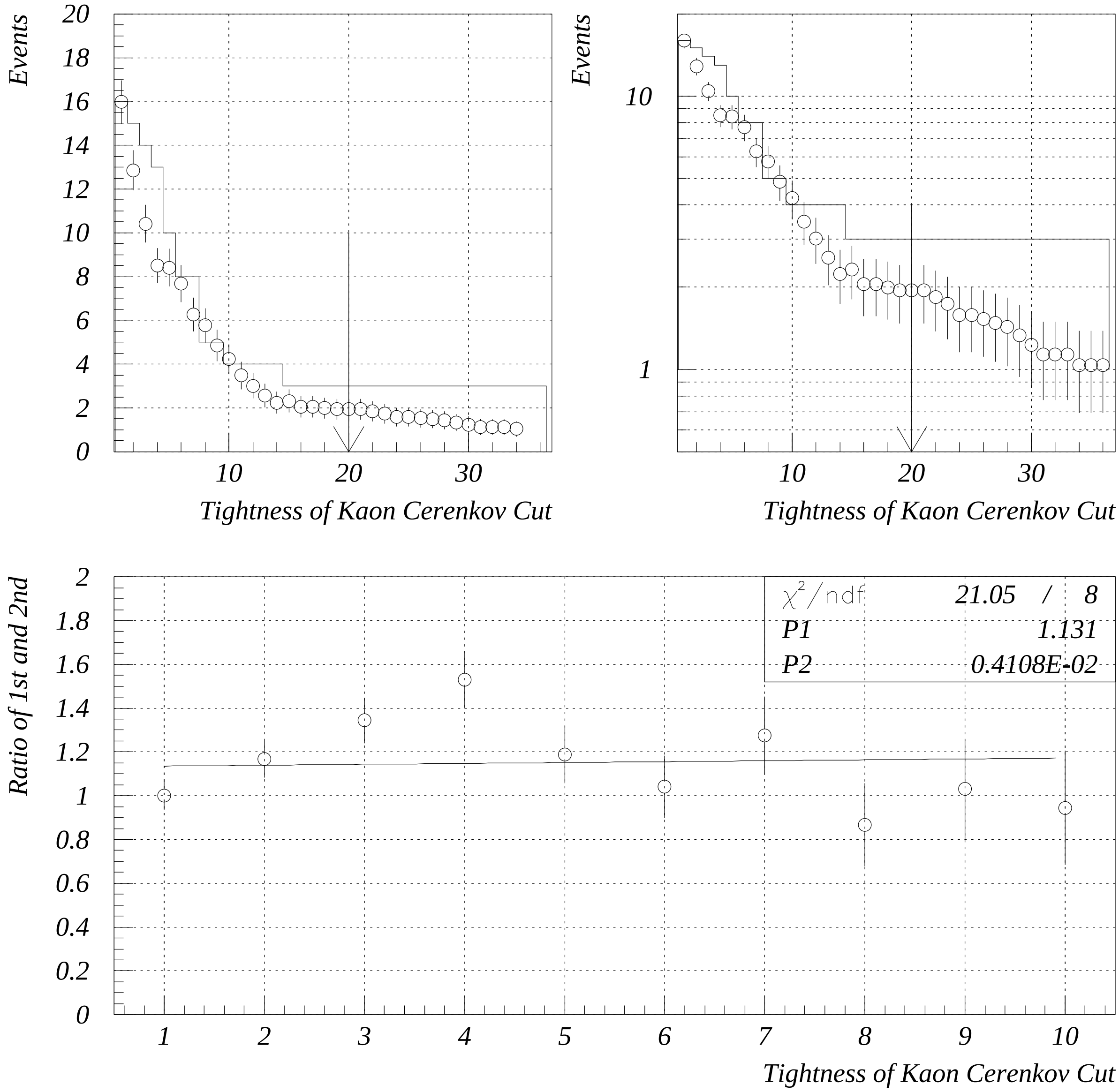

Figure 4.21: Numbers of the events in the normalization branch from the 1st bifurcation (histogram) and the 2nd bifurcation (open-circle) as a function of the cut position of the Kaon Čerenkov cuts in linear (top-left) and logarithmic (top-right) scales; the ratio of number of events in the normalization branch from the 1st bifurcation and 2nd bifurcation (bottom).

4.5 Double-Beam background

4.5.1 Double Beam Cuts

The two bifurcation cuts for the double-beam background estimation are:

- timing cuts on the Čerenkov counters and Beam Wire Chambers and
- timing cuts on the B4 counter,

each of which is described below.

Cuts on the Čerenkov counters and Beam Wire Chambers

- Kaon Čerenkov Cut:
  This cut is described in section 4.4.1, and is also used in a double-beam background study. The top-left histogram of Fig. 4.22 shows the time distributions of Kaon Čerenkov-counter hits, relative to the Range Stack time, for the $K_{\mu2}$ events and for the double-beam background in the background sample.

- Pion Čerenkov Cut:
  Events are rejected if there is a reconstructed hit in the Pion Čerenkov counters at the Range Stack time. A Pion Čerenkov hit is reconstructed with the coincidence hits in 5 or more PMTs. The top-right histogram of Fig. 4.22 shows the time distributions of Pion Čerenkov-counter hit, relative to the Range Stack time, for the $K_{\mu2}$ events and for the double-beam background in the background sample. The time window is set to be ± 2 nsec, and is indicated by the arrows in the figure.

- Beam Wire Chamber Cut:
  Events are rejected if there is a reconstructed hit in the Beam Wire Chambers: BWPC1 and BWPC2. The histograms in the middle of Fig. 4.22 shows the time distributions of the BWPC1 and BWPC2 hits relative to the Range Stack time, for the $K_{\mu2}$ events (shaded histogram) and for the double-beam background in the background sample (open histogram).

Cuts on the B4 Counter

- Timing Cut on the B4 counter:
  Events are rejected if there is a reconstructed hit in the B4 counter. The bottom-left histogram of Fig. 4.22 shows the time distributions of the B4 counter hits, relative to the Range Stack time, for the $K_{\mu2}$ events and for the double-beam background in the background sample. The time window is set to be ± 2.5 nsec, and is indicated by the arrows in the figures.

- Timing Cut on the 2nd Pulse in the B4 Counter:
  Single-pulse and double-pulse fits are performed on the CCD pulse shapes of the B4 counter. Events with a 2nd pulse, whose timing is close to the Range Stack time within ± 3.5 nsec, are rejected. The bottom-right histogram of Fig. 4.22 shows the

time distributions of the 2nd pulse in the B4 counter, relative to the Range Stack time, for the $K_{\mu 2}$ events and for the double-beam background in the background sample. The time window is set to be ± 3.5 nsec and is indicated by the arrows in the figure.

4.5.2 Double-Beam Background Estimation

Backgrounds due to double-beam events are studied in the normalization branch, in which the events that fail any one of the Čerenkov counter cuts and Beam Wire-Chamber cuts are tagged. The number of events in the normalization branch is estimated using the 2nd bifurcation in the assumption that the B4 counter cuts and the Target pattern-recognition cuts are uncorrelated; no event out of 37 events was left in both normalization and rejection branches of the 2nd bifurcation. Taking 2.3 events instead of zero for the 2nd normalization (N_{B4}) and 1 event instead of zero after imposing the Target pattern-recognition cuts ($R_{TG} = 37/1 = 37$), the number in the normalization branch (N_{norm}) is estimated to be

$$
\begin{aligned}
N_{norm} &= \frac{N_{B4}}{R_{TG} - 1} \\
&= \frac{2.3}{37/1 - 1} = 0.064(90\%\text{C.L.}).
\end{aligned}
$$

The cuts on the Čerenkov counters and Beam Wire Chambers are studied in the rejection branch, in which the events that fail one of the B4 counter cuts are tagged. The rejection of the cuts on the Čerenkov counters and Beam Wire Chambers was measured to be

$$
R_{2bm} = \frac{285}{24} = 11.9 \pm 2.3.
$$

Based on these numbers, the double beam background from the 2/3 sample is estimated to be

$$
\begin{aligned}
N_{2beam} &\leq \frac{N_{norm}}{R_{2bm} - 1} \\
&= \frac{0.064}{285/24 - 1} = 0.0059 \quad (90\%\text{C.L.}).
\end{aligned}
$$

and is negligible. Details of the double-beam background study are described in Appendix B.5.

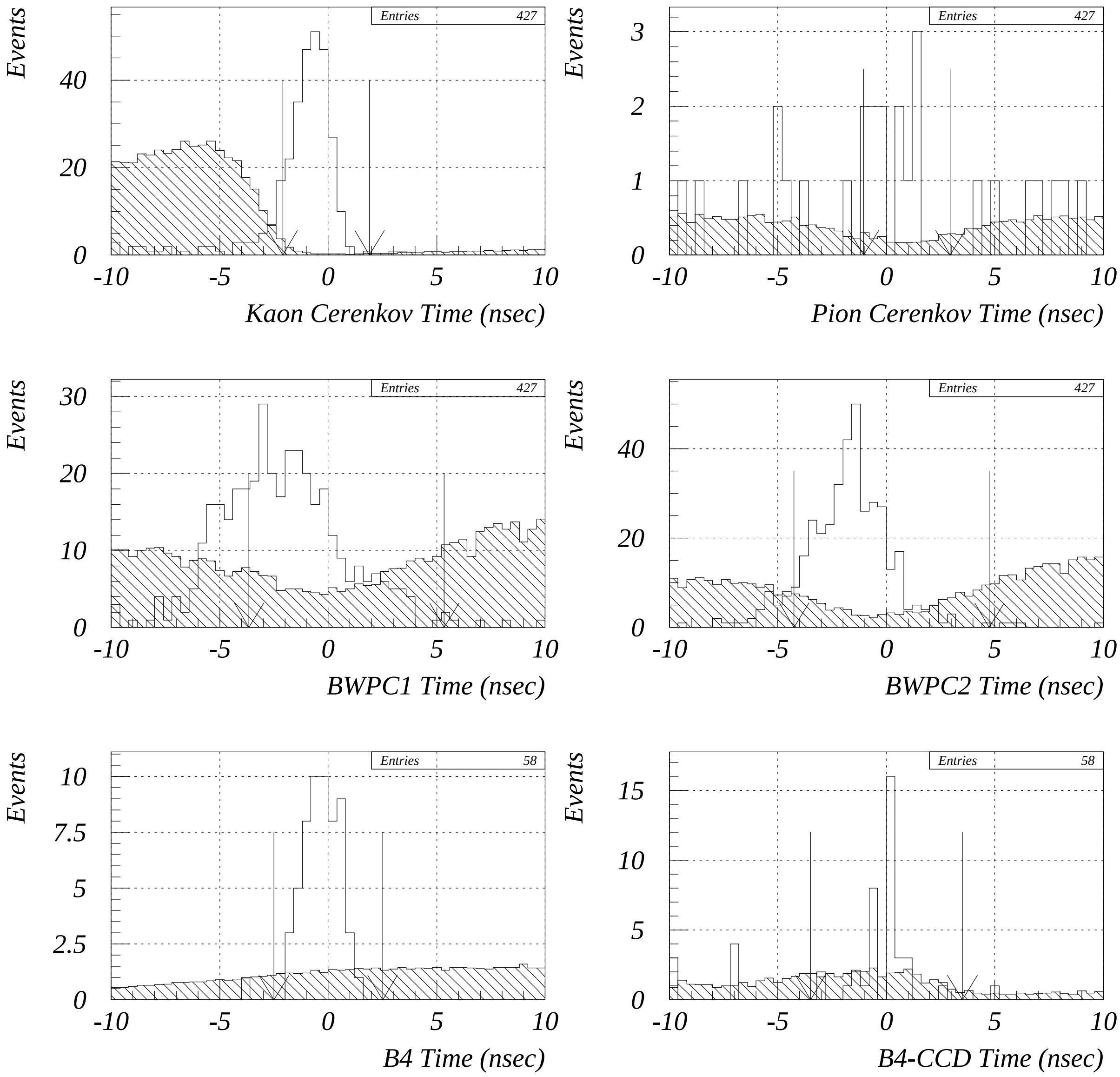

Figure 4.22: Time distribution of the Kaon Čerenkov hits (top-left), Pion Čerenkov hits (top-right), BWPC1 hits (middle-left), BWPC2 hits (middle-right), B4 counter hits (bottom-left) and the 2nd pulses found in the CCDs of the B4 counter (bottom right) for the $K_{\mu 2}$ events (shaded histogram) and for the double-beam background in the background sample (open histogram).

4.6 Summary of the Background Studies

Table 4.4 is a summary of the background studies. The total background level is estimated to be 0.197±0.070. The muon background (0.090 ± 0.020) is dominant. The overlapping photon background (0.065 ± 0.065) has a large uncertainty, since the number of events in the normalization branch is one. The double-beam background is neglected because the limit obtained as a 90% C.L. upper limit is already very small.

Background	Background Level
$K_{\pi 2}$	0.017±0.006
Overlapping Photon	0.065±0.065
Muon	0.090±0.020
Single Beam	0.025±0.014
Double Beam	0.006 (90% C.L.)
Total	0.197±0.070

Table 4.4: Expected background levels to the full sample.

Chapter 5

Results

Results of this analysis are described in this chapter. The search region is examined after imposing all of the offline cuts described in section 5.1. The acceptance factors for the single-event sensitivity calculation are explained in section 5.2. The K^+ stop efficiency is evaluated in section 5.3 in order to obtain the number of effective K^+ decays at rest. The measurement of the $K_{\mu 2}$ branching ratio is described in section 5.4 in order to confirm the validity of the acceptance calculations. The $K^+ \to \pi^+\gamma\gamma$ branching ratio is given in section 5.5.

5.1 Search for the Signal Candidates

After the expected background level to the search region is confirmed to be much smaller than one event, and it is confirmed that there is no or negligible correlation between two bifurcation cuts in each background source, the search region is "opened"; all of the cuts are imposed to the $K^+ \to \pi^+\gamma\gamma$ trigger data and the number of remained events in the search region ($N_{\pi^+\gamma\gamma}$) is counted. The top figure of Fig. 5.1 shows the range-energy plot of the events after imposing all of the cuts, except for the $K^+ \to \pi^+\gamma\gamma$ range and energy cuts. The search region is indicated by the box in the figure. There is no candidate event in the search region, and $N_{\pi\gamma\gamma}$ is obtained to be zero. Table 5.1 gives a series of imposed cuts together with the remaining number of events. The events clustered in the range of 32 cm and an energy of 110 MeV[1] are the remaining $K_{\pi 2}$ background. The $K^+ \to \pi^+\gamma\gamma$ Monte Carlo events under the same online and offline requirements are shown in the bottom figure of Fig. 5.1.

[1]These values are slightly larger than the expected values for $K_{\pi 2}$ (R=30.37 cm and E=108.55 MeV) due to the fact that the stopping layer requirement in the trigger would collect the $K_{\pi 2}$ events whose range and energy are measured to be larger in the Range Stack.

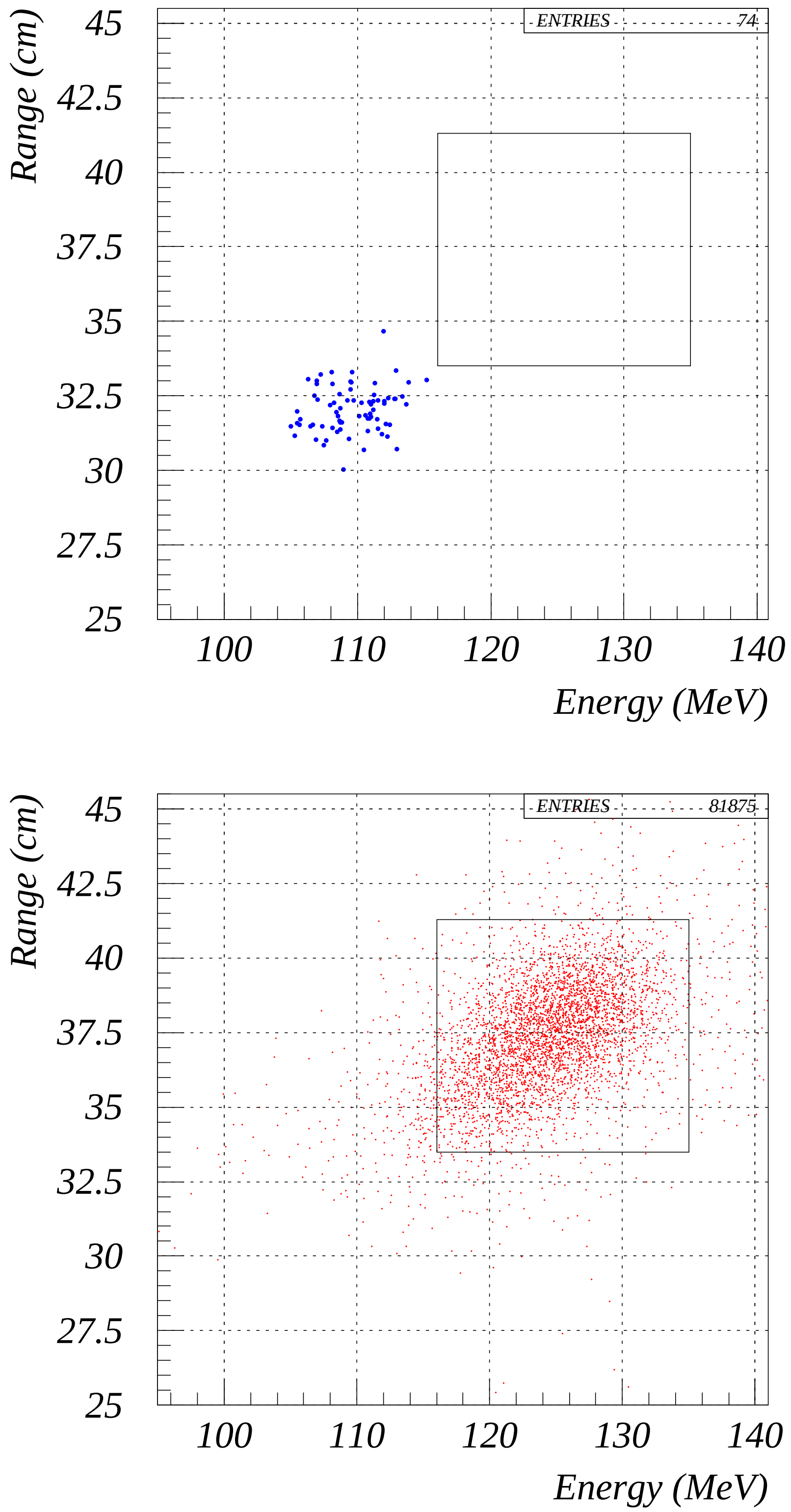

Figure 5.1: Range-energy plot of real data after imposing all of the cuts, except for the $K^+ \to \pi^+\gamma\gamma$ range and energy cuts (top); range-energy plot of Monte Carlo $K^+ \to \pi^+\gamma\gamma$ events (bottom).

Cut	Events
Sample	10716016
π^+ Reconstruction Cuts	8901805
Beam and Target Cuts	2789188
Kinematic Cuts	312917
$\pi^+ \to \mu^+ \to e^+$ Requirements	193253
γ Related Cuts	8704
$\pi^+\gamma\gamma$ Momentum	74
$\pi^+\gamma\gamma$ Range and Energy	0
$N_{\pi\gamma\gamma}$	0

Table 5.1: Number of events after imposing the offline cuts to the $K^+ \to \pi^+\gamma\gamma$ trigger.

5.2 Acceptance Factors

In order to obtain the single-event sensitivity for $K^+ \to \pi^+\gamma\gamma$, the acceptance factors of both the online and offline cuts should be measured. Real data are used as much as possible in the acceptance calculations. A number of acceptance factors are measured with the $K_{\mu 2}$, $K_{\pi 2}$ and π_{scat} monitor data. A Monte-Carlo simulation is used for the acceptance factors whose estimation is impossible with the real data; the trigger acceptance, the acceptance of the π^+ fiducial cuts and the π^+ stop efficiency in the Range Stack are measured with the Monte-Carlo simulation. The π^+ stop efficiency accounts for the acceptance loss due to π^+ nuclear interactions or decay-in-flights in the Range Stack. These acceptances totally depend on the kinematics of π^+ in $K^+ \to \pi^+\gamma\gamma$, and can not be measured with any monitor data. In addition, a part of the γ reconstruction and fiducial cuts and extra photon veto cuts, which are also related to the kinematics of photons in $K^+ \to \pi^+\gamma\gamma$, are measured with the Monte-Carlo simulation. The $K^+ \to \pi^+\gamma\gamma$ events are generated by assuming the ChPT with the $O(p^6)$ correction and $\hat{c} = 1.8$ for the Monte Carlo-based acceptance study. In addition, the $K^+ \to \pi^+\gamma\gamma$ events are generated by assuming the ChPT with $O(p^4)$ and $\hat{c} = 1.6$ and by assuming the phase-space distribution in order to compare to the previous results. Note that the Monte Carlo events whose π^+ momentum is larger than 200 MeV/c are generated for a speed-up.[2] The π^+ reconstruction efficiency and the acceptances of the beam and Target analysis are measured with the $K_{\mu 2}$ monitor data. The accidental losses due to the extra photon cuts are also measured with the $K_{\mu 2}$ monitor data, since the $K_{\mu 2}$ decay does not accompany particles other than the charged track. A part of the acceptance of the Target analysis, which is related to a π^+ track, is measured with the $K_{\pi 2}$ monitor data in order to take into account the hadronic interactions of π^+. In addition, the acceptance of the timing cut on the reconstructed photon cluster is measured with the photons from the $K_{\pi 2}$ monitor data. The acceptance of the $\pi^+ \to \mu^+ \to e^+$ decay chain requirements and the kinematic

[2] The lower edges of the $K^+ \to \pi^+\gamma\gamma$ kinematic cuts are much larger than those corresponding to the π^+ with 200 MeV/c.

cuts, except for the $K^+ \to \pi^+\gamma\gamma$ momentum, range and energy cuts, are measured with the π_{scat} monitor data. The $T \bullet 2$ efficiency, which accounts for the trigger inefficiency of the $T \bullet 2$ and I-counter, is measured with the K_B monitor data, which does not contain the $T \bullet 2$ requirement in the trigger. Since the energy deposits in the scintillator are different for $K_{\pi 2}$ and $K_{\mu 2}$, the $T \bullet 2$ efficiency is measured for each; the $T \bullet 2$ efficiency for the $K^+ \to \pi^+\gamma\gamma$ is obtained by interpolating the efficiencies from the $K_{\pi 2}$ and $K_{\mu 2}$ decays reconstructed with the same K_B trigger.

The acceptance factors, $A_i^{\pi^+\gamma\gamma}$, for each component i are listed in Table 5.2(ChPT $O(p^6)$), Table 5.3(ChPT $O(p^4)$) and Table 5.4(Phase Space), together with the monitor data type used in the calculation. In summary, the total acceptance for the $K^+ \to \pi^+\gamma\gamma(A^{\pi^+\gamma\gamma})$ is obtained by multiplying all the acceptance factor $A_i^{\pi^+\gamma\gamma}$ and

$$\begin{aligned} A^{\pi^+\gamma\gamma} &= \prod_i A_i^{\pi^+\gamma\gamma} \\ &= (1.550 \pm 0.034) \times 10^{-4} \quad (\text{for ChPT } O(p^6)), \\ &= (1.655 \pm 0.060) \times 10^{-5} \quad (\text{for ChPT } O(p^4)), \\ &= (1.533 \pm 0.036) \times 10^{-4} \quad (\text{for Phase Space}). \end{aligned} \tag{5.1}$$

Details of the acceptance measurements are described in Appendix C.

Definition	Symbol	Acceptance	Data
Trigger	$A^{\pi^+\gamma\gamma}_{\text{Trigger}}$	0.03455 ± 0.00008	Monte Carlo
π^+ Reconstruction Efficiency	$A^{\pi^+\gamma\gamma}_{\text{Reconstruction}}$	0.99556 ± 0.00012	$K_{\mu 2}$
π^+ Fiducial Cuts	$A^{\pi^+\gamma\gamma}_{\text{Fiducial}}$	0.89802 ± 0.00073	Monte Carlo
π^+ Stop Efficiency	$A^{\pi^+\gamma\gamma}_{\pi^+\text{StopEff.}}$	0.49226 ± 0.00215	Monte Carlo
$\pi^+ \to \mu^+ \to e^+$ Decay Chain	$A^{\pi^+\gamma\gamma}_{\pi^+\to\mu^+\to e^+}$	0.34872 ± 0.00548	π_{scat}
γ Reconstruction and Fiducial	$A^{\pi^+\gamma\gamma}_{\gamma\text{Recon.\&Fid.}}$	0.53047 ± 0.00204	Monte Carlo, $K_{\pi 2}$
Extra Photon Veto Cuts	$A^{\pi^+\gamma\gamma}_{\text{ExtraPV}}$	0.21633 ± 0.00185	Monte Carlo, $K_{\mu 2}$
Kinematic Cuts	$A^{\pi^+\gamma\gamma}_{\text{Kinematics}}$	0.53706 ± 0.00613	$K_{\pi 2}$, π_{scat}
Beam and Target	$A^{\pi^+\gamma\gamma}_{\text{Beam\&Target}}$	0.50697 ± 0.00077	$K_{\mu 2}$
$T \bullet 2$ Efficiency($\pi^+\gamma\gamma$)	$A^{\pi^+\gamma\gamma}_{T\bullet 2\text{Eff.}}$	0.93570 ± 0.00110	K_B
Total Acceptance	$A^{\pi^+\gamma\gamma} = 1.550 \pm 0.034 \times 10^{-4}$		

Table 5.2: Acceptance factors for $K^+ \to \pi^+\gamma\gamma$ (ChPT $O(p^6)$).

Definition	Symbol	Acceptance	Data
Trigger	$A^{\pi^+\gamma\gamma}_{\text{Trigger}}$	0.00609 ± 0.00003	Monte Carlo
π^+ Reconstruction Efficiency	$A^{\pi^+\gamma\gamma}_{\text{Reconstruction}}$	0.99556 ± 0.00012	$K_{\mu 2}$
π^+ Fiducial Cuts	$A^{\pi^+\gamma\gamma}_{\text{Fiducial}}$	0.62606 ± 0.00279	Monte Carlo
π^+ Stop Efficiency	$A^{\pi^+\gamma\gamma}_{\pi^+\text{StopEff.}}$	0.57773 ± 0.00692	Monte Carlo
$\pi^+ \to \mu^+ \to e^+$ Decay Chain	$A^{\pi^+\gamma\gamma}_{\pi^+\to\mu^+\to e^+}$	0.34872 ± 0.00548	π_{scat}
γ Reconstruction and Fiducial	$A^{\pi^+\gamma\gamma}_{\gamma\text{Recon.\&Fid.}}$	0.49166 ± 0.00471	Monte Carlo, $K_{\pi 2}$
Extra Photon Veto Cuts	$A^{\pi^+\gamma\gamma}_{\text{ExtraPV}}$	0.17271 ± 0.00434	Monte Carlo, $K_{\mu 2}$
Kinematic Cuts	$A^{\pi^+\gamma\gamma}_{\text{Kinematics}}$	0.53706 ± 0.00613	$K_{\pi 2}$, π_{scat}
Beam and Target	$A^{\pi^+\gamma\gamma}_{\text{Beam\&Target}}$	0.50697 ± 0.00077	$K_{\mu 2}$
$T \bullet 2$ Efficiency($\pi^+\gamma\gamma$)	$A^{\pi^+\gamma\gamma}_{T\bullet 2\text{Eff.}}$	0.93570 ± 0.00110	K_B
Total Acceptance	$A^{\pi^+\gamma\gamma} = 1.655 \pm 0.060 \times 10^{-5}$		

Table 5.3: Acceptance factors for $K^+ \to \pi^+\gamma\gamma$ (ChPT $O(p^4)$).

Definition	Symbol	Acceptance	Data
Trigger	$A^{\pi^+\gamma\gamma}_{\text{Trigger}}$	0.03490 ± 0.00010	Monte Carlo
π^+ Reconstruction Efficiency	$A^{\pi^+\gamma\gamma}_{\text{Reconstruction}}$	0.99556 ± 0.00012	$K_{\mu 2}$
π^+ Fiducial Cuts	$A^{\pi^+\gamma\gamma}_{\text{Fiducial}}$	0.89701 ± 0.00092	Monte Carlo
π^+ Stop Efficiency	$A^{\pi^+\gamma\gamma}_{\pi^+\text{StopEff.}}$	0.49796 ± 0.00273	Monte Carlo
$\pi^+ \to \mu^+ \to e^+$ Decay Chain	$A^{\pi^+\gamma\gamma}_{\pi^+\to\mu^+\to e^+}$	0.34872 ± 0.00548	π_{scat}
γ Reconstruction and Fiducial	$A^{\pi^+\gamma\gamma}_{\gamma\text{Recon.\&Fid.}}$	0.53584 ± 0.00242	Monte Carlo, $K_{\pi 2}$
Extra Photon Veto Cuts	$A^{\pi^+\gamma\gamma}_{\text{ExtraPV}}$	0.20751 ± 0.00220	Monte Carlo, $K_{\mu 2}$
Kinematic Cuts	$A^{\pi^+\gamma\gamma}_{\text{Kinematics}}$	0.53706 ± 0.00613	$K_{\pi 2}$, π_{scat}
Beam and Target	$A^{\pi^+\gamma\gamma}_{\text{Beam\&Target}}$	0.50697 ± 0.00077	$K_{\mu 2}$
$T \bullet 2$ Efficiency($\pi^+\gamma\gamma$)	$A^{\pi^+\gamma\gamma}_{T\bullet 2\text{Eff.}}$	0.93570 ± 0.00110	K_B
Total Acceptance	$A^{\pi^+\gamma\gamma} = 1.533 \pm 0.036 \times 10^{-4}$		

Table 5.4: Acceptance factors for $K^+ \to \pi^+\gamma\gamma$ (Phase Space).

5.3 K^+ Stop Efficiency

The acceptance due to the K^+ stop efficiency (f_s) in the Target has to be considered in order to calculate the single event sensitivity with the number of K^+ decays in the Target. The K^+ stop efficiency is a fraction of the number of K^+s that enter the Target and the number of K^+s that actually come to rest in it. In order to measure the efficiency, the $K_{\pi 2}$ decays in the $K^+ \to \pi^+\gamma\gamma$ trigger are used. The $K_{\pi 2}$ branching ratio ($BR(K_{\pi 2})$) is expressed as

$$BR(K_{\pi 2}) = \frac{N_{K_{\pi 2}}}{K_B^{\pi^+\gamma\gamma} \cdot f_s \cdot \prod_i A_i^{K_{\pi 2}}}, \tag{5.2}$$

where

$N_{K_{\pi 2}}$,	number of $K_{\pi 2}$ decays at rest in the $K^+ \to \pi^+\gamma\gamma$ trigger;
$K_B^{\pi^+\gamma\gamma}$,	number of K^+s that enter the Target, and;
$A_i^{K_{\pi 2}}$,	acceptance factors for selecting the $K_{\pi 2}$ decays.

$N_{K_{\pi 2}}$ is counted after imposing the selection cuts listed in the Table5.5 to the $K^+ \to \pi^+\gamma\gamma$ trigger, and

$$N_{K_{\pi 2}} = 212709$$

is obtained. $K_B^{\pi^+\gamma\gamma}$ was counted for the period that the $K^+ \to \pi^+\gamma\gamma$ trigger was active in the E949 run in 2002, and is

$$K_B^{\pi^+\gamma\gamma} = 1.192 \times 10^{12}. \tag{5.3}$$

The acceptance factors for the selection cuts ($A_i^{K_{\pi 2}}$) are listed in the Table5.6 together with $N_{K_{\pi 2}}$ and $K_B^{\pi^+\gamma\gamma}$. The trigger acceptance and the acceptance of the fiducial cuts are measured with the Monte-Carlo simulation. The $K_{\pi 2}$ decays with the $K^+ \to \pi^+\gamma\gamma$ trigger conditions are generated for this purpose. Other acceptance factors are measured with monitor data. By multiplying all of the acceptance factors, the total acceptance of the selection cut ($A^{K_{\pi 2}}$) is obtained to be

$$\begin{aligned} A^{K_{\pi 2}} &= \prod_i A_i^{K_{\pi 2}} \\ &= (1.1200 \pm 0.0351) \times 10^{-6}. \end{aligned}$$

By solving Eqn.5.2 and using the above numbers, the K^+ stop efficiency (f_s) is found to be

$$\begin{aligned} f_s &= \frac{N_{K_{\pi 2}}}{K_B^{\pi^+\gamma\gamma} \cdot \prod_i A_i^{K_{\pi 2}}} \times \frac{1}{BR(K_{\pi 2})} \\ &= 0.7541 \pm 0.0242, \end{aligned} \tag{5.4}$$

where the Particle Data Group value of 0.2113 ± 0.0014 [30] is used for the $BR(K_{\pi 2})$.

Cut	Events
Sample	10707691
π^+ Reconstruction Cuts	3746863
Beam and Target Cuts	1089144
π^+ Fiducial Cuts	423711
$\pi^+ \to \mu^+ \to e^+$ Requirements	333015
γ Fiducial Cuts	212709
Stopped $K_{\pi 2}$ Decays	212709

Table 5.5: Number of events after imposing the selection cuts in the K^+ stop efficiency measurement.

Definition	Symbol	Acceptance
Trigger	$A^{K_{\pi 2}}_{\mathrm{Trigger}}$	$0.48090 \pm 0.00310 \times 10^{-4}$
π^+ Reconstruction Cuts	$A^{K_{\pi 2}}_{\mathrm{Reconstruction}}$	0.79409 ± 0.00078
Beam and Target	$A^{K_{\pi 2}}_{\mathrm{Beam\&Target}}$	0.46627 ± 0.00102
π^+ Fiducial Cuts	$A^{K_{\pi 2}}_{\mathrm{Fiducial}}$	0.13127 ± 0.00229
$\pi^+ \to \mu^+ \to e^+$ Requirements	$A^{K_{\pi 2}}_{\pi^+ \to \mu^+ \to e^+}$	0.35269 ± 0.00842
γ Fiducial Cuts	$A^{K_{\pi 2}}_{\mathrm{Fiducial}}$	0.14418 ± 0.00105
$T \bullet 2$ Efficiency($K_{\pi 2}$)	$A^{K_{\pi 2}}_{T \bullet 2}$	0.93910 ± 0.00280
Total Acceptance	$A^{K_{\pi 2}} = 1.1200 \pm 0.0351 \times 10^{-6}$	
Stopped $K_{\pi 2}$ Decays	$N_{K_{\pi 2}}$	212709
K^+ Beam	$K_B^{\pi^+ \gamma\gamma}$	1.192×10^{12}
$K_{\pi 2}$ Branching Ratio	$BR(K_{\pi 2})$	0.21130 ± 0.00140
K^+ Stop Efficiency	$f_s = 0.7541 \pm 0.0242$	

Table 5.6: Numbers used in the K^+ stop efficiency measurement.

5.4 $K_{\mu 2}$ Branching Ratio

In order to confirm the validity of the acceptance calculations, the $K_{\mu 2}$ branching ratio $BR(K_{\mu 2})$ is measured using the following formula

$$BR(K_{\mu 2}) = \frac{N_{K_{\mu 2}}}{K_B^{K_{\mu 2}} \cdot f_s \cdot \prod_i A_i^{K_{\mu 2}}}, \tag{5.5}$$

where

$N_{K_{\mu 2}}$,	number of $K_{\mu 2}$ decays at rest in the $K_{\mu 2}$ trigger;
$K_B^{K_{\mu 2}}$,	number of K^+s that enter the Target; and
$A_i^{K_{\mu 2}}$,	acceptance factors for selecting the $K_{\mu 2}$ decays.

The number of $K_{\mu 2}$ events was counted after imposing the selection cuts listed in Table 5.7 to the $K_{\mu 2}$ trigger and obtained to be

$$N_{K_{\mu 2}} = 252908.$$

$K_B^{K_{\mu 2}}$ was counted for the same period that the $K^+ \to \pi^+ \gamma\gamma$ trigger was active. The online prescale factor of the $K_{\mu 2}$ trigger should be taken into account, and the $K_B^{K_{\mu 2}}$ is

$$K_B^{K_{\mu 2}} = 2910156.$$

The acceptance factors of the selection cuts are listed in Table 5.8. The trigger acceptance and the acceptance of fiducial cuts are measured with the Monte-Carlo simulation. The $K_{\mu 2}$ decays with the $K_{\mu 2}$ trigger are generated for this purpose. Other acceptance factors are measured with monitor data. By multiplying all of the acceptance factors, the total acceptance of the selection cut ($A^{K_{\mu 2}}$) is obtained to be

$$\begin{aligned} A^{K_{\mu 2}} &= \prod_i A_i^{K_{\mu 2}} \\ &= 0.18346 \pm 0.00049. \end{aligned}$$

By using Eqn. 5.5 and the above numbers, the $BR(K_{\mu 2})$ is calculated to be

$$BR(K_{\mu 2}) = 0.6282 \pm 0.0203,$$

which is consistent with the Particle Data Group value of 0.6343 ± 0.0017.

Cut	Events
Sample	761777
Reconstruction Cuts	561951
Beam and Target Cuts	278022
Photon Veto Cuts	254233
Fiducial Cuts	252908
Stopped $K_{\mu2}$ Decays	252908

Table 5.7: Numbers of events after imposing the selection cuts in the $K_{\mu2}$ branching-ratio measurement.

Definition	Symbol	Acceptance
Trigger	$A^{K_{\mu2}}_{\mathrm{Trigger}}$	0.44244 ± 0.00050
Reconstruction Cuts	$A^{K_{\mu2}}_{\mathrm{Reconstruction}}$	0.84678 ± 0.00062
Beam and Target	$A^{K_{\mu2}}_{\mathrm{Beam\&Target}}$	0.55984 ± 0.00076
Fiducial Cuts	$A^{K_{\mu2}}_{\mathrm{Fiducial}}$	0.98394 ± 0.00020
Photon Veto Cuts	$A^{K_{\mu2}}_{\mathrm{PV}}$	0.95556 ± 0.00127
$T \bullet 2$ Efficiency($K_{\mu2}$)	$A^{K_{\mu2}}_{T\bullet2}$	0.93030 ± 0.00120
Total Acceptance	$A^{K_{\mu2}} = 0.18346 \pm 0.00049$	
Stopped $K_{\mu2}$ Decays	$N_{K_{\mu2}}$	252908
K^+ Beam	$K_B^{K_{\mu2}}$	2910156
K^+ Stop Efficiency	f_s	0.75406 ± 0.02421
$K_{\mu2}$ Branching Ratio	$BR(K_{\mu2}) = 0.6282 \pm 0.0203$	

Table 5.8: Numbers used in the $K_{\mu2}$ branching-ratio measurement.

5.5 Branching Ratio for the $K^+ \to \pi^+\gamma\gamma$

By using Eqn. 5.1, Eqn. 5.3 and Eqn. 5.4, the single-event sensitivity (SES) for the $K^+ \to \pi^+\gamma\gamma$ is calculated as

$$
\begin{aligned}
SES(K^+ \to \pi^+\gamma\gamma, P_{\pi^+} > 200\mathrm{MeV/c}) &= \frac{1}{K_B^{\pi^+\gamma\gamma} \cdot f_s \cdot \prod_i A_i^{\pi^+\gamma\gamma}} \\
&= 7.18 \times 10^{-9} \quad (\text{for ChPT } O(p^6)), \\
&= 6.72 \times 10^{-8} \quad (\text{for ChPT } O(p^4)), \\
&= 7.26 \times 10^{-9} \quad (\text{for Phase Space}).
\end{aligned}
$$

Assuming the ChPT $O(p^6)$ is correct, the sensitivity is below the prediction (1.18×10^{-8}) and 1.6 events are expected to be observed in this sample. Since there is no event in the search region, by taking $N_{\pi^+\gamma\gamma} = 2.44$ instead of zero according to the unified approach [31], a 90% upper limit for the $K^+ \to \pi^+\gamma\gamma$ branching ratio in the π^+ momentum region of P_{π^+} >213 MeV/c is set to be

$$
\begin{aligned}
BR(K^+ \to \pi^+\gamma\gamma, P_{\pi^+} > 213\mathrm{MeV/c}) &< 9.08 \times 10^{-9} \quad (90\% \text{ C.L. for ChPT } O(p^6)), \\
&< 2.29 \times 10^{-8} \quad (90\% \text{ C.L. for ChPT } O(p^4)), \\
&< 9.90 \times 10^{-9} \quad (90\% \text{ C.L. for Phase Space}).
\end{aligned}
$$

Since only events whose π^+ momentum is larger than 200 MeV/c are generated in acceptance measurements with the Monte Carlo simulation, each spectrum shape is assumed in order to convert the upper limits for the region P_{π^+} >200 MeV/c to the limits for P_{π^+} >213 MeV/c. The factors are 0.5185, 0.1399 and 0.5523 for the ChPT $O(p^6)$, ChPT $O(p^4)$ and Phase Space, respectively The obtained upper limits for both the ChPT $O(p^6)$ and ChPT $O(p^4)$ are consistent with their predictions: 6.10×10^{-9} and 4.90×10^{-10} for P_{π^+} >213 MeV/c, respectively. The results from this analysis, unfortunately, cannot tell which of the ChPT with $O(p^6)$ corrections and the ChPT at $O(p^4)$ is favored. However, the following improvements have been achieved and should be emphasized. These limits are the tightest ones that have been experimentally achieved on the $K^+ \to \pi^+\gamma\gamma$ (P_{π^+} >213 MeV/c). This analysis, which is limited by the statistics of kaon decays in the E949-2002 data taking, has proved that the E949 hardware and software are suitable to study the $K^+ \to \pi^+\gamma\gamma$ decay in this kinematic region with negligible background. E949 is assumed to run for 60 weeks in total, and would surely be able to observe a few signal events if the ChPT with $O(p^6)$ corrections is correct. In order to compare to the previous result, the 90% upper limit for the full spectrum is set to be

$$\begin{aligned} BR(K^+ \to \pi^+\gamma\gamma) &< 1.57 \times 10^{-6} \quad (90\% \text{ C.L. for ChPT } O(p^6)), \\ &< 4.46 \times 10^{-5} \quad (90\% \text{ C.L. for ChPT } O(p^4)), \\ &< 6.58 \times 10^{-8} \quad (90\% \text{ C.L. for Phase Space}). \end{aligned}$$

The upper limit for the Phase Space distribution is 7.6-times better than that in the previous result [6].

5.6 Branching Ratio for the $K^+ \to \pi^+\gamma$

The upper limit for $K^+ \to \pi^+\gamma$ is also set from this analysis. This decay is a spin $0 \to 0$ transition with a real photon, and is thus forbidden by angular-momentum conservation. Current interest in this decay is to search for exotic new physics, such as non-commutative QED [32]. The current upper limit of 3.6 $\times 10^{-7}$ at 90% C.L was set by E787 [33]. The signature of $K^+ \to \pi^+\gamma$ in the experiment is a two-body decay of kaon at rest with a 227 MeV/c π^+ track in the Range Stack and a 227 MeV photon emitted directly opposite to it and observed in the Barrel Veto Liner and the Barrel Veto.

The acceptance factors were measured in the same way as the $K^+ \to \pi^+\gamma\gamma$, and are listed in Table 5.9. Monte Carlo $K^+ \to \pi^+\gamma$ events with the $K^+ \to \pi^+\gamma\gamma$ trigger conditions are generated for this purpose. The upper limit for $K^+ \to \pi^+\gamma$ is obtained to be

$$\begin{aligned} BR(K^+ \to \pi^+\gamma) &= \frac{N_{\pi^+\gamma}}{N_{K_B}^{\pi^+\gamma} \cdot f_s \cdot \prod_i A_{\pi^+\gamma}} \\ &< 2.50 \times 10^{-9} \quad (90\% \ \text{C.L.}). \end{aligned}$$

The upper limit is 144-times better than that in the previous result.

Definition	Symbol	Acceptance	Data
Trigger	$A^{\pi^+\gamma}_{\text{Trigger}}$	0.12491 ± 0.00021	Monte Carlo
π^+ Reconstruction Efficiency	$A^{\pi^+\gamma}_{\text{Reconstruction}}$	0.99556 ± 0.00012	$K_{\mu 2}$
π^+ Fiducial Cuts	$A^{\pi^+\gamma}_{\text{Fiducial}}$	0.94162 ± 0.00042	Monte Carlo
π^+ Stop Efficiency	$A^{\pi^+\gamma}_{\pi^+\text{StopEff.}}$	0.45982 ± 0.00145	Monte Carlo
$\pi^+ \to \mu^+ \to e^+$ Decay Chain	$A^{\pi^+\gamma}_{\pi^+\to\mu^+\to e^+}$	0.34872 ± 0.00548	π_{scat}
γ Reconstruction and Fiducial	$A^{\pi^+\gamma}_{\gamma\text{Recon.\&Fid.}}$	0.67620 ± 0.00181	Monte Carlo, $K_{\pi 2}$
Extra Photon Veto Cuts	$A^{\pi^+\gamma}_{\text{ExtraPV}}$	0.33525 ± 0.00169	Monte Carlo, $K_{\mu 2}$
Kinematic Cuts	$A^{\pi^+\gamma}_{\text{Kinematics}}$	0.53706 ± 0.00613	$K_{\pi 2}$, π_{scat}
Beam and Target	$A^{\pi^+\gamma}_{\text{Beam\&Target}}$	0.50697 ± 0.00077	$K_{\mu 2}$
$T \bullet 2$ Efficiency($\pi^+\gamma$)	$A^{\pi^+\gamma}_{T\bullet 2\text{Eff.}}$	0.93570 ± 0.00110	K_B
Total Acceptance	$A^{\pi^+\gamma} = 0.0010844 \pm 0.0000224$		

Table 5.9: Acceptance factors for $K^+ \to \pi^+\gamma$.

Chapter 6

Conclusion

An experimental search for the $K^+ \to \pi^+\gamma\gamma$ decay in the momentum region $P_{\pi^+} > 213$ MeV/c was performed by using the data set collected by the BNL-E949 experiment in the year 2002. The motivation to study this decay mode is a test of the ChPT. The E949 collected 1.192 $\times 10^{12}$ K_B triggers and the sensitivity from the data set are within the prediction of ChPT with higher order corrections. In order to reliably estimate the background level, a special technique, called the "Bifurcation Method", is used. The background level to the search region is estimated to be (0.197 $\pm$ 0.070) events. No candidate event was found in the search region after imposing all of the selection criteria. The 90% Confidence Level upper limits for each of the ChPT with $O(p^6)$ corrections, the at ChPT $O(p^4)$ and the Phase Space distribution are set to be

$$\begin{aligned} BR(K^+ \to \pi^+\gamma\gamma, P_{\pi^+} > 213\text{MeV/c}) &< 9.08 \times 10^{-9} \quad (90\% \text{ C.L. for ChPT } O(p^6)), \\ &< 2.29 \times 10^{-8} \quad (90\% \text{ C.L. for ChPT } O(p^4)), \\ &< 9.90 \times 10^{-9} \quad (90\% \text{ C.L. for Phase Space}). \end{aligned}$$

The obtained upper limits for both the ChPT $O(p^6)$ and ChPT $O(p^4)$ are consistent with the predictions of 6.10 $\times 10^{-9}$ and 4.90 $\times 10^{-10}$, respectively. The upper limits for the full spectrum were also obtained in order to compare with the previous result; the upper limit for the phase space distribution is 7.6-times better than the previous limit.

The same analysis set the upper limit for $K^+ \to \pi^+\gamma$:

$$BR(K^+ \to \pi^+\gamma) < 2.50 \times 10^{-9} \quad (90\% \text{ C.L.}),$$

which is 144-times better than the previous limit.

Acknowledgments

First of all, I would like to express my deep gratitude to my supervisor Prof. S. Sugimoto, who gave me an opportunity to work in the E949 collaboration and greatly encouraged my research with useful advice.

I am very thankful to Prof. T. Komatsubara, who always supported me with many suggestions throughout this research. There is no doubt that this thesis could not be finished without his kindful helps.

I am deeply grateful to Prof. M. Nomachi, who taught me many things to be an experimental particle physicist. Working with him was really exciting for me, and I hope to work with him again someday.

I am greatly indebted to Prof. T. Nakano, who has been promoting the studies of radiative kaon decays and Chiral Perturbation Theory in E787-E949 and originally proposed to do this study. He provided me with much useful advice, in particular on the theoretical issues.

I would like to express my great appreciation to Dr. J. Frank, Dr. D. Jaffe, Dr. S. Kettell, Dr. L. Littenberg and Dr. G. Redlinger of BNL, and Prof. D. Bryman, Dr. S. Chen, Dr. J. Hu, Dr. A. Konaka and Dr. J. Mildenberger of TRIUMF and all the members of the E949 collaboration in Japan, Canada, Russia and the United States for useful discussions.

I would like to express my special appreciation to Mr. K. Mizouchi and Mr. T. Sekiguchi for their support and friendship that I received.

Finally, I would like to thank my grandparents and parents for their supports.

This research was supported by the Japan-U.S. Cooperative Research Program in High Energy Physics and the Grant-in-Aid for Scientific Research on Priority Areas “Origin of Mass”.

Appendix A

Lists of Selection Criteria

All the cuts used in this analysis are listed and explained in this appendix. They are classified into five categories (or "cut packages"): Reconstruction Cuts, Kinematic Cuts, Photon Cuts, Beam Cuts and Transient Digitizer Cuts.

A.1 Reconstruction Cuts : PASS1CUT

- **Trigger Bit (TRBIT)**
  The online bit for the $K^+ \to \pi^+\gamma\gamma$ trigger is requested.

- **Range-Stack Track Reconstruction (RDTRK)**
  At least one positively-charged track is reconstructed successfully in the Range Stack.

- **Stopping Layer Consistency (STLAY)**
  The online stopping counter and hextant[1] of the charged track agree with those from the offline analysis.

- **Cut on the Range-Stack Accidental Hits (RSHEX)**
  This cut looks for any extra activity in the Range Stack counters which are in the same hextant and in the same layer as the stopping layer. Signals from these four counters are multiplexed and fed into the same TD channel; an extra activity could screw up the π^+ identification in the TDs.

- **Track Time Reconstruction (TRKTIM)**
  A track time in the Range Stack is reconstructed successfully.

- **Drift Chamber Reconstruction (UTC)**
  At least one charged-track is reconstructed successfully in the Drift Chamber in both the x-y and r-z track fittings.

[1] The Range Stack counters are grouped into six regions, each of which contains four adjacent sectors. These regions are called "hextants" and are used for the online Range Stack photon veto logic.

- **Matching between the Drift-Chamber and Range-Stack Tracks (UTC/RANGE)**
  The track reconstructed in the Drift Chamber matches the positions of the Range Stack hits.

- **Cut on the Sector Crossing in the Stopping Counter (RSHEX2)**
  Events with a sector crossing[2] in the stopping layer are rejected due to the possible screwed-up in the TD analysis.

A.2 Kinematic Cuts : KINCUT

- **Fiducial Cuts on Charge Track (FIDUCIAL)**

  - **Polar Angle (COS3D)**
    Events with a charged track whose cosine of the polar angle θ with respect to the beam direction (z axis) is greater than 0.5 or less than -0.5 are rejected; this cut requests $60^\circ < \theta < 120^\circ$ as the fiducial region of π^+.
  - **Offline Stopping Layer (LAY1617)**
    The offline stopping layer should be 16 or 17 as requested in the trigger.
  - **Z-Position in the Range Stack (ZFRF)**
    The fiducial region in the Range Stack stopping layer in the beam direction is defined as $|z| < 50.0$cm. The z position is measured from the Drift-Chamber track extrapolation in the r-z view.
  - **Z-Position in the Drift Chamber (ZUTOUT)**
    A charged track passes through the region $|z| < 25$cm at the outermost radius of the Drift Chamber.

- **Quality Cut on the Drift-Chamber Track Fitting (UTCQUAL)**
  The confidence level of the track fitting in the Drift Chamber is calculated, and the events with the confidence level less than 10^{-5} are rejected.

- **Range Stack dE/dx Cuts (RSDEDX)**
  The cuts on the dE/dx in the Range Stack counters consist of three cuts based on the measured energy deposits ($E_{meas.}$) and the expected energy deposits from the measured range ($E_{expt.}$) in the Range Stack counters. The χ_{RSDEDX} is defined as

  $$\chi_{RSDEDX} \equiv \frac{\Delta \log(E)}{\sigma_E}$$

  where the $\Delta \log(E)$ is an expression of the residual of the measured and expected energies:

  $$\Delta \log(E) \equiv \log(E_{expt.}) - \log(E_{meas.}).$$

  The σ_E has been obtained for each layer as a function of the stopping layer of the charged track. The confidence level is computed by summing the χ^2_{RSDEDX}

[2]The "sector crossing" is explained in section 3.2.1.

for all the track counters except for the T-counter, sector crossing counters and the stopping counter, and the cut position is set to be $\geq$ 2%. The maximum value among the χ_{RSDEDX} measurements (χ^{MAX}_{RSDEDX}) also rejects the background efficiently; it is required that $|\chi^{MAX}_{RSDEDX}| \leq 4$. A likelihood formed by the $\Delta \log(E)$ also discriminates the signal from background. The cut position is set to be 10.0.

- **Range-Momentum Relation (RNGMOM)**
  Events with $\chi_{RP} \equiv (R_{meas.} - R_{expt.})/\sigma_R > 2.2$ is rejected, where the $R_{meas.}$ is the measured range in the Range Stack, $R_{expt.}$ is the expected range in the Range Stack from the momentum measured by the Drift Chamber, and the σ_R is the standard deviation of the range distribution at the measured momentum.

- **Quality Cuts on the Range-Stack Track Fitting (PRRF)**
  The confidence level of the track fitting in the Range Stack is calculated based on the position of sector crossing, RSSCs hit positions, and the energy deposit in the stopping layer. Events with the confidence level <0.05 are rejected. Other confidence levels in both the x-y plane and r-z plane, by using the extrapolation of the Drift Chamber track, are calculated, and the events with the confidence level <0.05 and <0.005 for xy-plane and r-z plane, respectively, are rejected.

- **Target dE/dx Cuts (TGDEDX)**
  The dE/dx of a charged track in the Target is required to be consistent with that expected for π^+ tracks; events with too long range in the Target (>12 cm), too large energy in pion fibers (>28 MeV) and the events which do not satisfy a correlation between the energy and the range in the Target are rejected.

- **Likelihood Cuts in the Target Reconstruction (TGLIKE)**
  A likelihood is reconstructed by using the time, the energy and the distance from the extrapolated Drift Chamber track (swath) of each pion fiber. Another likelihood is reconstructed by using only the distance from swath. Events with the likelihood values <3.2 and <2.3, respectively, are rejected.

- **Matching Between the Hit Positions in B4 and Target (TGB4)**
  Events are rejected if the x-y position of the B4 counter is far from the nearest kaon fiber in the Target (>2 cm) or from the extreme tip of the kaon fibers (>2 cm). In addition, events are removed when the decay vertex is far from the nearest pion fiber in the Target (>1.5 cm) or from the extreme tip of the kaon fibers (>0.7 cm).

- **Pion Gap Cut (PIGAP)**
  Events are rejected if there is a gap greater than 1.6 cm in the Target pion track.

- **Charged Track Kinematics (BOXCUT)**

  - **Box Cuts for $K^+ \to \pi^+\gamma\gamma$ (PGGBOX)**
    The search region is defined as

$$\begin{array}{ccccc} 213.3 \text{ MeV/c} & < & \text{Momentum} & < & 234.0 \text{ MeV/c} \\ 33.5 \text{ cm} & < & \text{Range} & < & 41.3 \text{ cm} \\ 116.0 \text{ MeV} & < & \text{Energy} & < & 135.0 \text{ MeV}. \end{array}$$

The cuts on the lower-side (213.3 MeV/c, 33.5 cm and 116 MeV) are determined by using the deviation from the $K_{\pi 2}$ peak, correspond to the following conditions.

$$\begin{array}{ccccc} \text{PDEV} & \equiv & \dfrac{P_{meas.} - P_{peak}^{K_{\pi 2}}}{\sigma_P^{K_{\pi 2}}} & \geq & 3.26 \\ \text{RDEV} & \equiv & \dfrac{R_{meas.} - R_{peak}^{K_{\pi 2}}}{\sigma_R^{K_{\pi 2}}} & \geq & 2.34 \\ \text{EDEV} & \equiv & \dfrac{E_{meas.} - E_{peak}^{K_{\pi 2}}}{\sigma_E^{K_{\pi 2}}} & \geq & 2.63, \end{array}$$

where the P_{peak}, R_{peak}, E_{peak} are the means and $\sigma_P^{K_{\pi 2}}$, $\sigma_R^{K_{\pi 2}}$ and $\sigma_E^{K_{\pi 2}}$ are the sigmas for the π^+ distributions from $K_{\pi 2}$, as listed in Table 3.1

– **Box Cuts for $K_{\pi 2}$ ($K_{\pi 2}$BOX)**
This cut is used to select and purify the $K_{\pi 2}$ events in the background study.

$$\begin{array}{ccccc} 195.0 \text{ MeV/c} & < & \text{Momentum} & < & 213.0 \text{ MeV/c} \\ 27.0 \text{ cm} & < & \text{Range} & < & 33.5 \text{ cm} \\ 95.0 \text{ MeV} & < & \text{Energy} & < & 115.0 \text{ MeV}. \end{array}$$

A.3 Photon Cuts : PTNCUT

- **Number of Photon Clusters (NREG)**
  The photon clusters whose energy is more than 6.7 MeV are reconstructed in the Barrel Veto Liner and Barrel Veto. The number of clusters must be one or two.

- **Fiducial Cuts on the Photon Cluster (BVCLS)**

  – **Energy of the Highest-Energy Clusters (EG1)**
  The energy of the highest-energy cluster (γ_1) should satisfy 50MeV $< E_{\gamma_1} <$ 320MeV.

  – **Energy of the 2nd Cluster (EG2)**
  The energy of the 2nd cluster (γ_2), if it exists, should be greater than 10MeV.

  – **Polar Angle (DIPANG)**
  $\cos\theta_{\gamma 1}$ and $\cos\theta_{\gamma 2}$ should be within ± 0.6, where θ_{γ_1} and θ_{γ_2} are the polar angles of γ_1 and γ_2, respectively.

- **Opening Angle in X-Y Plane (COSOPXY)**
  It is required that the azimuthal opening angle between the charged track and the highest-energy cluster is greater than 155°.
- **Opening Angle in R-Z Plane (COSOPZ)**
  It is required that the polar opening angle between the charged track and the highest-energy cluster is greater than 155°.
- **Time of the Photon Clusters (TG)**
  It is required that the timing of each cluster is within ±2.0 nsec with respect to the Range Stack track time.

- **Energy Ratio and Opening Angle Between Two Photons (COSGG)**
  If two photons γ_1 and γ_2 are reconstructed, a cut on the relation between the ratio of the energies ($E_{\gamma_1}/E_{\gamma_2}$) and their opening angle ($\cos\theta_{\gamma\gamma}$):

$$\frac{E_{\gamma 2}}{E_{\gamma 1}} = \frac{E_0 - \sqrt{E_0^2 - \frac{2M_{\gamma\gamma}^2}{1-\cos\theta_{\gamma\gamma}}}}{E_0 + \sqrt{E_0^2 - \frac{2M_{\gamma\gamma}^2}{1-\cos\theta_{\gamma\gamma}}}}$$

  where

$$E_0 \equiv \frac{M_{K^+}^2 - M_{\pi^+}^2 + M_{\gamma\gamma}^2}{2M_{K^+}},$$

  is imposed. The cut position is set to be $M_{\gamma\gamma} \geq 100$ MeV, where the $M_{\gamma\gamma}$ is the invariant mass of the two photons and is calculated from E_{γ_1}, E_{γ_2} and $\cos\theta_{\gamma\gamma}$. Remind that this cut is automatically satisfied if NREG=1 ($E_{\gamma_2} = 0.0$).

- **Cut on the Maximum Discrepancy Among Z Measurements (TZMAX)**
  Events are rejected if the maximum discrepancy among the TDC-based z-measurements (z_{disc}) in the highest-energy cluster is greater than 112.5 cm are rejected.

- **Photon Veto Cuts in Other Subsystems (PVCUT)**
  Any extra activity other than the charged track and the photons in the Barrel region should be detected and vetoed. The time window and energy threshold are set for each detector subsystem. In the Endcap photon-veto cut, the innermost ring of the upstream Endcap is taken care of separately because the crystals in it are located in the environment with higher accidental rates. The time window and energy threshold for the Endcap are listed in Table A.1. In the Range Stack photon-veto cut (RSPVCUT), the cut is tightened if the hits are recorded in TDCs but not recorded in ADCs of both ends. The time window and energy threshold for the Range Stack are listed in Table A.2. The time window and energy threshold for the Target photon fibers (TGPVCUT), I-counter, V-counter, Collar and Micro-Collar are listed in Table A.3.

Subsystems	Time Window (nsec)	Energy Threshold (MeV)
EC Except for the Innermost Ring in the Upstream	0.25±2.25	3.80
EC Innermost Ring in the Upstream	0.00±1.75	1.00

Table A.1: Time window and energy threshold for the Endcap photon-veto cut.

Subsystems	Time Window (nsec)	Energy Threshold (MeV)
Range Stack	-0.75±1.50	3.80
RS no ADC, both-end TDC	0.75±2.00	0.40

Table A.2: Time window and energy threshold for the Range Stack photon-veto cut.

Subsystems	Time Window (nsec)	Energy Threshold (MeV)
Target	0.10±1.30	4.79
I-counter	0.25±2.25	0.40
V-counter	-1.75±2.00	1.60
Collar	2.75±1.25	0.80
Micro-Collar	-0.50±1.50	2.80

Table A.3: Time window and energy threshold for the photon veto cuts of Target, I-counter, V-counter, Collar and Micro-Collar.

A.4 Beam Cuts : PSCUT

- **B4 Counter and Beam Wire Chambers (B4BW)**
  - **dE/dx in B4 Counter (B4DEDX)**
    The energy deposit in the B4 counter is required to be greater than 1.1 MeV, which discriminates a kaon from a pion in the beam.
  - **Timing on Beam Wire Chambers (BWTRS)**
    Events are rejected if there is a reconstructed hit in the beam wire chambers whose timing is close to the Range-Stack track time within ± 4.5 nsec.
  - **Timing on B4 Counter (B4TRS)**
    Events are rejected if there is a reconstructed hit in the B4 counter whose timing is close to the Range-Stack track time within ± 2.5 nsec.
  - **Consistency in the B4 Analysis (B4ETCON)**
    The values of the energy deposit in the B4 counter measured by ADCs and CCDs, respectively, are required to be consistent within ± 1.5MeV. The timings of the B4 counter measured by TDCs and CCDs, respectively, are also required to be consistent within ± 2.0 nsec.
  - **Timing on the 2nd Pulse in B4 Counter (B4CCD)**
    Single-pulse and double-pulse fits are performed to the CCD pulse shapes of the B4 counter. Events with a 2nd pulse whose timing is close to the Range-Stack track time within ± 3.5 nsec are rejected.

- **Čerenkov Counters (CERENKOV)**
  - **Timing on Kaon Čerenkov Counter (CKTRS)**
    Events are rejected if there is a reconstructed hit in the Kaon Čerenkov counter whose timing is close to the Range-Stack track time within ± 2.0 nsec.
  - **Timing on Kaon Čerenkov Counter Using the TDC Trailing Edge (CKTAIL)**
    This cut is the same as the CKTRS cut except that the trailing-edge of the TDC time is used to reconstruct the timing of the hit.
  - **Timing on Pion Čerenkov Counter (CPITRS)**
    Events are rejected if there is a reconstructed hit in the Pion Čerenkov counter whose timing is close to the Range-Stack track time within ± 2.0 nsec.
  - **Timing on Pion Čerenkov Counter Using the TDC Trailing Edge (CPITRS)**
    This cut is the same as the CPITRS cut except that the trailing-edge of the TDC time is used to reconstruct the timing of the hit.

- **Target Pattern Recognition and Quality (TGPATT)**
  - **Target Quality (TGQUALT)**
    It is required that the kaon and pion clusters are successfully reconstructed in

the Target analysis. Events with no pion fibers in the Target are accepted if there is an I counter hit near the kaon cluster.

- **Z Position in the Target (TGZFOOL)**
  The z position of the decay vertex in the Target, determined by the extrapolated Drift Chamber track, should be located at $z = -15$ cm or larger, which corresponds to the fiducial region of the Target.
- **Pion Fiber Energy (EPITG)**
  It is required that the energy deposit of any pion fiber in the Target should be less than 5 MeV. This cut avoids putting a hit with an extra activity into the pion energy in the Target.
- **Additional Pion-Fiber Energy Cut (EPIMAXK)**
  It is required that the pion fibers near the decay vertex should have the energy less than 3.5 MeV. This cut avoids putting a hit with an extra activity or an energy loss due to the kaon coming to rest into the pion energy in the Target.
- **Target Gap Cut (TARGF)**
  The distance between the kaon cluster and the pion cluster in the Target should be less than 0.7 cm.
- **Matching of the Charged Tracks in Target and in Drift Chamber (DTGTTP)**
  The distance between the pion fiber at the Target edge and the extrapolated Drift Chamber track to the Target should be less than 2 cm.
- **Errors in the Target Path-Length (RTDIF)**
  Errors in the calculation of a pion path length in the Target is required to be small.
- **Kink in the Target (DRP)**
  The difference of the maximum and minimum distances from the center of the curvature of the Drift Chamber track in the x-y view to the pion fibers in the Target is required to be small. The difference is normalized by the range in the Target, and the events with the value greater than 0.35 are rejected. This cut rejects the events with a charged decay product scattered in the Target.
- **Decay Vertex Cut (PHIVTX)**
  Events with back-to-back two tracks reconstructed in the Target are rejected.
- **Additional Decay-Vertex Cut (PHIVTX2)**
  Events with pion fibers on the opposite side of the decay vertex from the π^+ track in the Target are rejected.

• **Target Energy (ENERGY)**

  - **Beam Likelihood (B4EKZ)**
    A likelihood is formed by using the energy deposit in the B4 counter, the decay vertex position and the kaon energy in the Target. These three variables have correlations if they record the information of kaons coming to rest. The likelihood value is required to be greater than 2.0. If there is no pion cluster in the Target, the cut position is tightened to be greater than 12.5.

- **Consistency Between the Target Energy and Range (TGER)**
  Events which have small pion energy (<1 MeV) and have a long range (> 2 cm) in the Target are rejected.
- **Opposite Side Veto (OPSVETO)**
  The energies in the fibers on the opposite side of the decay vertex from the π^+ track are summed up. Events with the sum greater than 2.0 MeV are rejected. The energy threshold is lowered if the beam likelihood value is poor (<200.0).
- **Target Edge (TGEDGE)**
  Events which have an energy of more than 4 MeV in any edge fiber in the Target within ± 5.0 nsec of the Range-Stack track time are rejected.

• **Timing Cuts (TIMING)**

- **Timing Consistency (TIMCON)**
  The kaon time in the Target should be consistent with the B4 counter time within ± 3 nsec. The pion time in the Target should be consistent with the Range-Stack track time within ± 4 nsec.
- **Consistency of Kaon Fibers (TGTCON)**
  The time recorded in each kaon fiber should be consistent with the kaon time reconstructed in the Target.
- **I-counter Timing (TIC)**
  The I-counter time should be consistent with the Range-Stack track time within ± 5 nsec.

• **I-counter Energy (EIC)**
Consistency cuts between the energy deposit (eic) and that expected from the range ($eicest$) in the I-counter: events are rejected if $|eic - eicest| > 5\text{MeV}$ or $(eic - eicest) > 1.75\text{MeV}$.

• **Cuts on the Upstream Photon Veto and Ring Veto Counters (UPV/RPVTRS)**
Events with any activity at the Range-Stack track time in the upstream photon veto or in the ring veto counters are rejected.

• **Delayed Coincidence Cuts (DELC)**
It is required that $t_\pi - t_K > 2\text{nsec}$, where t_π and t_K are the pion and kaon times reconstructed in the Target, respectively. The cut position is tightened as follows, according to the quality of the timing reconstruction.

- $t_\pi - t_K > 5\text{nsec}$, if the kaon time in the Target is not consistent with the B4 counter time within ± 1.0 nsec.
- $t_\pi - t_K > 6\text{nsec}$, if the pion time in the Target is not consistent with the Range Stack time within ± 1.5 nsec.
- $t_\pi - t_K > 5\text{nsec}$, if there is no pion fiber in the Target and the I-counter time is used for t_π instead.
- $t_\pi - t_K > 4\text{nsec}$, if the kaon energy in the Target is less than 50 MeV.

- $t_\pi - t_K > 3$nsec, if the number of pion fibers in the Target is less than 4.
- $t_\pi - t_K > 3$nsec, if the beam likelihood value is less than 200.0.
- $t_\pi - t_K > 5$nsec, if any one of the kaon fibers has a time deviated from the average kaon time for more than 2.0 nsec.
- $t_\pi - t_K > 5$nsec, if any one of the pion fibers has a time deviated from the average pion time for more than 3.5 nsec.

- **Cut Against Kaons Stopped in the I-counter (KIC)**
  Events with an I-counter hit at the kaon time and the counter is located near the kaon cluster are rejected. This cut ensures that the kaon comes to rest in the Target, not in the I-counter.

- **TGGEO**
  This cut removes double-beam backgrounds by using the TD/TDC information of the I-counter. Events are rejected if:
  - two particles enter the Target near the target edge or two particles enter an I-counter at first and reach the Target,
  - the particle that comes at first or the decay product from the particle leaves large energies in the I-counter, or
  - the particle that comes at first enters the Target, decays to the downstream or decays very late and is not detected, and the particle that comes in the next is scattered in the upstream and then is missed by some beam counters.

A.5 Transient Digitizer Cuts : TDCUT

- **Observation of a $\pi^+ \to \mu^+$ (FITPI)**
  It is required that a $\pi^+ \to \mu^+$ decay chain is observed in the stopping counter by the double-pulse fit.

- **Timing Consistency (TDTCON)**
  It is required that the TD π^+ time in the stopping counter is consistent with the Range-Stack track time within ± 2.5 nsec.

- **Cut against Electron Time Accidental (EV5)**
  Events with an extra activity in the Range Stack at the e^+ time are rejected.

- **Cut against Muon Time Accidental (ELVETO)**
  Events with an extra activity at the μ^+ time are rejected. The time window and energy threshold, optimized for TD analysis, are set for each of the Range Stack, Barrel Veto Liner, Barrel Veto and Endcap in the same way as in the photon veto cuts.

- **Cut against Muon Time Accidental (TDFOOL)**
  Events with an extra activity in the track counters in the Range Stack at the μ^+ time are rejected.

- **Neural Network Cut (TDVAR)**
  A Neural Network function is formed by using five variables from TD; (1) the χ^2 of the single-pulse fit, (2) the χ^2 ratio of the single-pulse fit to the double-pulse fit, (3) μ^+ energy, (4) the time difference of μ^+ between both ends, and (5) the μ^+ time.

Appendix B

Details of Background Studies

B.1 $K_{\pi 2}$ Background Study

Fig. B.1 shows the bifurcation chart for the $K_{\pi 2}$ background study. A number of cuts to remove other backgrounds, called "setup cuts", are imposed before the bifurcation; the Reconstruction Cuts (PASS1CUT), Beam Cuts (PSCUT), Kinematic Cuts (KINCUT) except for BOXCUT, Transient Digitizer Cuts (TDCUT), and fiducial cuts for the photon cluster (BVCLS) are imposed to the $K^+ \to \pi^+\gamma\gamma$ triggers. Note that the Range Stack photon-veto cut (RSPVCUT) should also be imposed in the setup cuts because, based on the Monte Carlo studies, about 5% of the $K^+ \to \pi^+\gamma\gamma$ signal events would be tagged by RSPVCUT reversed in the normalization branch. The Target photon veto cut (TGPVCUT) are also applied in the setup cut for the same reason. The bifurcation is performed between Photon Cuts (PTNCUT) and box cuts on the charged track kinematics (BOXCUT). The normalization branch is further bifurcated (2nd bifurcation) in order to estimate the number of events in the normalization branch. In the normalization branch of the 2nd bifurcation, the events that failed a $K^+ \to \pi^+\gamma\gamma$ energy cut (EDEV) are tagged, and the number of events within the $K^+ \to \pi^+\gamma\gamma$ momentum and range cuts (RPBOX) are counted. The rejection factor of the EDEV cut is measured in the rejection branch of the 2nd bifurcation with the events that failed the RPBOX cuts. The $K_{\pi 2}$ background study is summarized in Table B.1 from both the 1/3 sample and the 2/3 sample, and each quantity is described as follows.

N_{RP}	:	Number of events in the normalization branch of the 2nd bifurcation.
R_E	:	Rejection factor for the EDEV cut in the 2nd bifurcation.
N_{Norm}	:	Number of events in the normalization branch obtained from the 2nd bifurcation.
N_{PTN}	:	Rejection factor of the photon cuts (PTNCUT).
$N_{K_{\pi 2}}$	:	Estimated $K_{\pi 2}$ background level.

$K_{\pi 2}$ Background Study

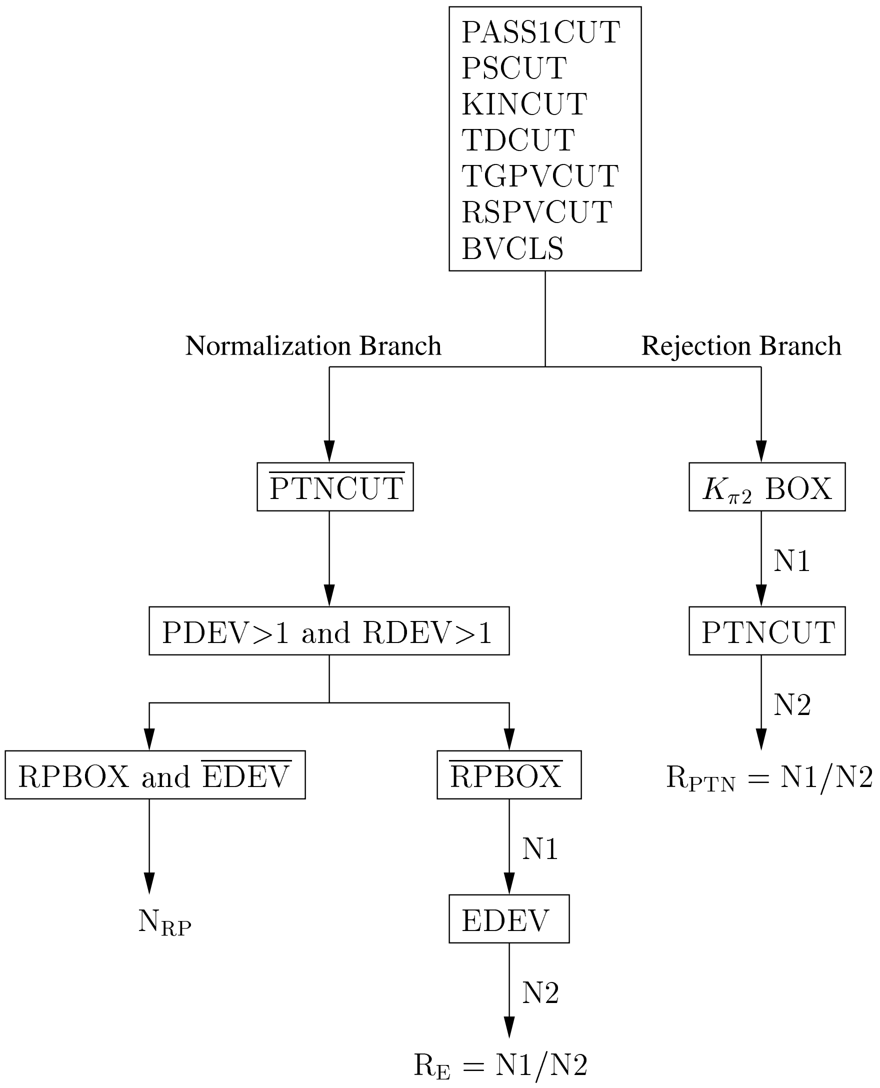

$$\mathrm{N_{norm}} = \frac{\mathrm{N_{RP}}}{\mathrm{R_E} - 1} \qquad \mathrm{N_{K_{\pi 2}}} = \frac{\mathrm{N_{norm}}}{\mathrm{R_{PTN}} - 1}$$

Figure B.1: Bifurcation chart for the $K_{\pi 2}$ background study.

$K_{\pi 2}$ Background Study		
Quantity	1/3 Sample	2/3 Sample
N_{RP}	10±3.2	13±3.6
R_E	131.1±49.4	137.1±37.9
N_{Norm}	0.077±0.038	0.096±0.035
R_{PTN}	9.85±0.18	9.59±0.12
$N_{K_{\pi 2}}$	0.009±0.004	0.011±0.004

Table B.1: Numbers for the $K_{\pi 2}$ background estimations from the 1/3 sample and the 2/3 sample.

B.2 Overlapping Photon Background Study

Fig. B.2 shows the bifurcation chart for the overlapping-photon background study. The setup cuts are the Reconstruction Cuts (PASS1CUT), Beam Cuts (PSCUT), Transient Digitizer Cuts (TDCUT), photon cuts (PTNCUT), and Kinematic Cuts (KINCUT) except for the Range Stack dE/dx cut (RSDEDX) and the box cuts on the charged-track kinematics (BOXCUT). The bifurcation is performed between the RSDEDX cuts and the BOXCUT cuts. The overlapping-photon background study is summarized in Table B.2 from both the 1/3 sample and the 2/3 sample, and each quantity is described as follows.

N_{Norm} : Number of events in the normalization branch.
N_{RSDEDX} : Rejection factor of the Range Stack dE/dx cuts (RSDEDX).
$N_{Overlap}$: Estimated overlapping-photon background level.

Overlapping Photon Background Study		
Quantity	1/3 Sample	2/3 Sample
N_{Norm}	0	1
R_{RSDEDX}	35.2	24.5
$N_{Overlap}$	0.067 (90% C.L.)	0.043±0.043

Table B.2: Numbers for the overlapping-photon background estimations from the 1/3 sample and the 2/3 sample.

Overlapping Photon Background Study

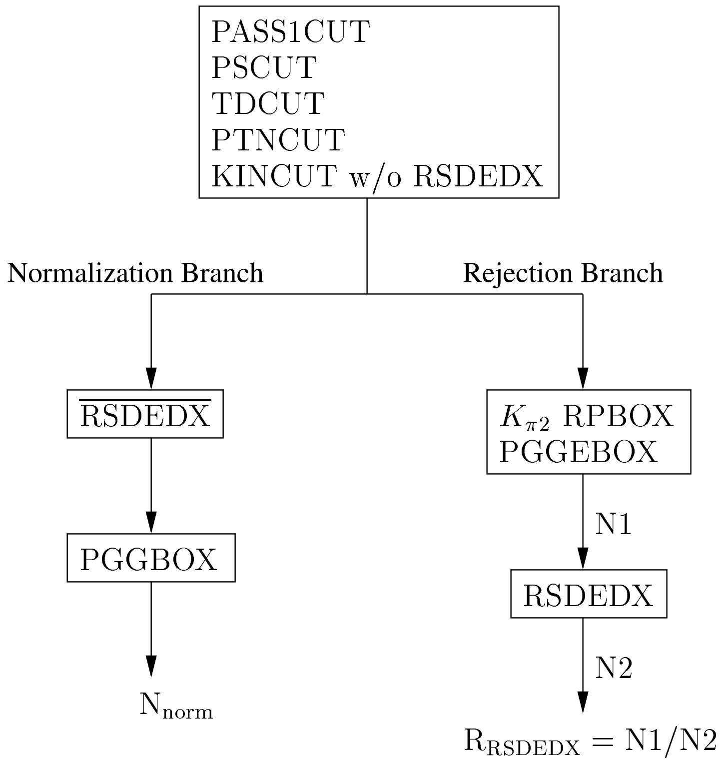

$$\mathrm{N}_{\mathrm{Overlap}} = \frac{\mathrm{N}_{\mathrm{norm}}}{\mathrm{R}_{\mathrm{RSDEDX}} - 1}$$

Figure B.2: Bifurcation chart for the overlapping photon background study.

B.3 Muon Background Study

Fig. B.3 shows the bifurcation chart for the muon background study. The setup cuts are the Reconstruction Cuts (PASS1CUT), Beam Cuts (PSCUT), photon cuts (PTNCUT), and Kinematic Cuts (KINCUT) except for the cut on the range-momentum relation (RNGMOM). The bifurcation is performed between RNGMOM and the Transient Digitizer cuts (TDCUT). The muon background study is summarized in Table B.3 from both the 1/3 sample and the 2/3 sample, and each quantity is described as follows.

N_{Norm}	:	Number of events in the normalization branch.
N_{TD}	:	Rejection factor of the Transient Digitizer cuts (TDCUT).
N_{Muon}	:	Estimated muon background level.

Muon Background Study		
Quantity	1/3 Sample	2/3 Sample
N_{Norm}	21±4.6	44±6.6
R_{TD}	916.4±210.1	737.9±107.6
N_{muon}	0.023±0.007	0.060±0.013

Table B.3: Numbers for the muon background estimations from the 1/3 sample and the 2/3 sample.

MuonBackgroundStudy

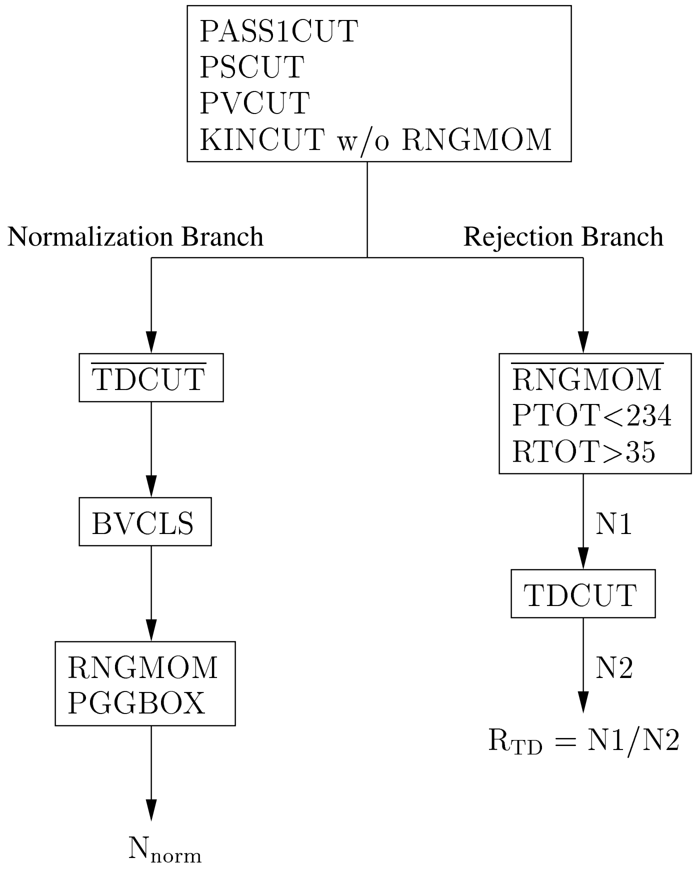

$$\text{N}_{\text{Muon}} = \frac{\text{N}_{\text{norm}}}{\text{R}_{\text{TD}} - 1}$$

Figure B.3: Bifurcation chart for the muon background study.

B.4 Single-Beam Background Study

Fig. B.4 shows the bifurcation chart for the single-beam background study. The setup cuts are the Reconstruction Cuts (PASS1CUT), the cut on the range-momentum relation (RNGMOM), Range Stack dE/dx cut (RSDEDX), BOXCUT, and Beam Cuts (PSCUT) except for the Delayed Coincidence Cuts (DELC) and the Kaon Čerenkov Cut (CKTRS). The bifurcation is performed between the DELC cut and the CKTRS cut. In the normalization branch, further setup cuts are imposed; Target photon veto cut (TGPVCUT), fiducial cuts on the charged track (FIDUCIAL), quality cuts in the drift chamber track fitting (UTCQUAL), Quality Cuts in the Range Stack track fitting (PRRF), kinematic cuts in the Target (TGKIN)[1], and fiducial cuts on the photon cluster (BVCLS). The normalization branch is further bifurcated (2nd bifurcation) in order to estimate the number of events in the normalization branch. In the normalization branch of the 2nd bifurcation, the events that failed the CKTRS cut are tagged, and and number of event after imposing the Transient Digitizer cuts (TDCUT) and photon cuts (PTNCUT) are counted. The rejection factor of CKTRS cut is measured in the rejection branch of the 2nd bifurcation with the events that failed one of the TDCUT cuts and the PTNCUT cuts. The single-beam background study is summarized in Table B.4 from both the 1/3 sample and the 2/3 sample, and each quantity is described as follows.

N_k	:	Number of events in the normalization branch of the 2nd bifurcation.
R_k	:	Rejection factor for the CKTRS cut in the 2nd bifurcation.
N_{Norm}	:	Number of events in the normalization branch obtained from the 2nd bifurcation.
N_{DELC}	:	Rejection factor of the Delayed Coincidence cuts (DELC).
N_{1beam}	:	Estimated single-beam background level.

Single Beam Background Study		
Quantity	1/3 Sample	2/3 Sample
N_k	10±3.2	28±5.3
R_k	10.8±2.4	9.3±1.3
R_{DELC}	>358	205.0±102.2
N_{Norm}	1.0±0.3	3.4±0.8
N_{1beam}	0.003±0.003	0.016±0.009

Table B.4: Numbers for the single-beam background estimations from the 1/3 sample and the 2/3 sample.

[1]TGKIN contains the Target dE/dx cut (TGDEDX), pion gap cut (PIGAP), likelihood cut in the Target reconstruction (TGLIKE) and the cut on the matching between the B4 and Target hit positions (TGB4).

Single Beam Background Study

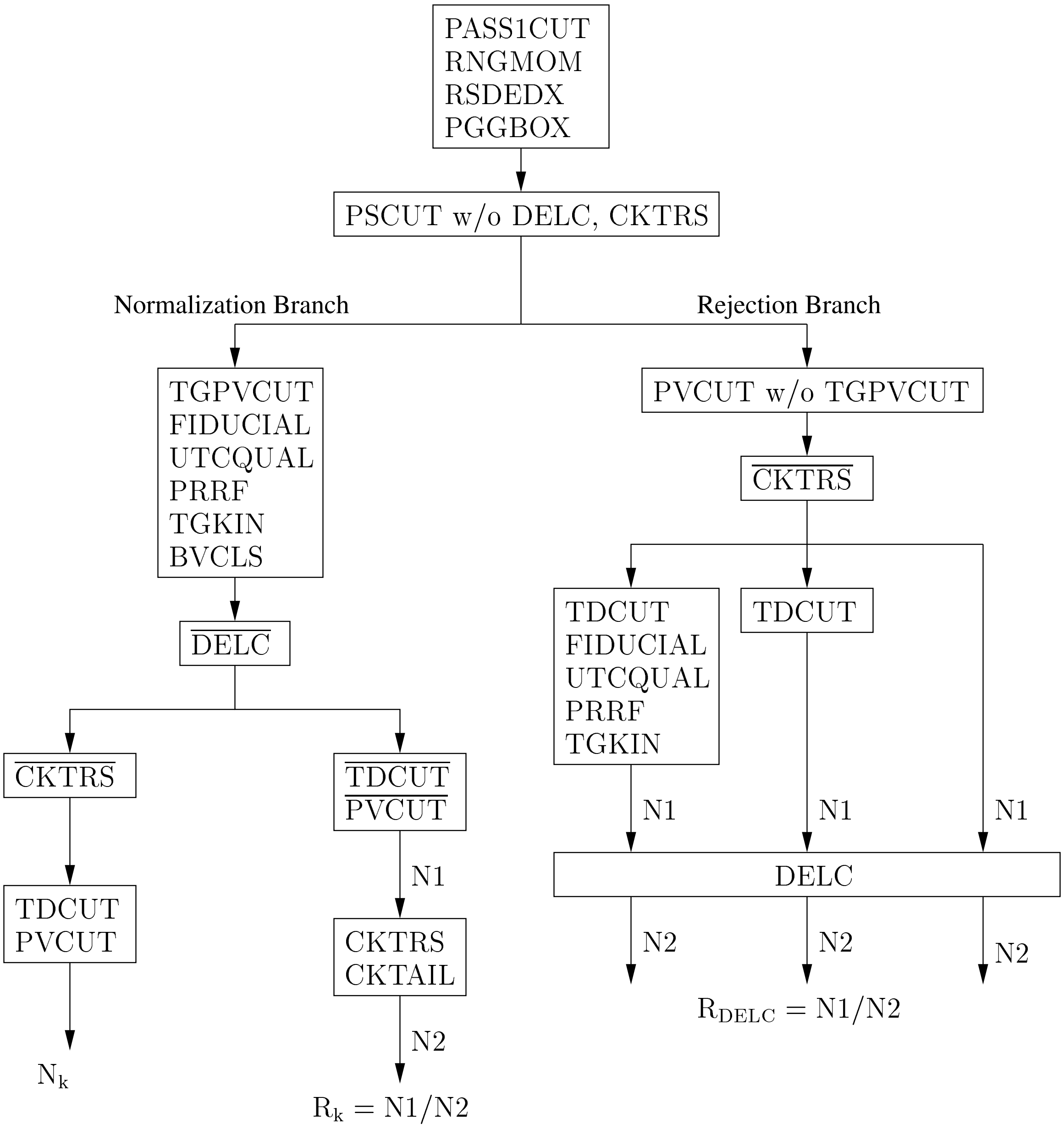

$$N_{norm} = \frac{N_k}{R_k - 1} \qquad N_{1beam} = \frac{N_{norm}}{R_{DELC} - 1}$$

Figure B.4: Bifurcation chart for the single beam background study.

B.5 Double-Beam Background Study

Fig. B.5 shows the bifurcation chart for the double-beam background study. The setup cuts are the Reconstruction Cuts (PASS1CUT), the cut on the range-momentum relation (RNGMOM), Range Stack dE/dx cut (RSDEDX), BOXCUT, and photon cuts (PTN-CUT) except for the Target photon veto cut (TGPVCUT) and the fiducial cuts on the photon cluster (BVCLS). The bifurcation is performed between the Čerenkov counter and Beam Wire Chamber cuts and the B4 counter cuts. In the normalization branch, further setup cuts are imposed; cut on dE/dx in the B4 counter (B4DEDX), the Target quality cut (TGQUALT), timing consistency cut (TIMCON), the delayed coincidence cuts (DELC), the Target energy and range cut (TGER), z position cut in the Target (TGZFOOL), cuts on the upstream photon veto and ring veto counters (UPV/RVTRS), and the consistency cut in the B4 analysis (B4ETCON). The normalization branch is further bifurcated (2nd bifurcation) in order to estimate the number of events in the normalization branch. In the normalization branch of the 2nd bifurcation, the number of event after imposing the B4 counter cuts are counted. The rejection factor of Target Cuts is measured in the rejection branch of the 2nd bifurcation. The double-beam background study is summarized in Table B.4 from both the 1/3 sample and the 2/3 sample, and each quantity is described as follows.

N_{B4}	:	Number of events in the normalization branch of the 2nd bifurcation.
R_{TG}	:	Rejection factor for the CKTRS in the 2nd bifurcation.
N_{Norm}	:	Number of events in the normalization branch obtained from the 2nd bifurcation.
N_{2bm}	:	Rejection factor of the the Čerenkov counter and Beam Wire Chamber cuts.
N_{2beam}	:	Estimated double-beam background level.

Double Beam Background Study		
Quantity	1/3 Sample	2/3 Sample
N_{B4}	0	0
R_{TG}	>21	>37
R_{2bm}	11.8±3.3	11.9±2.3
N_{Norm}	0.13 (90% C.L.)	0.06 (90% C.L.)
N_{2beam}	0.012 (90% C.L.)	0.006 (90% C.L.)

Table B.5: Numbers for the double-beam background estimations from the 1/3 sample and the 2/3 sample.

Double Beam Background Study

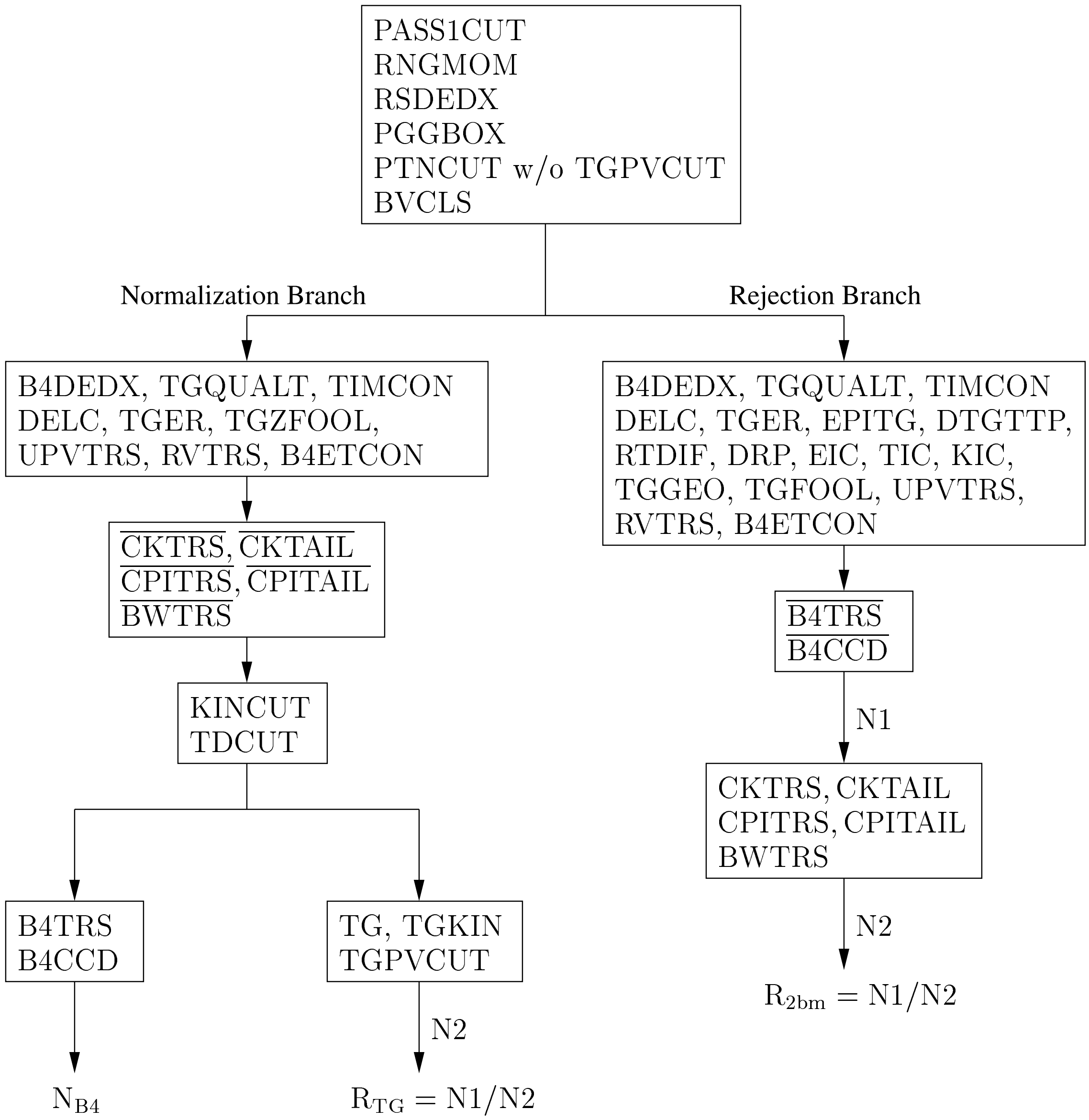

$$N_{norm} = \frac{N_{B4}}{R_{TG} - 1} \qquad N_{2beam} = \frac{N_{norm}}{R_{2bm} - 1}$$

Figure B.5: Bifurcation chart for the double beam background study.

Appendix C

Details of Acceptance Measurements

Details of the acceptance measurements used in the calculations of the single event sensitivity are described.

C.1 Monte Carlo Based Acceptance

The trigger acceptance (A_{trigCT}), the acceptance of the π^+ fiducial cuts (A_{fidCT}) and the π^+ stop efficiency (A_{nidif}) for the $K^+ \to \pi^+\gamma\gamma$ are measured with the Monte Carlo simulation. In addition, the acceptance of the fiducial cuts on the photon clusters (A_{fidBV}), except for the timing cut, and the photon cuts (A_{PV-MC}) are measured. The $K^+ \to \pi^+\gamma\gamma$ events are generate by assuming the ChPT $O(p^6)$ with $\hat{c} = 1.8$, ChPT $O(p^4)$ with $\hat{c} = 1.6$, and the phase space distribution for the π^+ with P_{π^+} >200 MeV/c. Events are generated for both the π^+ nuclear interaction and decay-in-flight (NIDIF) turned on and off. The calculations of the trigger acceptance are summarized in Tables C.1, C.2 and C.3; the acceptance factor is obtained as

$$\begin{aligned} A_{trigCT} &= 0.03455 \pm 0.00008 \quad (\text{for ChPT } O(p^6)) \\ &= 0.00609 \pm 0.00003 \quad (\text{for ChPT } O(p^4)) \\ &= 0.03490 \pm 0.00010 \quad (\text{for Phase Space}). \end{aligned}$$

The "UFATE", "USTMED" and "USTOP_HEX" are prepared in order to estimate the acceptance loss by the $\pi^+ \to \mu^+ \to e^+$ decay chain requirements due to an incorrect assignment of the stopping counter. The UFATE requires that a track does not decay-in-flight nor interact with the Range Stack materials before it comes to rest in the simulation. The USTMED requires that a charged track does not come to rest in the dead materials in the Range Stack in the simulation. The USTOP_HEX requires that the stopping counter in the offline analysis agrees with the true stopping position in the simulation.

The calculations of the acceptance of π^+ fiducial cuts are summarized in Tables C.4, C.5 and C.6; the acceptance factor is obtained as

$$\begin{aligned} A_{fidCT} &= 0.89802 \pm 0.00073 \quad (\text{for ChPT } O(p^6)) \\ &= 0.62606 \pm 0.00279 \quad (\text{for ChPT } O(p^4)) \\ &= 0.89701 \pm 0.00092 \quad (\text{for Phase Space}). \end{aligned}$$

The π^+ stop efficiency is obtained by taking the ratio of the factors with NIDIF turned on and off.

$$\begin{aligned} A_{nidif} &= \frac{A_{trigCT}(\text{NIDIFon})}{A_{trigCT}(\text{NIDIFoff})} \times \frac{A_{fidCT}(\text{NIDIFon})}{A_{fidCT}(\text{NIDIFoff})} \\ &= 0.49226 \pm 0.00215 \quad (\text{for ChPT } O(p^6)) \\ &= 0.57772 \pm 0.00692 \quad (\text{for ChPT } O(p^4)) \\ &= 0.49796 \pm 0.00273 \quad (\text{for Phase Space}). \end{aligned}$$

The calculation of the acceptance of fiducial cuts on the photon cluster are summarized in Tables C.7, C.8 and C.9; the acceptance factor is obtained as

$$\begin{aligned} A_{fidBV} &= 0.55209 \pm 0.00180 \quad (\text{for ChPT } O(p^6)) \\ &= 0.51170 \pm 0.00479 \quad (\text{for ChPT } O(p^4)) \\ &= 0.55768 \pm 0.00226 \quad (\text{for Phase Space}). \end{aligned}$$

The calculation of the acceptance of photon cuts are summarized in Tables C.10, C.11 and C.12; the acceptance factor is obtained as

$$\begin{aligned} A_{PV-MC} &= 0.28075 \pm 0.00220 \quad (\text{for ChPT } O(p^6)) \\ &= 0.22413 \pm 0.00558 \quad (\text{for ChPT } O(p^4)) \\ &= 0.26930 \pm 0.00270 \quad (\text{for Phase Space}). \end{aligned}$$

	NIDIF on		NIDIF off	
Cut	Events	Acceptance	Events	Acceptance
K_B	4999684	–	4999707	–
$T \bullet 2$	2246678	0.44936	2332350	0.46650
$6_{CT} + 7_{CT}$	1873487	0.83389	2298723	0.98558
$16_{CT} + 17_{CT}$	112603	0.06010	184823	0.08040
UFATE	96775	0.85944	184823	1.00000
USTMED	96406	0.99619	184504	0.99827
USTOP_HEX	88512	0.91812	172730	0.93619
A_{trigCT}	0.01770 ± 0.00006		0.03455 ± 0.00008	

Table C.1: Trigger acceptance for the $K^+ \to \pi^+\gamma\gamma$ (ChPT $O(p^6)$ with $\hat{c} = 1.8$).

	NIDIF on		NIDIF off	
Cut	Events	Acceptance	Events	Acceptance
K_B	4999673	–	4999719	–
$T \bullet 2$	2242190	0.44847	2336778	0.46738
$6_{CT} + 7_{CT}$	1880363	0.83863	2301050	0.98471
$16_{CT} + 17_{CT}$	32794	0.01744	37075	0.01611
UFATE	22236	0.67805	37075	1.00000
USTMED	21867	0.98341	36839	0.99364
USTOP_HEX	17081	0.78113	30460	0.82684
A_{trigCT}	0.00342 ± 0.0000261		0.00609 ± 0.00003	

Table C.2: Trigger acceptance for the $K^+ \to \pi^+\gamma\gamma$ (ChPT $O(p^4)$ with $\hat{c} = 1.6$).

	NIDIF on		NIDIF off	
Cut	Events	Acceptance	Events	Acceptance
K_B	3124797	–	3124818	–
$T \bullet 2$	1403625	0.44919	1456344	0.46606
$6_{CT} + 7_{CT}$	1173809	0.83626	1437534	0.98708
$16_{CT} + 17_{CT}$	72813	0.02330	117799	0.08195
UFATE	62817	0.86272	117799	1.00000
USTMED	62555	0.99583	117558	0.99795
USTOP_HEX	56667	0.90588	109048	0.92761
A_{trigCT}	0.01813 ± 0.00008		0.03490 ± 0.00010	

Table C.3: Trigger acceptance for the $K^+ \to \pi^+\gamma\gamma$ (Phase Space).

	NIDIF on		NIDIF off	
Cut	Events	Acceptance	Events	Acceptance
SETUP	87994	–	171761	–
LAY1617	86046	0.97786	169441	0.98649
COS3D	85739	0.99643	169110	0.99805
ZFRF	85739	1.00000	169110	1.00000
ZUTOUT	85717	0.99974	169080	0.99982
PGGBOX	75910	0.88559	154244	0.91226
A_{fidCT}	0.86267 ± 0.00116		0.89802 ± 0.00073	

Table C.4: π^+ fiducial acceptance for the $K^+ \to \pi^+\gamma\gamma$ (ChPT $O(p^6)$ with $\hat{c} = 1.8$).

	NIDIF on		NIDIF off	
Cut	Events	Acceptance	Events	Acceptance
SETUP	16898	–	30176	–
LAY1617	15481	0.91614	28315	0.93833
COS3D	15456	0.99839	28307	0.99972
ZFRF	15456	1.00000	28307	1.00000
ZUTOUT	15452	0.99974	28306	0.99997
PGGBOX	10899	0.70535	18892	0.66742
A_{fidCT}	0.64499 ± 0.00368		0.62606 ± 0.00279	

Table C.5: π^+ fiducial acceptance for the $K^+ \to \pi^+\gamma\gamma$ (ChPT $O(p^4)$ with $\hat{c} = 1.6$).

	NIDIF on		NIDIF off	
Cut	Events	Acceptance	Events	Acceptance
SETUP	56349	–	108462	0.99463
LAY1617	55111	0.97803	106930	0.98588
COS3D	54933	0.99677	106728	0.99811
ZFRF	54933	1.00000	106728	1.00000
ZUTOUT	54913	0.99964	106712	0.99985
PGGBOX	48435	0.88203	97291	0.91172
A_{fidCT}	0.85955 ± 0.00146		0.89701 ± 0.00092	

Table C.6: π^+ fiducial acceptance for the $K^+ \to \pi^+\gamma\gamma$ (Phase Space)

Cut	Events	Acceptance
SETUP	75910	–
NREG	58008	0.76417
EG1	53044	0.91443
COSOPXY	51965	0.97966
COSOPZ	51616	0.99328
DIPANG	51592	0.99953
EG2	41909	0.81231
A_{fidBV}	0.55209 ± 0.00180	

Table C.7: γ fiducial acceptance for the $K^+ \rightarrow \pi^+\gamma\gamma$ (ChPT $O(p^6)$ with $\hat{c} = 1.8$).

Cut	Events	Acceptance
SETUP	10899	–
NREG	8009	0.73484
EG1	7282	0.90923
COSOPXY	6961	0.95592
COSOPZ	6848	0.98377
DIPANG	6845	0.99956
EG2	5577	0.81476
A_{fidBV}	0.51170 ± 0.00479	

Table C.8: γ fiducial acceptance for the $K^+ \rightarrow \pi^+\gamma\gamma$ (ChPT $O(p^4)$ with $\hat{c} = 1.6$).

Cut	Events	Acceptance
SETUP	48435	0.88203
NREG	37453	0.77326
EG1	34459	0.92006
COSOPXY	33730	0.97884
COSOPZ	33548	0.99460
DIPANG	33536	0.99964
EG2	27011	0.80543
A_{fidBV}	0.55768 ± 0.00226	

Table C.9: γ fiducial acceptance for the $K^+ \rightarrow \pi^+\gamma\gamma$ (Phase Space).

Cut	Events	Acceptance
SETUP	41909	–
HEX	19334	0.46133
RSPVCUT	16761	0.86692
BV·BVL	14132	0.84483
COSGG	13886	0.98259
TZMAX	13865	0.99849
EC	13053	0.94144
PVCUT	12107	0.92753
TGPVCUT	11766	0.97183
A_{PV-MC}	0.28075 ± 0.00220	

Table C.10: Photon-cut acceptance for the $K^+ \to \pi^+\gamma\gamma$ (ChPT $O(p^6)$ with $\hat{c} = 1.8$).

Cut	Events	Acceptance
SETUP	5577	–
HEX	2976	0.53362
RSPVCUT	2552	0.85753
BV·BVL	2008	0.78683
COSGG	1814	0.90339
TZMAX	1803	0.99394
EC	1508	0.83638
PVCUT	1343	0.89058
TGPVCUT	1250	0.93075
A_{PV-MC}	0.22413 ± 0.00558	

Table C.11: Photon-cut acceptance for the $K^+ \to \pi^+\gamma\gamma$ (ChPT $O(p^4)$ with $\hat{c} = 1.6$).

Cut	Events	Acceptance
SETUP	27011	–
HEX	13520	0.50054
RSPVCUT	11569	0.85570
BV·BVL	9297	0.80361
COSGG	9088	0.97752
TZMAX	9073	0.99835
EC	8417	0.92770
PVCUT	7697	0.91446
TGPVCUT	7274	0.94504
A_{PV-MC}	0.26930 ± 0.00270	

Table C.12: Photon-cut acceptance for the $K^+ \to \pi^+\gamma\gamma$ (Phase Space).

C.2 $K_{\mu 2}$-Based Acceptance

A number of acceptance factors are measured with the $K_{\mu 2}$ monitor data. The acceptance factors of the basic reconstruction cuts (A_{RD} and A_{recon}) are measured at first because these cuts are used as the setup cuts in the other acceptance measurements. The measurements of A_{RD} and A_{recon} are summarized in Tables C.13 and Table C.14, respectively; the acceptance factors are

$$A_{RD} = 0.99995 \pm 0.00001$$
$$A_{recon} = 0.99561 \pm 0.00012.$$

The acceptance factor of the beam and Target analysis (A_{rest}) is measured by selecting the events within the $\pm 2\sigma$ of the $K_{\mu 2}$ momentum peak. The measurement of A_{rest} is summarized in Table C.15; the acceptance factor is obtained as

$$A_{rest} = 0.50697 \pm 0.00077.$$

The accidental loss due to the online and offline photon veto cuts ($A_{PV-K_{\mu 2}}$) is measured after requiring the offline stopping layer to be 18 or less to avoid muons that reach the Barrel photon detectors. The measurement of $A_{PV-K_{\mu 2}}$ is summarized in Table C.16; the acceptance factor is obtained as

$$A_{PV-K_{\mu 2}} = 0.50697 \pm 0.00077.$$

In addition, the accidental loss due to the online requirement of $18_{ct}+19_{ct}$ ($A_{\bar{\mu}}$) is measured with the $K_{\mu 2}$ monitor data. $A_{\bar{\mu}}$ is obtained as

$$A_{\bar{\mu}} = 0.99625 \pm 0.00065.$$

Cut	Events	Acceptance
SETUP	381644	–
RDTRK	381644	1.00000
TRKTIM	381625	0.99995
A_{RD}	0.99995 ± 0.00001	

Table C.13: $K_{\mu 2}$-based acceptance factor A_{RD}.

Cut	Events	Acceptance
SETUP	291543	–
UTC/RANGE	291543	1.00000
ITGQUAL	290264	0.99561
A_{recon}	0.99561 ± 0.00012	

Table C.14: $K_{\mu 2}$-based acceptance factor A_{recon}.

Cut	Events	Acceptance
SETUP	422384	0.00000
TIC	421583	0.99810
TIMCON	420153	0.99661
DCBIT	368523	0.87712
DELC2	354726	0.96256
TGTCON	352068	0.99251
DELCO	318250	0.90394
CKTRS	313104	0.98383
CKTAIL	305714	0.97640
B4DEDX	300786	0.98388
CPITRS	299408	0.99542
CPITAIL	299202	0.99931
TARGF	286837	0.95867
DTGTTP	286779	0.99980
RTDIF	283525	0.98865
PIGAP	281302	0.99216
TGB4	265541	0.94397
KIC	261507	0.98481
TGGEO	258124	0.98706
EIC	248578	0.99171
B4EKZ	240027	0.99487
TGZFOOL	240027	1.00000
BWTRS	231548	0.96467
RVUPV	227839	0.98398
B4TRS	216661	0.95094
B4CCD	214135	0.98834
A_{rest}	0.50697 ± 0.00077	

Table C.15: $K_{\mu 2}$-based acceptance factor A_{rest}.

Cut	Events	Acceptance
SETUP	25831	–
Online PV	23615	0.98106
STLAY	23340	0.98835
RSHEX	22522	0.96495
PVCUT	21410	0.95063
NREG	19979	0.93316
$A_{PV}^{K_{\mu 2}}$	0.77345 ± 0.00260	

Table C.16: $K_{\mu 2}$-based acceptance factor $A_{PV}^{K_{\mu 2}}$.

C.3 $K_{\pi 2}$-Based Acceptance

The acceptance factor of the OPSVETO cut and the acceptance factors related to the track energy in the Target are measured with the $K_{\pi 2}$ monitor data (A_{opt} and A_{tgkin}). In order to select the $K_{\pi 2}$ events, the reconstruction cuts (PASS1CUT), beam and kinematic cuts except for those whose acceptances are being measured here, Transient Digitizer cuts (TDCUT), and $\pm 2\sigma$ cuts on the $K_{\pi 2}$ momentum, range and kinetic energy around the peaks are imposed as the setup cuts. In addition, the photon clustering in the Barrel photon detectors is performed and the π^0 in the $K_{\pi 2}$ events is tagged in order to confirm that the two photons reach the Barrel region, because the acceptance measurements might be screwed up due to the photon shower in the Target. The measurement of A_{opt} is summarized in Table C.17; the acceptance factor is obtained as

$$A_{opt} = 0.98317 \pm 0.00100.$$

The measurement of A_{tgkin} is summarized in Table C.18; the acceptance factor is obtained as

$$A_{tgkin} = 0.89142 \pm 0.00246.$$

In addition, the acceptance factor of the timing cut on the photon clusters is measured with the $K_{\pi 2}$ monitor data (A_{BVTIME}). The acceptance for a single photon is measured to be 0.98023 ± 0.00140. In the analysis, however, events with two photon-clusters are accepted; the number is squared, conservatively, for the A_{BVTIME} and obtained as

$$A_{BVTIME} = 0.96085 \pm 0.00194.$$

C.4 π_{scat}-Based Acceptance

The acceptance factors of the Kinematic cuts (A_{kin}) and the Transient Digitizer Cuts (A_{TD}) are measured with the π_{scat} monitor data. To measure A_{kin}, the reconstruction cuts, small energy deposit in the B4 counter, a prompt timing in the Target, Range Stack photon-veto cut and the Transient Digitizer cuts are imposed in the setup cuts. The measurement of A_{kin} is summarized in Table C.19; the acceptance factor is obtained as

$$A_{kin} = 0.61280 \pm 0.00675.$$

To measure A_{TD}, the same setup cuts used in the A_{kin} acceptance measurements, with $\pi^+\gamma\gamma$ box cuts, the cut on the range-momentum relation, z-position cuts in the Range Stack and Drift Chamber and the cut on the I-counter energy are imposed, but the Transient Digitizer cuts are unused. The measurement of A_{TD} is summarized in Table C.20 ; the acceptance factor is obtained as

$$A_{TD} = 0.34872 \pm 0.00548.$$

C.5 Categorization of the Acceptances

The acceptance factors obtained in the previous sections are categorized and summarized in Tables C.21, C.22 and C.23.

Cut	Events	Acceptance
SETUP	16397	–
OPSVETO	16121	0.98317
A_{ops}	0.98317 ± 0.00100	

Table C.17: $K_{\pi 2}$-based acceptance factor A_{ops}.

Cut	Events	Acceptance
SETUP	15997	–
TGDEDX	15424	0.96418
TGER	15418	0.99961
TGLIKE	15107	0.97983
EPITG	15100	0.99954
EPIMAXK	14918	0.98795
TGEDGE	14850	0.99544
PHIVTX	14381	0.96842
PHIVTX2	14290	0.99367
DRP	14260	0.99790
A_{tgkin}	0.89142 ± 0.00246	

Table C.18: $K_{\pi 2}$-based acceptance factor A_{tgkin}.

Cut	Events	Acceptance
SETUP	5204	1.00000
UTCQUAL	4856	0.93313
RNGMOM	4807	0.98991
RSDEDX	4097	0.85230
PRRF	3189	0.88781
A_{kin}	0.61280 ± 0.00675	

Table C.19: π_{scat}-based acceptance factor A_{kin}.

Cut	Events	Acceptance
SETUP	7562	–
FITPI	6195	0.81999
RSHEX2	6065	0.97902
Online PID	4081	0.67288
EV5	3425	0.83926
ELVETO	3180	0.92847
TDFOOL	3179	0.99969
TDVAR	2637	0.82951
A_{TD}	0.34872 ± 0.00548	

Table C.20: π_{scat} based acceptance factor A_{TD}.

Definition	Symbol	Acceptances	Method
Trigger	A_{trigCT}	0.03455 ± 0.00008	Monte Carlo
$A^{\pi^+\gamma\gamma}_{\text{Trigger}} = 0.03455 \pm 0.00008$			
π^+ Reconstruction Efficiency	A_{RD} A_{Recon}	0.99995 ± 0.00001 0.99561 ± 0.00012	$K_{\mu 2}$ $K_{\mu 2}$
$A^{\pi^+\gamma\gamma}_{\text{Reconstruction}} = 0.99556 \pm 0.00012$			
π^+ Fiducial Cuts	A_{fidCT}	0.89802 ± 0.00073	Monte Carlo
$A^{\pi^+\gamma\gamma}_{\text{Fiducial}} = 0.89802 \pm 0.00073$			
π^+ Stop Efficiency	A_{nidif}	0.49226 ± 0.00215	Monte Carlo
$A^{\pi^+\gamma\gamma}_{\pi^+\text{StopEff.}} = 0.49226 \pm 0.00215$			
$\pi^+ \to \mu^+ \to e^+$ Decay Chain	A_{TD}	0.34872 ± 0.00548	π_{scat}
$A^{\pi^+\gamma\gamma}_{\pi^+\to\mu^+\to e^+} = 0.34872 \pm 0.00548$			
γ Reconstruction and Fiducial	A_{fidBV} A_{BVTIME}	0.55209 ± 0.00180 0.96085 ± 0.00194	Monte Carlo $K_{\pi 2}$
$A^{\pi^+\gamma\gamma}_{\gamma\text{Recon.\&.Fid.}} = 0.53047 \pm 0.00204$			
Extra Photon Veto Cuts	A_{PV-MC} $A_{PV-K_{\mu 2}}$ $A_{\bar{\mu}}$	0.28075 ± 0.00220 0.77345 ± 0.00260 0.99625 ± 0.00065	Monte Carlo $K_{\mu 2}$ $K_{\mu 2}$
$A^{\pi^+\gamma\gamma}_{\text{ExtraPV}} = 0.21633 \pm 0.00185$			
Kinematic Cuts	A_{ops} A_{tgkin} A_{kin}	0.98317 ± 0.00100 0.89142 ± 0.00246 0.61280 ± 0.00675	$K_{\pi 2}$ $K_{\pi 2}$ π_{scat}
$A^{\pi^+\gamma\gamma}_{\text{Kinematics}} = 0.53706 \pm 0.00613$			
Beam and Target	A_{rest}	0.50697 ± 0.00077	$K_{\mu 2}$
$A^{\pi^+\gamma\gamma}_{\text{Beam\&Target}} = 0.50697 \pm 0.00077$			
$T \bullet 2$ Efficiency($\pi^+\gamma\gamma$)	$A_{T\bullet 2}(\pi^+\gamma\gamma)$	0.9357 ± 0.0011	K_B
$A^{\pi^+\gamma\gamma}_{T\bullet 2\text{Eff.}} = 0.93570 \pm 0.00110$			
$A^{\pi^+\gamma\gamma}(\text{ChPT } O(p^6)) = 1.5502 \pm 0.0344 \times 10^{-4}$			

Table C.21: Categorization of acceptance factors for the $K^+ \to \pi^+\gamma\gamma$ (ChPT $O(p^6)$).

Definition	Symbol	Acceptances	Method
Trigger	A_{trigCT}	0.00609 ± 0.00003	Monte Carlo
$A^{\pi^+\gamma\gamma}_{\text{Trigger}} = 0.00609 \pm 0.00003$			
π^+ Reconstruction Efficiency	A_{RD} A_{Recon}	0.99995 ± 0.00001 0.99561 ± 0.00012	$K_{\mu 2}$ $K_{\mu 2}$
$A^{\pi^+\gamma\gamma}_{\text{Reconstruction}} = 0.99556 \pm 0.00012$			
π^+ Fiducial Cuts	A_{fidCT}	0.62606 ± 0.00279	Monte Carlo
$A^{\pi^+\gamma\gamma}_{\text{Fiducial}} = 0.62606 \pm 0.00279$			
π^+ Stop Efficiency	A_{nidif}	0.57772 ± 0.00692	Monte Carlo
$A^{\pi^+\gamma\gamma}_{\pi^+\text{StopEff.}} = 0.57772 \pm 0.00692$			
$\pi^+ \to \mu^+ \to e^+$ Decay Chain	A_{TD}	0.34872 ± 0.00548	π_{scat}
$A^{\pi^+\gamma\gamma}_{\pi^+\to\mu^+\to e^+} = 0.34872 \pm 0.00548$			
γ Reconstruction and Fiducial	A_{fidBV} A_{BVTIME}	0.51170 ± 0.00479 0.96085 ± 0.00194	Monte Carlo $K_{\pi 2}$
$A^{\pi^+\gamma\gamma}_{\gamma\text{Recon.\&.Fid.}} = 0.49166 \pm 0.00471$			
Extra Photon Veto Cuts	A_{PV-MC} $A_{PV-K_{\mu 2}}$ $A_{\bar{\mu}}$	0.22413 ± 0.00558 0.77345 ± 0.00260 0.99625 ± 0.00065	Monte Carlo $K_{\mu 2}$ $K_{\mu 2}$
$A^{\pi^+\gamma\gamma}_{\text{ExtraPV}} = 0.17271 \pm 0.00434$			
Kinematic Cuts	A_{ops} A_{tgkin} A_{kin}	0.98317 ± 0.00100 0.89142 ± 0.00246 0.61280 ± 0.00675	$K_{\pi 2}$ $K_{\pi 2}$ π_{scat}
$A^{\pi^+\gamma\gamma}_{\text{Kinematics}} = 0.53706 \pm 0.00613$			
Beam and Target	A_{rest}	0.50697 ± 0.00077	$K_{\mu 2}$
$A^{\pi^+\gamma\gamma}_{\text{Beam\&Target}} = 0.50697 \pm 0.00077$			
$T \bullet 2$ Efficiency($\pi^+\gamma\gamma$)	$A_{T\bullet 2}(\pi^+\gamma\gamma)$	0.9357 ± 0.0011	K_B
$A^{\pi^+\gamma\gamma}_{T\bullet 2\text{Eff.}} = 0.93570 \pm 0.00110$			
$A^{\pi^+\gamma\gamma}(\text{ChPT } O(p^4)) = 1.6550 \pm 0.00597 \times 10^{-5}$			

Table C.22: Categorization of the acceptance factors for the $K^+ \to \pi^+\gamma\gamma$ (ChPT $O(p^4)$).

Definition	Symbol	Acceptances	Method
Trigger	A_{trigCT}	0.03490 ± 0.00010	Monte Carlo
$A^{\pi^+\gamma\gamma}_{\text{Trigger}} = 0.03490 \pm 0.00010$			
π^+ Reconstruction Efficiency	A_{RD} A_{Recon}	0.99995 ± 0.00001 0.99561 ± 0.00012	$K_{\mu 2}$ $K_{\mu 2}$
$A^{\pi^+\gamma\gamma}_{\text{Reconstruction}} = 0.99556 \pm 0.00012$			
π^+ Fiducial Cuts	A_{fidCT}	0.89701 ± 0.00092	Monte Carlo
$A^{\pi^+\gamma\gamma}_{\text{Fiducial}} = 0.89701 \pm 0.00092$			
π^+ Stop Efficiency	A_{nidif}	0.49796 ± 0.00273	Monte Carlo
$A^{\pi^+\gamma\gamma}_{\pi^+\text{StopEff.}} = 0.49796 \pm 0.00273$			
$\pi^+ \to \mu^+ \to e^+$ Decay Chain	A_{TD}	0.34872 ± 0.00548	π_{scat}
$A^{\pi^+\gamma\gamma}_{\pi^+\to\mu^+\to e^+} = 0.34872 \pm 0.00548$			
γ Reconstruction and Fiducial	A_{fidBV} A_{BVTIME}	0.55768 ± 0.00226 0.96085 ± 0.00194	Monte Carlo $K_{\pi 2}$
$A^{\pi^+\gamma\gamma}_{\gamma\text{Recon.\&.Fid.}} = 0.53584 \pm 0.00242$			
Extra Photon Veto Cuts	A_{PV-MC} $A_{PV-K_{\mu 2}}$ $A_{\bar{\mu}}$	0.26930 ± 0.00270 0.77345 ± 0.00260 0.99625 ± 0.00065	Monte Carlo $K_{\mu 2}$ $K_{\mu 2}$
$A^{\pi^+\gamma\gamma}_{\text{ExtraPV}} = 0.20751 \pm 0.00220$			
Kinematic Cuts	A_{ops} A_{tgkin} A_{kin}	0.98317 ± 0.00100 0.89142 ± 0.00246 0.61280 ± 0.00675	$K_{\pi 2}$ $K_{\pi 2}$ π_{scat}
$A^{\pi^+\gamma\gamma}_{\text{Kinematics}} = 0.53706 \pm 0.00613$			
Beam and Target	A_{rest}	0.50697 ± 0.00077	$K_{\mu 2}$
$A^{\pi^+\gamma\gamma}_{\text{Beam\&Target}} = 0.50697 \pm 0.00077$			
$T \bullet 2$ Efficiency$(\pi^+\gamma\gamma)$	$A_{T\bullet 2}(\pi^+\gamma\gamma)$	0.9357 ± 0.0011	K_B
$A^{\pi^+\gamma\gamma}_{T\bullet 2\text{Eff.}} = 0.93570 \pm 0.00110$			
$A^{\pi^+\gamma\gamma}(\text{Phase Space}) = 1.5330 \pm 0.00361 \times 10^{-4}$			

Table C.23: Categorization of the acceptance factors for the $K^+ \to \pi^+\gamma\gamma$ (Phase Space).

Appendix D

Acceptance Factors for the K^+ Stop Efficiency Calculation

In order to measure the K^+ stop efficiency, the $K_{\pi2}$ events in the $K^+ \to \pi^+\gamma\gamma$ triggers are selected by imposing the fiducial cuts on the charged track, reconstruction cuts, beam cuts, Transient Digitizer cuts, online photon-veto cuts, and fiducial cuts on the photon cluster. These cuts are listed in Table D.1 together with the reduction of the number of events. The number of events after imposing all the cuts ($N_{K_{\pi2}}$) is obtained as

$$N_{K_{\pi2}} = 212709.$$

The acceptance factors of trigger (A_{trigCT}) and fiducial cuts on the charged track (A_{fidCT}) are measured with the Monte Carlo simulation. The $K_{\pi2}$ events with the $K^+ \to \pi^+\gamma\gamma$ trigger conditions are generated for this purpose. The measurements of A_{trigCT} and A_{fidCT} are summarized in Table D.2 and Table D.3, respectively; these acceptance factors are obtained as

$$A_{trigCT} = (0.48090 \pm 0.00310) \times 10^{-4}$$

$$A_{fidCT} = 0.13127 \pm 0.00229.$$

The acceptance factors of the reconstruction cuts (A_{recon}), beam cuts (A_{rest}), online photon veto cuts and the fiducial cuts on the photon cluster (A_{PV}), are measured with the $K_{\pi2}$ monitor data. The measurements of A_{recon}, A_{rest} and A_{PV} are summarized in Tables D.4, D.5 and D.6, respectively, and these acceptance factors are obtained to as

$$A_{recon} = 0.79409 \pm 0.00078$$

$$A_{rest} = 0.46627 \pm 0.00102$$

$$A_{PV} = 0.14418 \pm 0.00105.$$

The acceptance factor for the Transient Digitizer cuts (A_{TD}) is measured with the π_{scat} monitor data. The measurement of A_{TD} is summarized in Table D.6; the acceptance factor is obtained as

$$A_{TD} = 0.35269 \pm 0.00842.$$

Cut	Events
SAMPLE	10706477
RDTRK	10706477
TRKTIM	10704170
UTC/RANGE	10080195
UTCQUAL	6623652
ITGQUAL	3782591
COS3D	3746863
B4DEDX	3632615
CPITRS	3584714
CPITAIL	3581782
ICBIT	3581782
TIC	3564391
TIMCON	3502629
TGTCON	3448519
DCBIT	3448519
DELCO	2738745
CKTRS	2570489
CKTAIL	2508233
BWTRS	2376164
RVUPV	2325795
TARGF	2217390
DTGTTP	2217235
RTDIF	2184689
PIGAP	2165883
TGB4	2067925
KIC	2043717
TGGEO	1797481
B4EKZ	1739250
TGZFOOL	1739250
FITPI	1089144
$K_{\pi 2}$ BOX	429803
LAY1617	423711
BVCLS	333015
TDCUT	212709
$N_{K\pi 2}$	212709

Table D.1: List of the selection cuts imposed in the K^+ stop efficiency calculation with the reduction of the number of events.

Cut	Events	Acceptance
K_B	49996887	–
$T \bullet 2$	22438481	0.448798
$6_{CT} + 7_{CT}$	18816958	0.838602
$16_{CT} + 17_{CT}$	156868	0.008337
UFATE	65778	0.419321
USTMED	61659	0.937380
USTOP_HEX	24042	0.389919
A_{trigCT}	$0.48090 \pm 0.00310 \times 10^{-4}$	

Table D.2: Trigger acceptance for the $K_{\pi 2}$ events with the $K^+ \to \pi^+ \gamma\gamma$ trigger conditions

Cut	Events	Acceptance
SETUP	21742	–
ITGQUAL	14077	0.655560
LAY1617	3435	0.244015
COS3D	3432	0.999127
$K_{\pi 2}$ BOX	2854	0.831585
A_{fidCT}	0.13127 ± 0.00229	

Table D.3: Acceptance factor A_{fidCT} of the fiducial cuts imposed in the K^+ stop efficiency calculation.

Cut	Events	Acceptance
SETUP	270327	–
UTC/RANGE	270327	1.00000
UTCQUAL	227113	0.84014
ITGQUAL	214663	0.94518
A_{recon}	0.79409 ± 0.00078	

Table D.4: Acceptance factor A_{recon} of the reconstruction cuts imposed in the K^+ stop efficiency calculation.

Cut	Events	Acceptance
SETUP	239751	–
TIC	239615	0.99943
TIMCON	238784	0.99653
DCBIT	210472	0.88143
DELCO2	202545	0.96234
TGTCON	200576	0.99028
DELCO	183624	0.91548
CKTRS	178794	0.97370
CKTAIL	174030	0.97335
B4DEDX	171220	0.98385
CPITRS	169405	0.98940
CPITAIL	169262	0.99916
TARGF	162122	0.95782
DTGTTP	162120	0.99999
RTDIF	160532	0.99020
PIGAP	159043	0.99072
TGB4	150369	0.94546
KIC	148157	0.98529
TGGEO	122530	0.82703
EIC	122530	1.00000
B4EKZ	118986	0.99499
TGZFOOL	118986	1.00000
BWTRS	113779	0.95624
RVUPV	111789	0.98251
B4TRS	111789	1.00000
B4CCD	111789	1.00000
A_{rest}	0.46627 ± 0.00102	

Table D.5: Acceptance factor A_{rest} of the beam and Target cuts imposed in the K^+ stop efficiency calculation.

Cut	Events	Acceptance
SETUP	111789	–
Online PV	20713	0.18529
BVCLS	16118	0.77816
A_{PV}	0.14418 ± 0.00105	

Table D.6: Acceptance factor A_{PV} of the photon cuts imposed in the K^+ stop efficiency calculation.

Cut	Events	Acceptance
SETUP	3221	1.00000
FITPI	2686	0.83468
RSHEX2	2634	0.98064
Online PID	1715	0.65110
EV5	1465	0.85423
ELVETO	1359	0.92765
TDFOOL	1359	1.00000
TDVAR	1136	0.83591
A_{TD}	0.35269 ± 0.00842	

Table D.7: Acceptance factor A_{TD} of the Transient Digitizer cuts imposed in the K^+ stop efficiency calculation.

Appendix E

Acceptance Factors for the $K_{\mu 2}$ Branching Ratio

In order to measure the $K_{\mu 2}$ branching ratio, the $K_{\mu 2}$ events in the $K_{\mu 2}$ trigger events are selected by imposing the fiducial cuts on the charged track, reconstruction cuts, beam cuts, and photon veto cuts. These cuts are listed in Table E.1 together with the reduction of the number of events. The number of events after imposing all the cuts ($N_{K_{\mu 2}}$) is obtained as

$$N_{K_{\mu 2}} = 252908.$$

The acceptance factors of trigger (A_{trigCT}) and the fiducial cuts on the charged track (A_{fidCT}) are measured with the Monte Carlo simulation. The $K_{\mu 2}$ events with the $K_{\mu 2}$ trigger conditions are generated for this purpose. The measurements of A_{fidCT} and A_{trigCT} are summarized in Tables E.2 and E.3, respectively; the acceptance factors are obtained as

$$\begin{aligned} A_{trigCT} &= 0.44244 \pm 0.00050 \\ A_{fidCT} &= 0.98394 \pm 0.00020. \end{aligned}$$

The acceptance factors of the reconstruction cuts (A_{RD} and A_{recon}), beam cuts (A_{rest}), and photon veto cuts (A_{PV}) are measured with the $K_{\mu 2}$ monitor data. The measurements of A_{RD}, A_{recon}, A_{rest} and A_{PV} are summarized in Table E.4, E.5, E.6 and E.7, respectively; these acceptance factors are obtained as

$$\begin{aligned} A_{RD} &= 0.99995 \pm 0.00001 \\ A_{recon} &= 0.84682 \pm 0.00062 \\ A_{rest} &= 0.55984 \pm 0.00076 \\ A_{PV} &= 0.95556 \pm 0.00127. \end{aligned}$$

Cut	Events
SETIP	761777
BADRUN	761736
BADSTC	761725
RDTRK	761725
TRKTIM	761450
UTC/RANGE	728648
UTCQUAL	576936
ITGQUAL	569465
COS3D	561951
B4DEDX	550280
CPITRS	543235
CPITAIL	542718
ICBIT	542442
TIC	539677
TIMCON	536997
TGTCON	532309
DCBIT	454980
DELCO	393640
CKTRS	380853
CKTAIL	369556
BWTRS	348924
RVUPV	342897
TARGF	326759
DTGTTP	326697
RTDIF	322916
PIGAP	319609
TGB4	301121
KIC	296431
TGGEO	288863
B4EKZ	278022
TGZFOOL	278022
PVCUT	254233
RTOT40	252908
$N_{K_{\mu 2}}$	252908

Table E.1: List of the selection cuts imposed in the $K_{\mu 2}$ branching-ratio calculation with the reduction of the number of events.

Cut	Events	Acceptance
K_B	999997	–
$T \bullet 2$	454982	0.45498
$17_{CT} + 18_{CT} + 19_{CT}$	442441	0.97244
A_{trigCT}	0.44244±0.00050	

Table E.2: Trigger acceptance for $K_{\mu 2}$.

Cut	Events	Acceptance
SETUP	408455	–
COS3D	402899	0.98640
KM2BOX	401895	0.99751
A_{fidCT}	0.98394±0.00020	

Table E.3: Acceptance factor A_{fidCT} of the fiducial cuts imposed in the $K_{\mu 2}$ branching-ratio calculation.

Cut	Events	Acceptance
SETUP	381644	–
RDTRK	381644	1.00000
TRKTIM	381625	0.99995
A_{RD}	0.99995 ± 0.00001	

Table E.4: Acceptance factor A_{RD} of the reconstruction cuts imposed in the $K_{\mu 2}$ branching-ratio calculation.

Cut	Events	Acceptance
SETUP	342768	–
UTC/RANGE	342768	1.00000
UTCQUAL	291543	0.85055
TARGET	290264	0.99561
A_{recon}	0.84682 ± 0.00062	

Table E.5: Acceptance factor A_{recon} of the reconstruction cuts imposed in the $K_{\mu 2}$ branching-ratio calculation.

Cut	Events	Acceptance
SETUP	422384	–
TIC	421583	0.99810
TIMCON	420153	0.99661
DCBIT	368523	0.87712
DELCO2	354726	0.96256
TGTCON	352068	0.99251
DELCO	318250	0.90394
CKTRS	313104	0.98383
CKTAIL	305714	0.97640
B4DEDX	300786	0.98388
CPITRS	299408	0.99542
CPITAIL	299202	0.99931
TARGF	286837	0.95867
DTGTTP	286779	0.99980
RTDIF	283525	0.98865
TGQUALT	283525	1.00000
PIGAP	281302	0.99216
TGB4	265541	0.94397
KIC	261507	0.98481
TGGEO	258124	0.98706
EIC	258124	1.00000
B4EKZ	249213	0.99491
TGZFOOL	249213	1.00000
BWTRS	240308	0.96427
RVUPV	236466	0.98401
B4TRS	236466	1.00000
B4CCD	236466	1.00000
A_{rest}	0.55984 ± 0.00076	

Table E.6: Acceptance factor A_{rest} of the beam cuts imposed in the $K_{\mu2}$ branching-ratio calculation.

Cut	Events	Acceptance
SETUP	26530	–
PVCUT	25351	0.95556
A_{PV}	0.95556 ± 0.00127	

Table E.7: Acceptance factor A_{PV} of photon veto cuts imposed in the $K_{\mu2}$ branching-ratio calculation.

Appendix F

Acceptance Factors for the $K^+ \to \pi^+\gamma$ Branching Ratio

In the calculation of the single-event sensitivity for $K^+ \to \pi^+\gamma$, the acceptance factors of the trigger (A_{trigCT}), fiducial cuts on the charged track (A_{fidCT}), π^+ stop efficiency (A_{nidif}), fiducial cuts on the photon cluster (A_{fidBV}), and the photon cuts (A_{PV-MC}) are measured with the Monte Carlo simulation. The $K^+ \to \pi^+\gamma$ events with the $K^+ \to \pi^+\gamma\gamma$ trigger conditions are generated for this purpose. The measurements of A_{trigCT}, A_{fidCT}, A_{fidBV} and A_{PV-MC} are summarized in the Tables F.1, F.2, F.3 and F.4, respectively; these acceptance factors are obtained as

$$\begin{aligned} A_{trigCT} &= 0.12491 \pm 0.00021 \\ A_{fidCT} &= 0.94162 \pm 0.00042 \\ A_{nidif} &= 0.45982 \pm 0.00145 \\ A_{fidBV} &= 0.70376 \pm 0.00124 \\ A_{PV-MC} &= 0.43507 \pm 0.00161. \end{aligned}$$

The acceptances are categorized as in the Table F.5, the total acceptance is obtained as

$$A^{\pi^+\gamma} = (1.0844 \pm 0.0022) \times 10^{-3}.$$

	NIDIF on		NIDIF off	
Cut	Events	Acceptance	Events	Acceptance
K_B	2499839	–	2499866	–
$T \bullet 2$	1122758	0.44913	1156989	0.46282
$6_{CT} + 7_{CT}$	940684	0.83783	1151236	0.99593
$16_{CT} + 17_{CT}$	178585	0.18984	334525	0.29058
UFATE	164216	0.91954	334525	1.00000
USTMED	163697	0.99684	333987	0.99839
USTOP_HEX	150678	0.92047	312263	0.93496
A_{trigCT}	0.06028 ± 0.00015		0.12491 ± 0.00021	

Table F.1: Trigger acceptance for the $K^+ \to \pi^+\gamma$.

	NIDIF on		NIDIF off	
Cut	Events	Acceptance	Events	Acceptance
SETUP	150142	–	311447	–
LAY1617	148957	0.99211	310430	0.996735
COS3D	147959	0.99330	308692	0.994401
ZFRF	147958	0.99999	308692	1.000000
ZUTOUT	147926	0.99978	308594	0.999683
PGGBOX	134723	0.91075	293264	0.950323
A_{fidCT}	0.89730 ± 0.00078		0.94162 ± 0.00042	

Table F.2: Acceptance factor A_{fidCT} of the fiducial cuts for the $K^+ \to \pi^+\gamma$.

Cut	Events	Acceptance
SETUP	134723	–
NREG	123237	0.91474
EG1	117053	0.94982
COSOPXY	114711	0.97999
COSOPZ	114556	0.99865
DIPANG	114543	0.99989
EG2	94812	0.82774
A_{fidBV}	0.70376 ± 0.00124	

Table F.3: Acceptance factor A_{fidBV} of the fiducial cuts on the photon cluster for the $K^+ \to \pi^+\gamma$.

Cut	Events	Acceptance
SETUP	94812	–
HEX	64294	0.67812
RSPVCUT	61225	0.95227
BV·BVL	42173	0.68882
COSGG	42164	0.99979
TZMAX	42164	1.00000
EC	42146	0.99957
PVCUT	42041	0.99751
TGPVCUT	41250	0.98119
A_{PV-MC}	0.43507 ± 0.00161	

Table F.4: Acceptance factor A_{PV-MC} of the photon cuts for the $K^+ \to \pi^+\gamma$.

Definition	Symbol	Acceptances	Method
Trigger	A_{trigCT}	0.12491 ± 0.00021	Monte Carlo
$A^{\pi^+\gamma\gamma}_{\text{Trigger}} = 0.12491 \pm 0.00021$			
π^+ Reconstruction Efficiency	A_{RD} A_{Recon}	0.99995 ± 0.00001 0.99561 ± 0.00012	$K_{\mu 2}$ $K_{\mu 2}$
$A^{\pi^+\gamma\gamma}_{\text{Reconstruction}} = 0.99556 \pm 0.00012$			
π^+ Fiducial Cuts	A_{fidCT}	0.94162 ± 0.00042	Monte Carlo
$A^{\pi^+\gamma\gamma}_{\text{Fiducial}} = 0.94162 \pm 0.00042$			
π^+ Stop Efficiency	A_{nidif}	0.45982 ± 0.00145	Monte Carlo
$A^{\pi^+\gamma\gamma}_{\pi^+\text{StopEff.}} = 0.45982 \pm 0.00145$			
$\pi^+ \to \mu^+ \to e^+$ Decay Chain	A_{TD}	0.34872 ± 0.00548	π_{scat}
$A^{\pi^+\gamma\gamma}_{\pi^+\to\mu^+\to e^+} = 0.34872 \pm 0.00548$			
γ Reconstruction and Fiducial	A_{fidBV} A_{BVTIME}	0.70376 ± 0.00124 0.96085 ± 0.00194	Monte Carlo $K_{\pi 2}$
$A^{\pi^+\gamma\gamma}_{\gamma\text{Recon.\&.Fid.}} = 0.676201 \pm 0.00181$			
Extra Photon Veto Cuts	A_{PV-MC} $A_{PV-K_{\mu 2}}$ $A_{\bar{\mu}}$	0.43507 ± 0.00161 0.77345 ± 0.00260 0.99625 ± 0.00065	Monte Carlo $K_{\mu 2}$ $K_{\mu 2}$
$A^{\pi^+\gamma\gamma}_{\text{ExtraPV}} = 0.33525 \pm 0.00169$			
Kinematic Cuts	A_{ops} A_{tgkin} A_{kin}	0.98317 ± 0.00100 0.89142 ± 0.00246 0.61280 ± 0.00675	$K_{\pi 2}$ $K_{\pi 2}$ π_{scat}
$A^{\pi^+\gamma\gamma}_{\text{Kinematics}} = 0.53706 \pm 0.00613$			
Beam and Target	A_{rest}	0.50697 ± 0.00077	$K_{\mu 2}$
$A^{\pi^+\gamma\gamma}_{\text{Beam\&Target}} = 0.50697 \pm 0.00077$			
$T \bullet 2$ Efficiency$(\pi^+\gamma\gamma)$	$A_{T\bullet 2}(\pi^+\gamma\gamma)$	0.9357 ± 0.0011	K_B
$A^{\pi^+\gamma\gamma}_{T\bullet 2\text{Eff.}} = 0.93570 \pm 0.00110$			
$A^{\pi^+\gamma} = 1.0844 \pm 0.0022 \times 10^{-3}$			

Table F.5: Categorization of the acceptance factors for the $K^+ \to \pi^+\gamma$.

Appendix G

Upgrade of the Level-0 Trigger System

As mentioned in the section 2.1, various improvements were made to E787 in order for E949 to reach a sensitivity of 10^{-10}. A new programmable trigger board and digital mean-timer modules using complex programmable logic device (CPLD) have been introduced to the E949 trigger system [34]. Details of the upgrade are described in this appendix.

G.1 Overview of the E949 Trigger System

The E949 trigger system consists of fast Level-0 (L0) trigger, Level 1.1 (L1.1) and Level 1.2 (L1.2) triggers. They are based entirely on ECL signals. A block diagram of the E949 L0 trigger system is shown in Fig. G.1. The L0 trigger system is composed of several FASTBUS modules. Two trigger boards (the "RZ board" and "Trigger Transmitter" in Fig. G.1) latch a variety of signals from the detector onto the 65 bit wide Trigger Bus (T-Bus), which is then read by the L0 trigger board. The L0 trigger board makes a decision using the T-Bus bits. The L1.1 and L1.2 triggers involve processing of TD and ADC data with a longer decision time but at the lower rate of events that pass the L0 trigger.

All trigger decisions, defined as combinational logic on L0 trigger bits, are performed by the L0 trigger board. Note that all L0 trigger bits on T-Bus are latched by $T \bullet 2$ and every $T \bullet 2$ introduces a dead time of 40 ns. As will be described below, every L0 decision signal introduces a dead time of 100 ns. With a L0 pass and a subsequent $L1.1 \cdot L1.2$ pass the start signal for readout of the data is issued.

The E949 experiment aims to accumulate more statistics with higher beam intensity than E787. The trigger system must work more flexibly and with less dead time. In E949, a programmable L0 trigger board was installed to increase the flexibility of the trigger. Digital Mean-timer modules were installed to reduce the acceptance loss of the online photon veto.

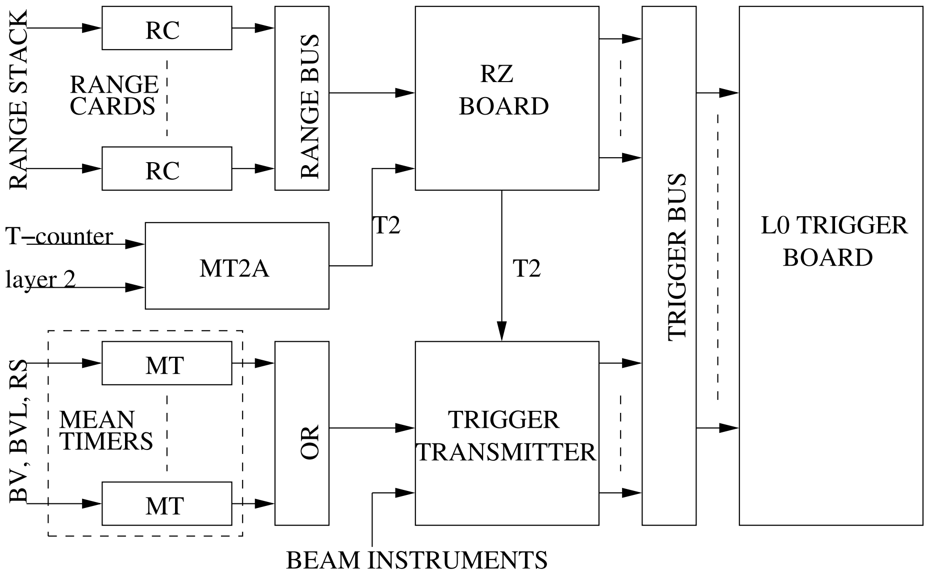

Figure G.1: A block diagram of the E949 L0 trigger system. All trigger decisions, defined as combinational logic of L0 trigger bits on the Trigger Bus, are performed by the L0 trigger board. Note that the dashed line region at the bottom-left corner of the figure are newly installed Mean-timers described later.

G.2 Level-0 Trigger Board

The L0 trigger board for E787 used wire-wrap ECL logic in a FASTBUS board; one had to re-wire the board to modify the trigger condition. In E949, trigger modifications were expected because of the detector upgrade, and we therefore developed a new programmable L0 trigger board. The board has Complex Programmable Logic Device (CPLD) chips (a product of the ALTERA corporation). Any trigger logic can be programmed using the Hardware Description Language (HDL). The CPLD has In System Program (ISP) capability. The trigger conditions can be modified through a JTAG link without extracting the board from the crate. The specifications of the new L0 trigger board are summarized in Table G.1; a picture of the board is shown in Fig. G.2. For the trigger logic, two high-speed PLD chips (EPM7032-B-4) are used. In addition to the high-speed PLD, the board has a large-scale PLD chip (EPF10K100E-1) for various additional applications, such as trigger prescaling and on-board diagnostics, which will be described below.

The $T \bullet 2$ signal initiates the trigger process and creates a dead time of 40 ns. If a L0 condition is satisfied, the dead time must be extended for further trigger processing. This scheme is illustrated in Fig. G.3. The OR-ed L0 decision signal is fed to the RZ board, which extends the $T \bullet 2$ signal via a one-shot to 100 ns. In order to realize this scheme, the propagation time of the new board is required to be less than 19 ns. We chose the SY100ELT24 (25) for the TTL/ECL (ECL/TTL) converter chips. The high-speed CPLD and ECL/TTL converter chips meet the requirement (see Table G.2).

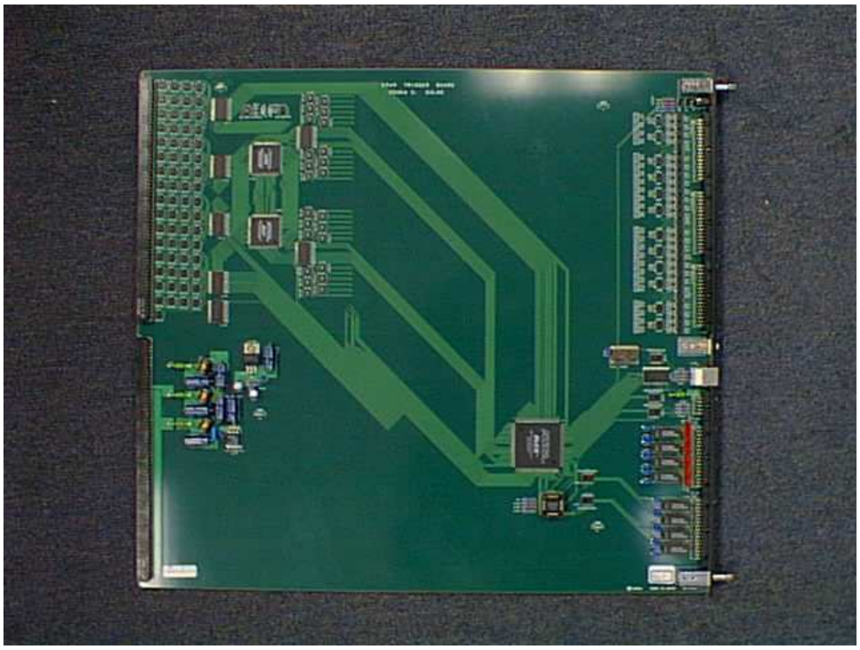

Figure G.2: A picture of the new L0 trigger board. Two high-speed PLD chips for trigger logic are located at the top-left corner. A large-scale PLD for various applications is located at the bottom-right corner.

High-speed PLD	EPM7032B-4
Large-scale PLD	EPF10K100E-1
Board Size	FASTBUS
Input	65 ECL at back 16 ECL at front
Output	24 ECL (duplicated) 3 Or-ed (output) 16 ECL at front

Table G.1: Specifications of the L0 trigger board

ECL/TTL + TTL/ECL conversion	2 ns
EPM7032B-4	12 ns
propagation on board	2 ns
TOTAL	16 ns

Table G.2: Propagation time of the L0 trigger board.

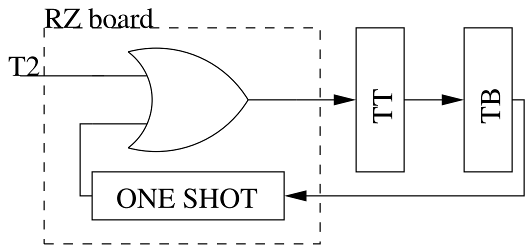

Figure G.3: A schematic view of extending the L0 dead time. Any L0 trigger decisions extend the $T \bullet 2$ width from 40 ns to 100 ns.

G.2.1 Prescaler

The number of L0 decisions for monitor triggers should be prescaled at the L0 trigger board, because any L0 decision signal introduces 100 ns dead time as described in the above scheme. In the E787 experiment, the prescaling was done by a module after the L0 trigger board. In order to reduce the trigger dead time, it is better to prescale before the L0 decision signal of a monitor trigger is issued. We therefore introduced an on-chip prescaler to the L0 trigger board. A block diagram of the prescaler on the trigger board is shown in Fig. G.4. The trigger decision signal of a monitor trigger is fed to the large-scale PLD, which counts the number of events. After reaching the prescale factor, the large-scale PLD issues an enable signal to the high-speed PLD for the next event. The prescaling factor can be selected through ECL lines (at front panel) from a computer. Introducing the prescaler on the trigger for monitoring the charged tracks from kaon decays (defined as $K_B \cdot DC \cdot T \bullet 2$), which required the largest prescale factor and therefore produced a dead time of 4.0%, the L0 dead time was reduced to 1.7%.

G.2.2 Diagnostic System

In the upgrade of the trigger system, debugging time is desired to be as short as possible. We therefore introduced an on-chip diagnostic system in the large-scale PLD. A block diagram of the diagnostic system is shown in Fig. G.5. The large-scale PLD counts the number of events (scaler) and monitors the hit pattern of input signals from the T-Bus (hit pattern finder). The on-chip scaler counts a trigger decision signal from both new and old trigger boards, and compares the number of events. No disagreement was observed at 10^{-6} level during the engineering run of E949. A hit pattern finder allowed for easy debugging when new triggers were introduced. The information is read through ECL lines (at front panel) from a computer.

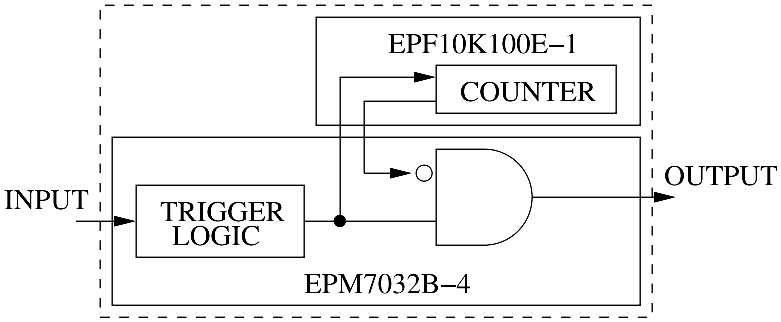

Figure G.4: A schematic view of the on-chip prescaler. After reaching the number of the prescaling factor, the large-scale PLD issues the enable signal to the high-speed PLD for the next event.

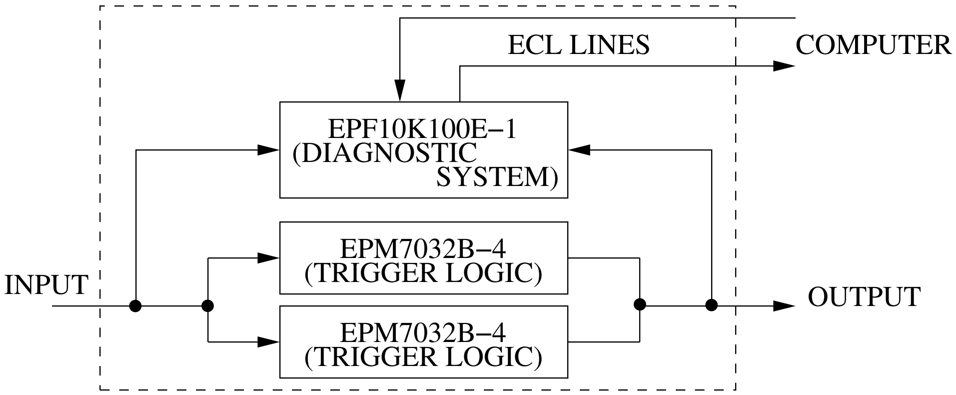

Figure G.5: A block diagram of the diagnostic system. On-chip scaler and hit pattern finder were introduced via a large-scale PLD. The information is read through ECL lines from a computer.

G.3 Mean-timer Module

Digital Mean-timer modules were installed for the online photon veto of the E949 experiment. The time distribution of the online photon veto signal due to a photon hit from a $K_{\pi 2}$ decay is peaked at around t=0. This photon hit can be removed by a veto whose width is determined by the time resolution of the photon veto signal relative to that of the $T \cdot 2$. In the E787 experiment, analog sum signals of the single ends of the RS and BV counters were used for the photon veto signal, and the veto time width was large (typically 20 ns) to account for the timing variations due to the z-position of the photons. By using a Mean-timer module, the veto time width can be narrowed and accidental veto rate therefore reduced. The signals of both ends of the RS, BV and BVL counters are mean-timed in the Mean-timer. The mean-timed signals are fed to the Trigger Transmitter and used as L0 photon veto signals.

Gate arrays have been used as digital Mean-timers previously [35], but we have now developed a digital Mean-timer using the remarkably fast CPLD's available today. Fig. G.6 shows the logic circuit of the digital Mean-timer described in HDL. The triangles in the figure represent a logic element which is the minimum component of the CPLD device (called a "delay-cell"). The propagation time of the delay-cell is 1 ns [36]. The serial line of delay-cells is called a "delay-line", and two delay-lines are used in the digital Mean-timer. The signal of both ends of the scintillator are fed to the delay-line. Fig. G.7 shows the time progress of the signals in the scintillator and the delay-line. The left-right coincidence signals occurs at a fixed time regardless of the time difference between the left and right signals.

Due to space limitations in the electronics hut, the Mean-timer combined the functions of a discriminator and a Mean-timer. Six Mean-timer blocks were implemented in a large scale PLD. A picture and block diagram of this module is shown in Fig. G.8 and Fig. G.9, respectively. The specifications are shown in Table G.3.

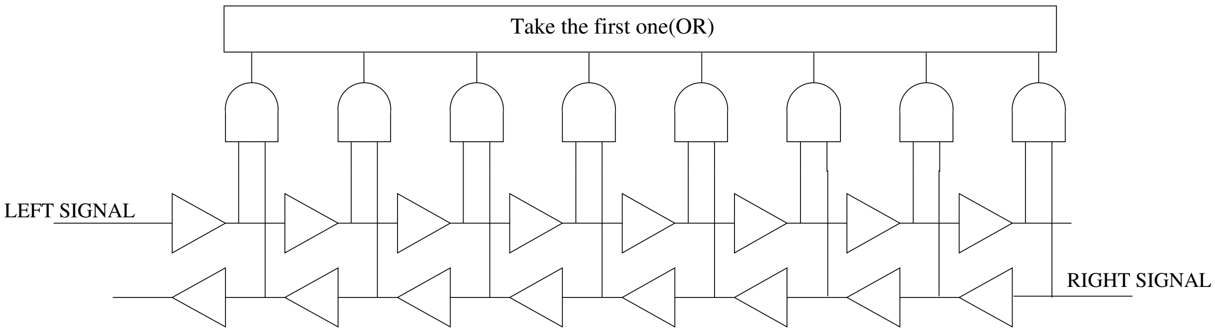

Figure G.6: Logic circuit of the digital Mean-timer described in HDL. The triangles represent a logic element which is the minimum component of the CPLD (called a "delay-cell").

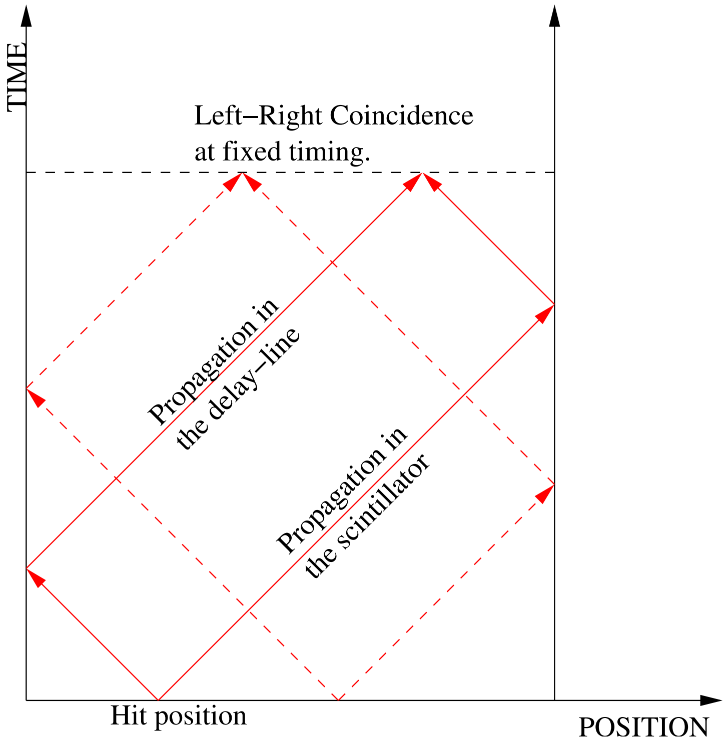

Figure G.7: Time progress of the signals in the scintillator and delay-line. Left-Right coincidence for any hit positions in the scintillator (e.g. solid line and dashed line) occurs at the fixed timing.

PLD	EPF10K50E-1
Board Size	CAMAC
Input	12 analog
Output	16 ECL at front

Table G.3: Specifications of the Mean-timer module.

Figure G.8: A picture of the Mean-timer module. A large-scale PLD is located at Middle-left of the module.

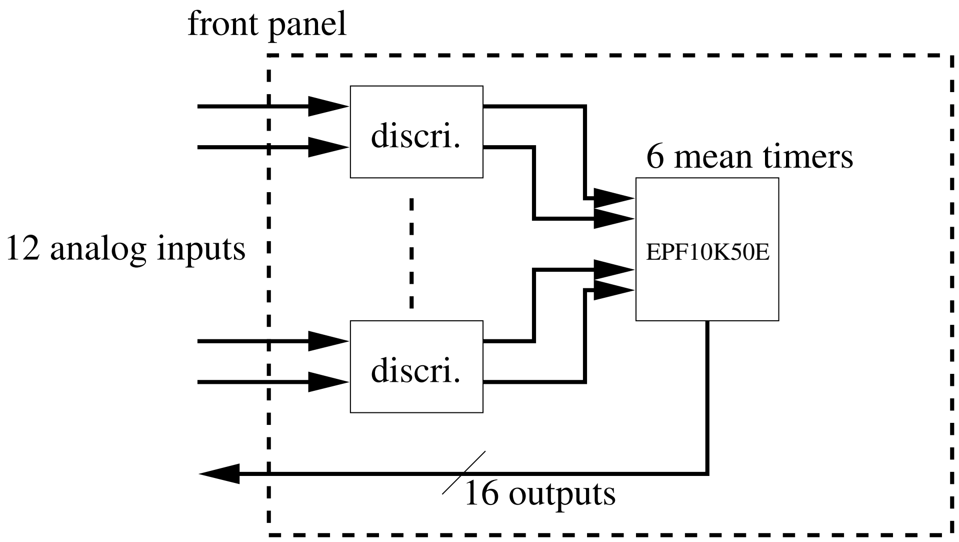

Figure G.9: A block diagram of the Mean-timer module. This module combined the functions of a discriminator and a Mean-timer.

G.3.1 Performance on the test bench

The performance of the Mean-timer was tested on a test bench. Two random signals from gate generators were input to the Mean-timer module. The two input signals and the mean-timed signal were fed into a CAMAC TDC with 25 ps resolution (see Fig. G.10). The left plot of Fig. G.11 shows the time distribution of the two input signals. Since 12 delay-cells in a delay-line are used for this test, the range is 12 ns. The right plot of the Fig. G.11 shows the time distribution of the difference of the online and offline mean-timed signals. The sigma is 0.26 ns.

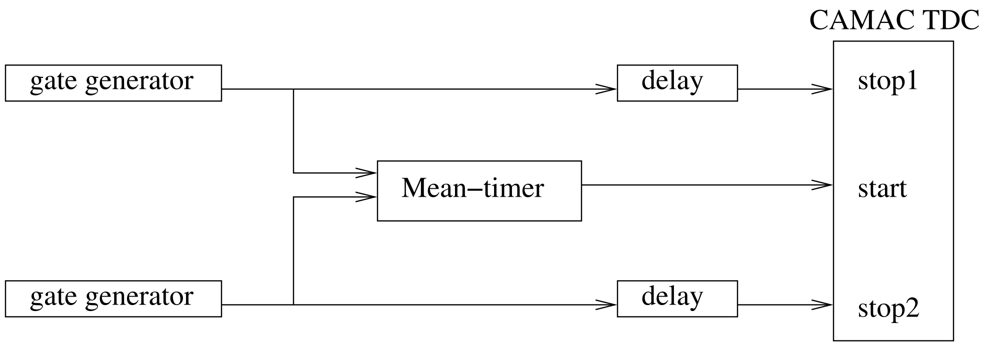

Figure G.10: A block diagram of setup for the Mean-timer performance test.

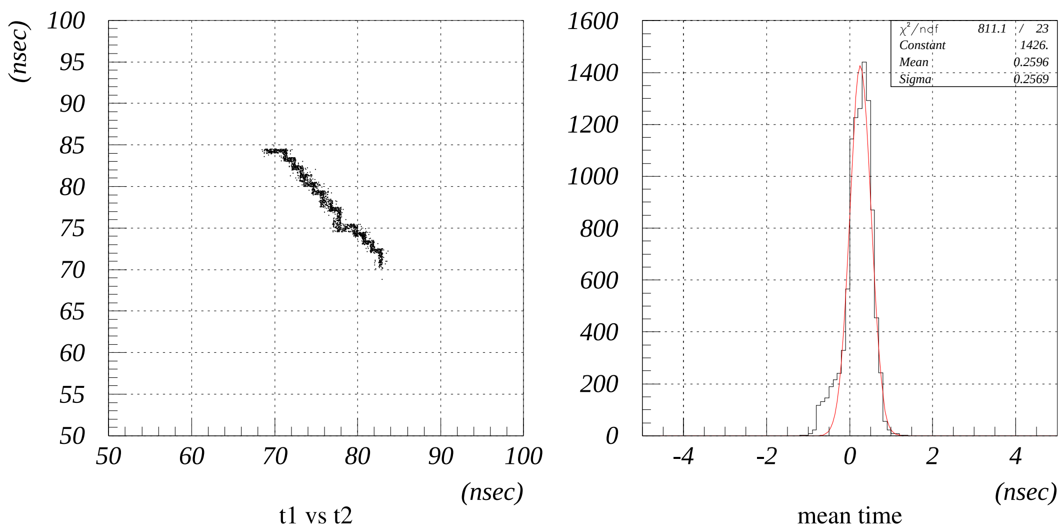

Figure G.11: Scatter plot of the two input signals (left) and difference of the online and offline mean timed signal (right). The sigma in the right plot is 0.26 ns. A dip at around t=78 ns in the left plot is due to the scheme of the CPLD.

G.3.2 Performance with beam

The digital Mean-timers were installed in the E949 trigger system and the performance was checked. Fig. G.12 shows the time distribution of the online photon veto signal. The top-left (right) figure shows the distribution of the BV (BVL) analog sum and bottom-left (right) figure shows the distribution of the BV (BVL) Mean-timer signals relative to the π^+ track time in $K_{\pi 2}$ decays. The hits at around t=0 due to electromagnetic showers in the detector were removed efficiently with half the veto width of the previous system. Fig. G.13 shows the online photon veto acceptance as a function of the kaon beam intensity. The open circles are for the Mean-timer and the black dots are for the analog sum. The acceptance loss was reduced by more than half at each beam intensity. The overall acceptance loss of the online photon veto was reduced from 4.9% to 1.8% by introducing the Mean-timer modules.

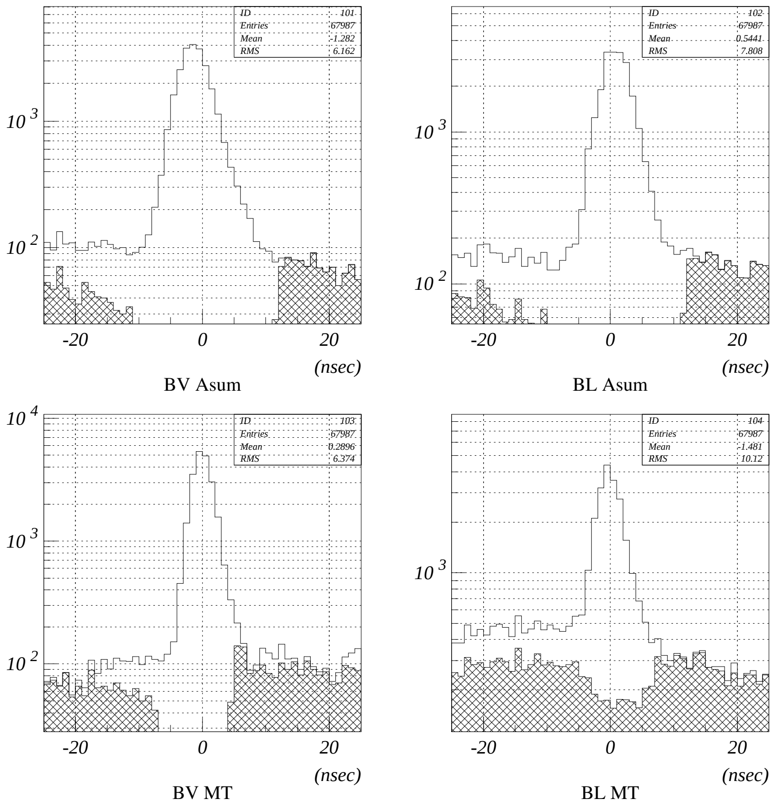

Figure G.12: Performance of the digital Mean-timer. Open histogram shows $K_{\pi 2}$ distribution of hit times in the photon veto systems when the bit is not set. Shaded histogram shows the time distribution for events with the bit set. In all cases the time distributions of the photon veto signals is shown relative to the time of the π^+ track.

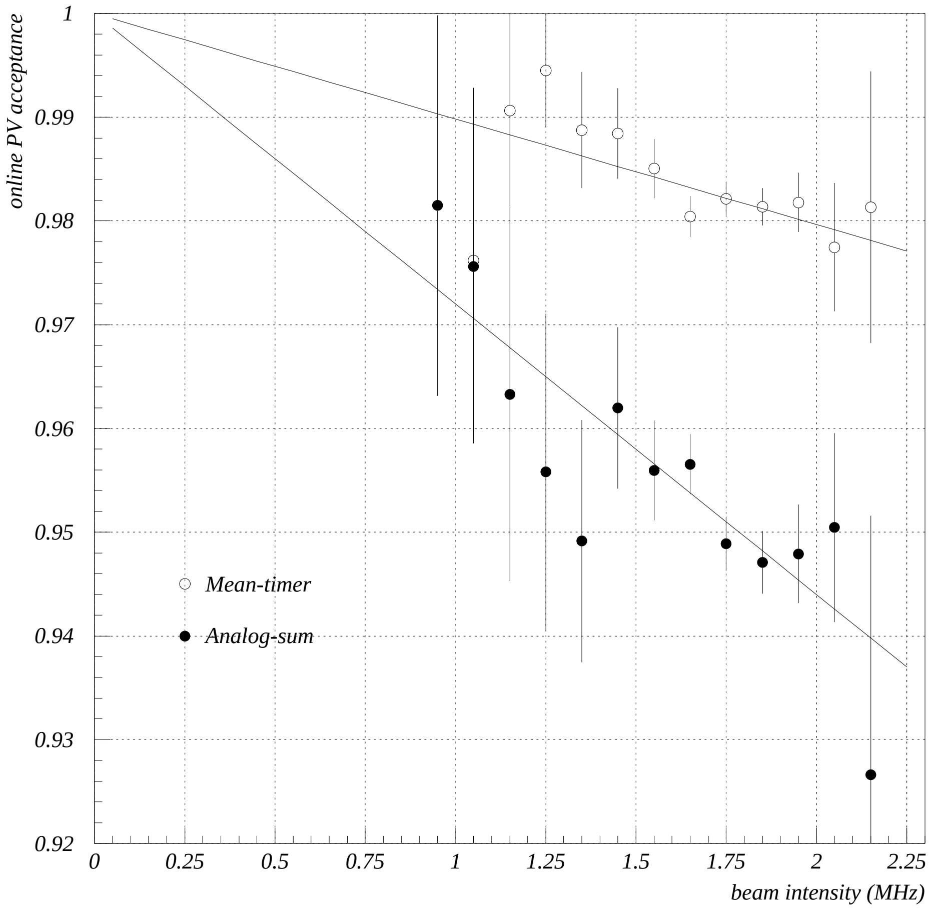

Figure G.13: Comparison of the online photon veto acceptance as a function of the kaon beam intensity between Mean-timer (open circles) and analog sum (black dots). The acceptance loss was reduced by more than half at each beam intensity.

Bibliography

[1] S. Weinberg, PhysicaA **96**, 327 (1979).

[2] J. Gasser and H. Leutwyler, Ann. Phys. (N.Y.) 158, 142 (1984); Nucl. Phys. B **250**, 465 (1985).

[3] J. F. Donoghue, E. Golowhich, and B. R. Holstein, *Dynamics of the Standard Model*, (Cambridge University Press, Cambridge, 1992).

[4] Y. Nambu, Phys. Rev. Lett. **4**, 380 (1960).

[5] J. Goldstone, Nuovo Cim. **19**, 154 (1961).

[6] P. Kitching *et al.* [E787 Collaboration], Phys. Rev. Lett. **79**, 4079 (1997).

[7] G. Ecker, A. Pich and E. de Rafael, Nucl. Phys. B **303**, 665 (1988).

[8] G. Ecker, A. Pich and E. de Rafael, Phys. Lett. B **237**, 481 (1990).

[9] H. Y. Cheng, Phys. Rev. D **42**, 72 (1990).

[10] C. Bruno and J. Prades, Z. Phys. C **57**, 585 (1993).

[11] G. Ecker, J. Kambor and D. Wyler, Nucl. Phys. B **394**, 101 (1993).

[12] G. D. Barr *et al.* [NA31 Collaboration], Phys. Lett. B **284**, 440 (1992).

[13] V. Papadimitriou *et al.*, Phys. Rev. D **44**, 573 (1991).

[14] A. Alavi-Harati *et al.* [KTeV Collaboration], Phys. Rev. Lett. **83**, 917 (1999).

[15] A. Lai *et al.* [NA48 Collaboration], Phys. Lett. B **536**, 229 (2002).

[16] L. Cappiello, G. D'Ambrosio and M. Miragliuolo, Phys. Lett. B **298**, 423 (1993).

[17] A. G. Cohen, G. Ecker and A. Pich, Phys. Lett. B **304**, 347 (1993).

[18] G. D'Ambrosio and J. Portolés, Phys. Lett. B **386**, 403 (1996) [Phys. Lett. B **389**, 770 (1996 ERRAT,B395,390.1997)]; Nucl. Phys. B **492**, 417 (1997).

[19] V. V. Anisimovsky *et al.* [E949 Collaboration], Phys. Rev. Lett. **93**, 031801 (2004).

[20] J. Doornbos *et al.*, Nucl. Instrum. Meth. A **444**, 546 (2000).

[21] D. A. Bryman *et al.*, Nucl. Instrum. Meth. A **396**, 394 (1997).

[22] E. W. Blackmore *et al.*, Nucl. Instrum. Meth. A **404**, 295 (1998).

[23] M. Atiya *et al.*, Nucl. Instrum. Meth. A **279**, 180 (1989).

[24] I. H. Chiang *et al.*, IEEE Trans. Nucl. Sci. **42**, 394 (1995).

[25] T. K. Komatsubara *et al.*, Nucl. Instrum. Meth. A **404**, 315 (1998).

[26] S. C. Adler *et al.* [E787 Collaboration], Phys. Rev. Lett. **79**, 2204 (1997).

[27] T. Junk, Nucl. Instrum. Meth. A **434**, 435 (1999).

[28] W. Nelson, H. Hirayama and D. Rogers, SLAC-0265, (1985)

[29] Mark R. Convery, "First Measurement of Structure Dependent $K^+ \to \mu^+\nu_\mu\gamma$", Princeton University *PhD* thesis, (1996)

[30] S. Eidelman *et al.* [Particle Data Group Collaboration], Phys. Lett. B **592**, 1 (2004).

[31] G. J. Feldman and R. D. Cousins, Phys. Rev. D **57**, 3873 (1998).

[32] J. Trampetic, Acta Phys. Polon. B **33**, 4317 (2002).

[33] S. C. Adler *et al.* [E787 Collaboration], Phys. Rev. D **65**, 052009 (2002).

[34] T. Yoshioka *et al.*, IEEE Trans. Nucl. Sci. **51**, 334 (2004).

[35] J. Chapman and J. Mann, "Triggering in the SDC using mean timer synchronizers with straw drift tubes", Proceedings of the first annual conference on electronics for future colliders, 151 (1991).

[36] ALTERA, "FLEX10KE Embedded Programmable Logic Family Data Sheet", ver.2.10 (2000).